Sooi Li Lee

Graduated in

Bachelor in Chemical Engineering

Role of Surfactants in Filtration and Fouling of Colloidal Silica

Dissertation for obtaining the Master degree in Membrane Engineering

Erasmus Mundus Master in Membrane Engineering

Advisor(s): Kitty Nijmeijer, Professor, MST, University of Twente
Antoine Kemperman, Senior Researcher, MST, University of Twente

Jury:

President: João Crespo, Professor, FCT-UNL
Member(s): Damien Quémener, Associate Professor, Université Montpellier 2
Vlastimil Fila, Associate Professor, Institute of Chemical Technology Prague
Svetlozar Velizarov, Researcher, FCT-UNL

FACULDADE DE CIÊNCIAS E TECNOLOGIA
UNIVERSIDADE NOVA DE LISBOA

July 2014

Sooi Li Lee

Graduated in

Role of Surfactants in Filtration and Fouling of Colloidal Silica

Dissertation presented to Faculdade de Ciências e Tecnologia, Universidade Nova de Lisboa for obtaining the master degree in Membrane Engineering

July 2014

TITLE: Role of Surfactants in Filtration and Fouling of Colloidal Silica

The EM3E Master is an Education Programme supported by the European Commission, the European Membrane Society (EMS), the European Membrane House (EMH), and a large international network of industrial companies, research centres and universities (http://www.em3e.eu).

Projecto financiado com o apoio da Comissão Europeia. A informação contida nesta publicação vincula exclusivamente o autor, não sendo a Comissão responsável pela utilização que dela possa ser feita.

Acknowledgements

"Science does not know its debt to imagination."

Ralph Waldo Emerson

First and foremost, I would like to thank my family, without their support, encouragement and understanding, I will not be where I am nor who I am today. Plus it was always a fantastic reason to visit your daughter/sister… In Europe.

To my supervisors, Dr. Ir. Antoine Kemperman and Prof. Dr.Ir. Kitty Nijmeijer, thank you for the opportunity to undertake my thesis in MST. I am grateful for all your motivation, professionalism and much-appreciated feedback.

Krzysztof, it was a pleasure to work with and for(!) you. Could not have asked for a better daily supervisor, and I deeply appreciate all your help and constructive feedback in the duration of my whole thesis. I hope OSMO will behave itself in the future.

The contributions of Dr. Ir. Wiebe de Vos and Joris de Grooth in the form of discussions and suggestions are also recognised.

The MST crew for making my stay in UT and Enschede a great one. I thank you for your friendship and I think my experience would not be this memorable otherwise. Also, I think I may have consumed enough cakes and treats in the last 5 months for the next year. Also a special thanks to my fellow EM3E 2nd Edition mates for your camaraderie and for being there. Two years have come and gone. Time flies when you are having fun.

I thank EM3E program coordinators, Prof. André Ayral, Prof. Isabel Coelho, Prof. João Crespo and Dr Elena Vallejo for their support and continuous guidance they offered during the masters program.

The financial support received from the European Union in the form of scholarship throughout the masters program is appreciated.

Abstract

The objective of this study is to investigate the influence of three different types of surfactants (i) anionic sodium dodecyl sulphate (SDS), (ii) cationic (hexadecyltrimethylammonium bromide (CTAB), and (iii) non-ionic: Triton X-100 (Polyethylene glycol *tert*-octylphenyl ether) and the effect of surfactant concentration on ultrafiltration of colloidal silica nanoparticles. Due to the high surface area to volume ratio of nanoparticles, the role of surface interactions on the stability of silica suspensions is enhanced. The effects of adsorption of surfactants are studied by means of static light scattering and zeta potential measurements. The strongest particle-surfactant interaction is observed between oppositely charged CTAB with silica, followed by TX-100 and SDS.

An ultrafiltration hollow-fibre membrane is used in a semi-dead end configuration to perform filtration of silica suspension with varying surfactant concentration to critical micelle concentration (CMC) ratio, $c_{surfactant}/c_{cmc}$ in a flux-step mode. The effect of surfactants and process conditions (flux) on filtration process have been compared by evaluating the critical flux and total fouling rate. The occurrence of critical flux and evolution of fouling rates are also strongly affected by the surfactant concentration. This difference in filtration performance is attributed to various competing and complementary mechanisms: electrostatic and hydrophobic interactions between surfactant-membrane surface, electrostatic and hydrophobic interactions between particles as well as the hydrodynamic effect of fluid motion towards the membrane. A comparison of the overall fouling potential for surfactant-silica systems showed that SDS-silica systems showed fouling rates of an order of magnitude higher than those of CTAB-silica and TX100-silica systems at the same c_{surf}/c_{CMC} ratio. This was an unexpected finding, as we would expect stable colloidal systems such as SDS-silica systems would exhibit lower fouling than unstable colloidal systems (e.g. CTAB-silica systems).

Keywords: Ionic and non-ionic surfactants, Adsorption, Ultrafiltration, Flux-step method, Fouling rate

Index of Figures

FIGURE 2-1: SCHEMATIC REPRESENTATION OF THE TYPES OF FUNCTIONAL GROUPS THAT OCCUR ON THE SILICA SURFACE (A) HYDRATED AND (B) ANYHYDROUS SILANOL GROUPS ARE ASSOCIATED WITH THE HYDROXYLATED SURFACE, WHEREAS (C) SILOXANE-DEHYDRATED GROUPS OCCUR MAINLY ON THE PYROGENIC SURFACE [5]. 12

FIGURE 2-2: INTERACTION ENERGY BETWEEN TWO SILICA NANOPARTICLES (HAMAKER CONSTANT: $0.8 \cdot 10^{-20}$ J [13], PARTICLE DIAMETER: 22 NM) CALCULATED ACCORDING TO DLVO THEORY; (A) INFLUENCE OF THE SURFACE CHARGE IN 1 MM NACL SOLUTION; (B) INFLUENCE OF THE NACL CONCENTRATION FOR THE NANOPARTICLE SURFACE CHARGE OF -30 MV; (C) INFLUENCE OF THE CATION VALENCY FOR THE NANOPARTICLE SURFACE CHARGE OF -30 MV. 14

FIGURE 2-3: CARTOONS DISPLAYING DIFFERENT MORPHOLOGIES THAT MAY FORM DURING THE ADSORPTION OF A SOLUBLE SURFACTANT TO A CLEAN HYDROPHILIC SUBSTRATE (1D). AT VERY LOW COVERAGE, THE HYDROCARBON CHAINS OF THE ADSORBED SURFACTANT MAY BE LIE PERPENDICULAR TO THE SURFACE (1A), PARALLEL TO THE SURFACE (1B), OR BE RANDOMLY ORIENTED (1C). AS THE COVERAGE INCREASES, THE MOLECULES MAY BE RANDOMLY DISTRIBUTED IN A SINGLE LAYER (LANGMUIR BEHAVIOR, 2C) OR INTERACTIONS BETWEEN SURFACTANT MOLECULES MAY LEAD TO THE FORMATION OF HEMIMICELLES (2A) OR ADMICELLES (2B). AT HIGH COVERAGES, A RANGE OF STRUCTURES ARE CONCEIVABLE: MONOLAYER (3A), HEMIMICELLES ON A MONOLAYER (3B), BILAYER (3C) OR ADMICELLES (3D) [14] 16

FIGURE 2-4: GENERAL SHAPE OF ADSORPTION ISOTHERM AND PROPOSED MOLECULAR MODEL FOR TWO-STEP AND FOUR-REGION ADSORPTION MODELS [21, 23]. 17

FIGURE 2-5: ADSORPTION ISOTHERM OF CTAB ON SIO_2 AS REPORTED BY TYRODE ET AL [14] 18

FIGURE 2-6: ADSORPTION OF SDS ONTO SILICA AND SILICA PRETREATED WITH POLYETHYLENE OXIDE AT ROOM TEMPERATURE ($23 \pm 2°C$) AND NEUTRAL PH (6.5 TO 7) [31] 19

FIGURE 2-7: ADSORPTION ISOTHERMS OF TX100 ON SYTON W30 AND LUDOX HS40 AT PH 6 [42] 20

FIGURE 2-8: ADSORPTION ISOTHERMS OF TRITON X-100 ON SYTON W30 AT VARIOUS PH [42]. 20

FIGURE 2-9: CTAB STRUCTURE: CATIONIC HEAD AND HYDROPHOBIC TAIL. 21

FIGURE 2-10: SIMPLIFIED SCHEME OF CTAB 'TAIL TO TAIL' BILAYER AND MULTILAYER FORMATION ON SIO_2-WATER INTERFACE [50]. 22

FIGURE 2-11: POSSIBLE SIMPLIFIED SCHEME OF CTAB-SIO_2-WATER INTERFACE AS PROPOSED BY LIU AND CO-WORKERS [44]. COUNTERIONS BR- ARE OMITTED FOR CLARITY. 23

FIGURE 2-12: STRUCTURE OF SDS: ANIONIC HEAD AND HYDROPHOBIC TAIL. 23

FIGURE 2-13: STRUCTURE OF NON-IONIC SURFACTANT TRITON X-100. 24

FIGURE 2-14: SCHEMATIC OF THE FORCES THAT ARE INVOLVED IN A DEAD END FILTRATION PROCESS. 28

FIGURE 3-1: (A) TOP VIEW OF THE PRINCIPLE OF LIGHT SCATTERING SET-UP. L: LIGHT SOURCE; 1: FILTERS, LENSES; 2: SAMPLE CELL; 3: MOBILE DETECTOR. (B) DEFINITION OF SCATTERING VOLUME VS IN A CROSS-SECTION OF THE INCOMING BEAM AND DETECTION BEAM [74]. 32

FIGURE 3-2: AN EXAMPLE OF A FILTRATION MODULE AND A SCHEMATIC DESCRIBING THE MODULE OPERATING IN A SEMI DEAD-END CONFIGURATION. 34

FIGURE 3-3: SCHEMATIC REPRESENTATION OF PERMPOROMETER SETUP [77]. 35

FIGURE 3-4: FLOWSHEET OF THE OSMO FILTRATION SETUP. BW AND FEED ARE BACKWASH WATER AND FEED WATER TANKS RESPECTIVELY. THE FLOWS ARE CONTROLLED BY TWO MASS FLOW CONTROLLERS (F). PRESSURE (P) IS MEASURED IN THE FEED, BACKWASH, PERMEATE AND RETENTATE. TEMPERATURE IS MONITORED IN THE FEED AND DOWNSTREAM OF THE BACKWASH PUMP. 37

FIGURE 3-5: PICTURE OF THE OSMO INSPECTOR FILTRATION SETUP. 37

FIGURE 3-6: LAYOUT OF ONE FILTRATION-BACKWASH CYCLE (ADAPTED FROM VAN DE VEN [80]). 39

FIGURE 3-7: TMP-FLUX PROFILE OF A FLUX STEP FILTRATION EXPERIMENT (ADAPTED FROM VAN DE MAREL [64]). 40

FIGURE 3-8: SCHEMATIC REPRESENTATION OF THE FLUX-STEP PROTOCOL AS DEVELOPED BY VAN DER MAREL ET AL [64]. 40

FIGURE 4-1: PORE SIZE DISTRIBUTION OF THE INVESTIGATED UF PES-PVP HOLLOW FIBRE MEMBRANE BASED ON PERMPOROMETRY MEASUREMENTS. 42

FIGURE 4-2: SEM IMAGES OF THE UF PES-PVP HOLLOW-FIBRE MEMBRANE (A) SHELL SURFACE AND (B-D) CROSS-SECTION AT THE SHELL SIDE OF THE NATIVE MEMBRANE AT VARIOUS MAGNIFICATIONS. 43

FIGURE 4-3: ZETA POTENTIAL AT INNER SURFACE OF THE INVESTIGATED UF PES-PVP UF HOLLOW FIBRE MEMBRANE AS A FUNCTION OF PH. 43

FIGURE 4-4: ZETA POTENTIAL OF CTAB-SILICA, TX100- SILICA AND SDS- SILICA AND THE PURE SURFACTANTS (SINGLE POINTS) AS A FUNCTION OF SURFACTANT CONCENTRATION VERSUS CMC AT PH 8. 44

FIGURE 4-5: RAYLEIGH NUMBERS FOR CTAB-SILICA, TX-100-SILICA AND SDS-SILICA SYSTEMS AS A FUNCTION OF SURFACTANT CONCENTRATION VERSUS CMC AT PH 8. OPEN SYMBOLS DENOTE MEASUREMENTS AFTER 1 HOUR AND CLOSED SYMBOLS DENOTE MEASUREMENTS AFTER 24 HOURS. 45

FIGURE 4-6: TOTAL FOULING RATE AND CRITICAL FOULING RATE FOR A FILTRATION OF 50 MG/L LUDOX TM-50 SIO_2 AT PH 8. OPEN SYMBOLS AND CLOSED SYMBOLS DENOTE FOULING RATES IN ASCENDING PHASE AND DESCENDING PHASE, RESPECTIVELY 48

FIGURE 4-7: PROFILE OF FOULING RATES FOR SDS-SIO_2 SYSTEMS AT VARIOUS SURFACTANT CONCENTRATIONS AT PH 8 AND 30°C. OPEN SYMBOLS AND CLOSED SYMBOLS DENOTE FOULING RATES IN ASCENDING PHASE AND DESCENDING PHASE, RESPECTIVELY 51

FIGURE 4-8: PROFILE OF FOULING RATES FOR CTAB-SIO_2 SYSTEMS AT VARIOUS SURFACTANT CONCENTRATIONS AT PH 8 AND 30°C. OPEN SYMBOLS AND CLOSED SYMBOLS DENOTE FOULING RATES IN ASCENDING PHASE AND DESCENDING PHASE, RESPECTIVELY 55

FIGURE 4-9: PROFILE OF FOULING RATES FOR TX100-SIO_2 SYSTEMS AT VARIOUS SURFACTANT CONCENTRATIONS AT PH 8 AND 30°C. OPEN SYMBOLS AND CLOSED SYMBOLS DENOTE FOULING RATES IN ASCENDING PHASE AND DESCENDING PHASE, RESPECTIVELY 59

FIGURE 4-10: SILICA REJECTION FOR FILTRATION OF SDS-SIO_2 SYSTEMS AT PH 8 AND 30 °C (CMC SDS: 8 MM). OPEN SYMBOLS AND CLOSED SYMBOLS DENOTE FOULING RATES IN ASCENDING PHASE AND DESCENDING PHASE, RESPECTIVELY. 61

FIGURE 4-11: SILICA REJECTION FOR FILTRATION OF CTAB-SIO_2 SYSTEMS AT PH 8 AND 30 °C (CMC CTAB: 0.92 MM). OPEN SYMBOLS AND CLOSED SYMBOLS DENOTE FOULING RATES IN ASCENDING PHASE AND DESCENDING PHASE, RESPECTIVELY. 62

FIGURE 4-12: SILICA REJECTION FOR FILTRATION OF TX100-SIO_2 SYSTEMS AT PH 8 AND 30°C. (CMC TX100: 0.24 MM). OPEN SYMBOLS AND CLOSED SYMBOLS DENOTE FOULING RATES IN ASCENDING PHASE AND DESCENDING PHASE, RESPECTIVELY. 62

FIGURE 4-13: SEM IMAGES- (A) CROSS-SECTION AND (B) SURFACE IMAGES OF UF PES-PVP MEMBRANE AFTER FILTRATION OF SDS-SILICA SOLUTION, AND WAS OBSERVED FOR ALL MEMBRANES AFTER FILTRATION. 63

FIGURE 4-14: PERMEABILITY RECOVERY (PR) FOR SDS-SIO_2 SYSTEMS AT VARIOUS SURFACTANT CONCENTRATIONS. OPEN SYMBOLS AND CLOSED SYMBOLS DENOTE FOULING RATES IN ASCENDING PHASE AND DESCENDING PHASE, RESPECTIVELY. 65

FIGURE 4-15: PERMEABILITY RECOVERY (PR) FOR CTAB-SIO_2 SYSTEMS AT VARIOUS SURFACTANT CONCENTRATIONS. OPEN SYMBOLS AND CLOSED SYMBOLS DENOTE FOULING RATES IN ASCENDING PHASE AND DESCENDING PHASE, RESPECTIVELY. 66

FIGURE 4-16: PERMEABILITY RECOVERY (PR) FOR TX100-SIO_2 SYSTEMS AT VARIOUS SURFACTANT CONCENTRATIONS. OPEN SYMBOLS AND CLOSED SYMBOLS DENOTE FOULING RATES IN ASCENDING PHASE AND DESCENDING PHASE, RESPECTIVELY 67

FIGURE B-1: FLUX AND TRANSMEMBRANE PRESSURE PROFILE FOR A COMPLETE FILTRATION EXPERIMENT. THE OPEN TRIANGLE SYMBOLS DENOTE FLUX, WHILE THE FULL CIRCLE SYMBOLS DENOTE THE TRANSMEMBRANE PRESSURE. 77

FIGURE B-1: EFFECT OF CONCENTRATION ON SDS REJECTION IN FILTRATION OF SDS-SILICA SYSTEMS. OPEN SYMBOLS AND CLOSED SYMBOLS DENOTE FOULING RATES IN ASCENDING PHASE AND DESCENDING PHASE, RESPECTIVELY. 78

FIGURE B-2: EFFECT OF CONCENTRATION ON CTAB REJECTION IN FILTRATION OF CTAB-SILICA SYSTEMS. OPEN SYMBOLS AND CLOSED SYMBOLS DENOTE FOULING RATES IN ASCENDING PHASE AND DESCENDING PHASE, RESPECTIVELY. 79

FIGURE B-3: EFFECT OF CONCENTRATION ON TX100 REJECTION IN FILTRATION OF TX100-SILICA SYSTEMS. OPEN SYMBOLS AND CLOSED SYMBOLS DENOTE FOULING RATES IN ASCENDING PHASE AND DESCENDING PHASE, RESPECTIVELY. 79

Index of Tables

TABLE 1: CHARACTERISTICS OF SURFACTANTS STUDIED. 26

TABLE 2: FILTRATION FEED SOLUTIONS AT PH 8 AND 30°C 31

TABLE 3: SILICA-SURFACTANT SUSPENSIONS FOR STATIC LIGHT SCATTERING AND ZETA POTENTAL MEASUREMENTS AT PH 8. 33

TABLE 4: CRITICAL FLUX FOR SDS-SIO_2, CTAB-SIO_2 AND TX100- SIO_2 SYSTEMS AT PH 8 & 30°C 49

Abbreviations

C_p	permeate concentration (mg/L)
C_f	feed concentration (mg/L)
CAC	critical association concentration (mM)
CMC	critical micelle concentration (mM)
CTAB	hexadecyltrimethylammonium bromide
F_{total}	total fouling rate ($m^{-1}s^{-1}$)
F_{crit}	critical fouling rate ($m^{-1}s^{-1}$)
ICP-MS	inductively coupled plasma mass spectrometry
IEP	isoelectric point
J_{crit}	critical flux
MWCO	molecular weight cut-off (kDa)
NP	nanoparticle
PES-PVP	polyethersulfone-polyvinylpyrrolidone
PR	permeability recovery (-)
PVP	polyvinylpyrrolidone
R	rejection (%)
SANS	small-angle neutron scattering
SiO_2	silica
SDS	sodium dodecyl sulphate
TMP	transmembrane pressure
TOC	total organic carbon (mg/L)
TX100	Triton X-100 (Polyethylene glycol *tert*-octylphenyl ether)
UF	ultrafiltration

Table of Contents

Acknowledgements i

Abstract ii

Index of Figures iii

Index of Tables vi

Abbreviations vii

1. INTRODUCTION 10

2. THEORY 12

2.1 Surface Chemistry of Silica Nanoparticles 12

2.2 DLVO Theory and Stabilization Mechanism 13

2.3 Equilibrium Surfactant Adsorption on Silica Surface 14

2.3.1 Equilibrium Adsorption of Ionic Surfactants onto Silica 16

2.3.2 Equilibrium Adsorption of Non-Ionic Surfactants onto Silica 19

2.3.3 Effect of CTAB on System Stability 21

2.3.4 Effect of SDS on System Stability 23

2.3.5 Effect of TX100 on System Stability 24

2.4 Colloidal Fouling & Concept of Critical Flux 27

3. EXPERIMENTAL 30

3.1 Feed Solutions 30

3.2 Membranes 34

3.3 Flux-Step Experiments 36

3.3.1 Analysis of the Result 39

4. RESULTS AND DISCUSSION 42

4.1 Membrane Characterisation 42

4.2 Particle Characterisation and Surface Modification 44

4.3 Filtration Experiments - Flux-Step Method 47

4.3.1 Fouling Development and Critical Flux 47

4.4 Influence of Surfactants on Fouling Rate 50

4.4.1 Influence of SDS on Colloidal Fouling Rate 50

4.4.2 Influence of CTAB on Colloidal Fouling Rate 54

4.4.3 Influence of TX100 on Colloidal Fouling Rate 58

4.5 Influence of Surfactant on Membrane Separation Properties 61

4.5.1 Influence of Surfactants on Silica Rejection 61

4.5.2 Influence of Concentration on Surfactant Rejection 63

4.6 Influence of Surfactant on Pure Water Permeability 64

4.6.1 Influence of SDS on Permeability Recovery of UF Membranes 64

4.6.2 Influence of CTAB on Permeability Recovery of UF Membranes 66

4.6.3 Influence of TX100 on Permeability Recovery of UF Membranes 67

5. CONCLUSIONS 69

6. RECOMMENDATIONS & FUTURE WORK 71

REFERENCES 72

Appendix A: Flux and Transmembrane Pressure for a Complete Filtration Experiment..... 77

Appendix B: Surfactant Rejection Data for Colloidal Silica Systems in SDS, CTAB and TX-100 solutions 78

1. INTRODUCTION

The rapid growth of nanotechnology has resulted in various implementations of nanomaterials in products or as process enhancers in manufacturing. Nanoparticles (NPs) may be classified via already known properties, the easiest being their chemical composition. Three main categories are usually distinguished [1]: i) pure metallic nanoparticles (e.g. Fe, Ag, Au,), (ii) metallic oxides or oxy-hydroxides (e.g. SiO_2, TiO_2), (iii) carbonaceous nanoparticles (e.g. nanotubes, fullerenes). Among them, SiO_2 and TiO_2 nanoparticles are already produced in very large quantities (10^2–10^3 tonnes/year) [1]. Although research on the impact of NPs on living organisms is still comparatively lesser compared to their wide range of applications, most researchers suggest that NPs are toxic. Furthermore, as a result of the increasing production and application, it is inevitable that the manufactured NPs will accumulate in the aqueous environment after usage. Therefore, there is a need to develop environmentally friendly technologies to remove NPs from potential drinking water sources in parallel with a sustainable growth of nanotechnology.

Over the last few decades, membrane technology has emerged as one of the most promising and reliable techniques in water purification, and has been proven to be effective in the removal of colloidal particles such as proteins, natural organic matter (NOM) and inorganic particles [2]. However, to date, the widespread usage of membrane technology is still limited by the fouling phenomenon. Furthermore, not much is known on the filtration and fouling behaviour of engineered NPs.

NPs are characterised by their size, which by definition are particles of any shape with at least one of the three dimensions between 1 and 100 nm [3]. Given their small sizes, these NPs have specific properties that are not found in bulk samples of the same material due to their high surface area to volume ratio, which meant that the role of surface interactions is significantly enhanced. Furthermore, the stability of the NP suspensions is also function of surface properties. Often, to improve the stability of such dispersions, different kinds of stabilizers are added to most commercially available NP suspensions. Adsorption of the stabilizer onto the surface of the NPs may change their surface character and consequently increase the repulsive interactions between the NPs thus preventing aggregation. Furthermore, it is imperative to consider that there are different types of stabilizers, which define the surface properties of NPs. Indeed, the effectiveness of particle stabilization is determined by the type of stabilizer, its affinity to the NPs, and concentrations of the NPs as well as stabilizers.

In membrane filtration, the role of surface interactions between foulants and membranes is indisputable. If a feed solution contains surface-active compounds, like stabilizers used for stabilization of the NP suspensions, its filtration behavior can significantly differ from the filtration process carried out without the presence of the surfactant. The type of surfactant determines the aggregation rate of the nanoparticles on the membrane surface by altering the interactions between particles. Process conditions like membrane type, pressure or temperature may also significantly change filtration behavior of the nanoparticles promoting aggregation near membrane surface.

Still, not much is known about the exact role of the surfactants during filtration of the NPs. In this study we will investigate influence of filtration conditions and the role of commercial surfactants additives on filtration behaviour of silica nanoparticles as model NPs. In this study, three industrially prominent surfactants (i) anionic: sodium dodecyl sulphate (SDS), (ii) cationic: hexadecyltrimethylammonium bromide (CTAB), and (iii) non-ionic: Triton X-100 (Polyethylene glycol *tert*-octylphenyl ether) will be used in varying concentrations to prepare SiO_2 NP suspensions, which later will be characterized and filtered.

2. THEORY

2.1 Surface Chemistry of Silica Nanoparticles

To understand the behaviour of colloidal fouling in membrane filtration, it is imperative to understand the surface chemistry of silica nanoparticles, and how this interaction changes when different surfactants are added to the silica suspension as an additive.

Bulk SiO_2 consists of a siloxane unit joined together in a tetrahedral lattice. Depending on the preparation of the surface and the nature of the solution, several different functional groups can be present at the surface [4]. Functional groups commonly associated with the SiO_2 surface are depicted schematically in Figure 2-1.

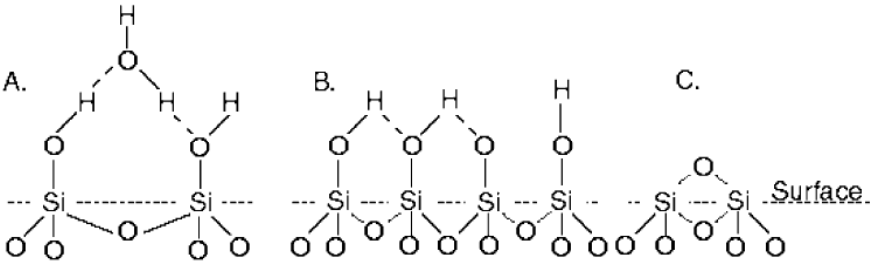

Figure 2-1: Schematic representation of the types of functional groups that occur on the silica surface (A) hydrated and (B) anyhydrous silanol groups are associated with the hydroxylated surface, whereas (C) siloxane-dehydrated groups occur mainly on the pyrogenic surface [5].

Like other mineral oxide surfaces, the surface charge character of SiO_2 is defined by the relative concentrations of H^+ and OH^- in solution, as shown by the following equations:

$$SiOH + H^+ \underset{K_1}{\Leftrightarrow} SiOH_2^+ \qquad \text{Equation 1}$$

$$SiOH + OH^- \underset{K_2}{\Leftrightarrow} SiO^- + H_2O \qquad \text{Equation 2}$$

The silica surface charge is determined by the relative magnitude of the equilibrium constants K_1 and K_2 in Equations 1 and 2. The isoelectric point (IEP) for SiO_2 occurs at approximately pH 2 [5, 6], and is somewhat dependent on the exact nature of the surface. The density of negative charges remains low until the solution pH reaches 6, however between pH 6 and 11 it increases sharply [7].

When analysing the SiO_2 surface charge, the structure of the oxide layer must be accounted for. Hydroxylated SiO_2 has a high density of hydroxyl groups with about ~4.5 OH nm^{-2} [5, 6] that are in close proximity of one another, leading to hydrogen bonding between the hydrogen of one hydroxyl group and oxygen of a neighbouring group (see Figure 2-1b). These hydroxyl hydrogen atoms are strongly bound at normal pH levels, resulting in the hydroxylated SiO_2 having low surface charge. Pyrogenic SiO_2, which is typically prepared by baking silicon wafers at high temperature in an oxygen atmosphere for a controlled amount of time, however has a lower density of hydroxyl groups of about ~0.7 OH nm^{-2} [5, 6] and a higher net charge than hydroxylated SiO_2. Indeed the presence of numerous siloxane-dehydrated groups as depicted in Figure 2-1c, will render the pyrogenic surface partially hydrophobic.

An aqueous nanoparticle dispersion is defined to be stable when the number of particles in a unit of time is constant with respect to time [8]. The stability of SiO_2 dispersions depends on the structure of SiO_2 surfaces and associated water molecules that define the characteristics of the near surface region. As discussed above, the hydrophilic silanol groups on the SiO_2 surface act as binding sites (H bonds) for water. The protonation and deprotonation of these silanol groups determine the surface charge of SiO_2 nanoparticles and the extent of the repulsive energy to keep them dispersed in solution [9].

Previous studies have also investigated the effects of pH, temperature and electrolytes on the stability of SiO_2 NP dispersions [10]. Metin et al [10] systematically investigated the stability of SiO_2 dispersion over a wide pH range of 2.5 to 10, whereby they observed a significant variation of SiO_2 nanoparticle surface structure. Also, they reported that the zeta potential of the SiO_2 NPs were around -45 mV as pH decreases from 10 to 6, but increased sharply with further decrease in pH. Nevertheless, they observed only a 1.36 factor increase in the effective particle diameter despite the significant pH decrease from 10 to 2, whereby they attributed the difference in particle size to the thickness and strength of the water bound layer to the SiO_2 particle [10].

2.2 DLVO Theory and Stabilization Mechanism

The small size of NPs results in a high surface area to volume ratio, with significantly enhances the role of surface interactions during membrane filtration. Broadly speaking, the stability of a colloidal system can be modified by two different mechanisms according to the type of repulsion forces that is generated: electrostatic stabilization and steric stabilization. Steric stabilization of colloidal particles is achieved by attaching (grafting or chemisorption) macromolecules to the surfaces of particles, which generates repulsion thus can be used to impart colloidal stability [11]. Electrostatic stabilization, on the other hand, is based on

electrostatic repulsion which is a consequence of interaction of the electrical double layer surrounding the particles [11].

In a membrane filtration process of colloidal systems, the deposition of nanoparticles on the membrane surface, which ultimately leads to membrane fouling can be described by colloidal stability theory. The classic Derjaguin-Landau-Verwey-Overbeek (DLVO) theory is the most simple and common theory to estimate colloidal stability, by combining the van der Waals attraction and electrical double layer repulsion between individual particles.

The role of pH, salt concentration and salt type on stability of the 22 nm silica nanoparticles is shown in **Figure 2-2**. This figure shows the relationship between total dimensionless interaction energy vs. distance between nanoparticles, proposed by Aimar et al [12]. In simple terms, stable colloidal suspensions typically have total dimensionless interaction energy higher than 10-15 kT [12]. These suspensions are stable and would not aggregate without reduction of the interaction energy in any conditions. For suspensions with interaction energy smaller than 3kT, the systems are unstable and particles will rapidly aggregate. For suspensions with total dimensionless interaction energy between 3 kT and 15 kT, they are semi-stable, as such their aggregation rate is strongly time and concentration dependent [12].

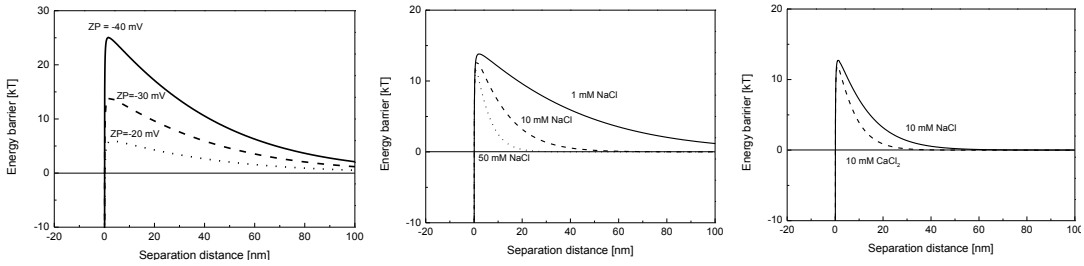

Figure 2-2: Interaction energy between two silica nanoparticles (Hamaker constant: $0.8 \cdot 10^{-20}$ J [13], particle diameter: 22 nm) calculated according to DLVO theory; (a) influence of the surface charge in 1 mM NaCl solution; (b) influence of the NaCl concentration for the nanoparticle surface charge of -30 mV; (c) influence of the cation valency for the nanoparticle surface charge of -30 mV.

2.3 Equilibrium Surfactant Adsorption on Silica Surface

The presence of surfactants is known to modify the surface chemistry of colloidal NPs by adsorbing on the surface of the NP. As such it is essential to recognise the different mechanisms and effect of adsorption of the various types of surfactant (e.g. anionic, cationic and non-ionic) on the substrate of interest. Indeed, the adsorption of surfactants onto hydrophilic surfaces such as SiO_2 from aqueous solutions has been studied rather extensively over the last few decades [4, 14-17] particularly as this model hydrophilic surface has been well characterised.

Adsorption isotherms are traditionally determined by solution depletion methods [4, 15, 16], where they are accomplished by mixing a surfactant solution with a given mass of adsorbate (i.e. SiO_2) of known surface area. At equilibrium, the surface excess is determined by the change in the bulk solution surfactant concentration. Adsorption can be considered as a partitioning of the adsorbate species between the interface and the bulk, and will occur if the interface is energetically favoured by the surfactant in comparison to the bulk solution. Γ_δ, (kmol/m^2) the adsorption density in the Stern plane, δ can be written as follows [18]:

$$\Gamma_\delta = lC\ exp\left(\frac{-\Delta\overline{G^o_{ads}}}{RT}\right) \qquad \text{Equation 3}$$

Where *l* is the effective length of the chain (m), C is the bulk concentration of the surfactant (kmol/m^3), R is the gas constant (JK^{-1}mol^{-1}), T is the absolute temperature (K) and $-\Delta\overline{G^o_{ads}}$ is the standard free energy of adsorption (J) [18]. The driving forces for adsorption is the sum of a number of contributing forces, whereby the major forces involved in surfactant adsorption are written as follows [19]:

$$-\Delta\overline{G^o_{ads}} = \Delta G^o_{elec} + \Delta G^o_{chem} + \Delta G^o_{c-c} + \Delta G^o_{c-s} + \Delta G^o_H + \Delta G^o_{H2O} \qquad \text{Equation 4}$$

where ΔG^o_{elec} (J) is the electrostatic interaction term, ΔG^o_{chem} (J) the chemical term due to covalent bonding, ΔG^o_{c-c} (J) the free energy gained upon association of methyl groups in the hydrocarbon chain, ΔG^o_{c-s} (J) the free energy due to interactions between the hydrocarbon chains and hydrophobic sites on the solid, ΔG^o_H (J) the hydrogen bonding term and ΔG^o_{H2O} (J) is the term owing to dissolution or solvation of the adsorbate species or any species displaced from the interface due to adsorption.

A number of different models for surfactant adsorption have been proposed over the years, relating to different combinations of surfactant and surface. These models attempt to describe systems that lie between two limiting cases; one limit corresponds to surfactant molecules in which the headgroups interact only weakly with the surface. The standard free energy of binding is insufficient to compensate for the loss of transitional entropy upon adsorption and surface coverage remains negligible until the concentration is very near the critical micelle concentration (CMC) [14]. A monolayer of surfactant does not form on the surface at any point in the isotherm. If a monolayer of surfactant were to form, the exposed hydrophobic surface would immediately attract a second later of adsorbed surfactant with an opposite orientation to avoid unfavourable hydrophobic interactions at the surface. This limit can be illustrated by the adsorption of non-ionic surfactants, such as polyethyleneglycol alkyl ethers with short ethylene oxide (EO) groups [20].

The second limiting case is the self-assembled monolayer (SAM) limit. In this limit, the interaction between the headgroup and the surface, together with the van der Waals interactions between closely packed chains, is sufficiently strong to create monolayer formation at concentrations orders of magnitude below the CMC [14]. At dilute concentrations, a second layer does not form because elimination of water-hydrocarbon contacts does not compensate for the loss of transitional entropy upon adsorption. As the surfactant concentration increases further, isolated molecules adsorb to the hydrophobic surface thus gradually increasing the surface coverage until it approaches a bilayer at CMC. This bilayer may be asymmetric, given the different nature of interactions in the two layers, as schematically shown in Figure 2-3.

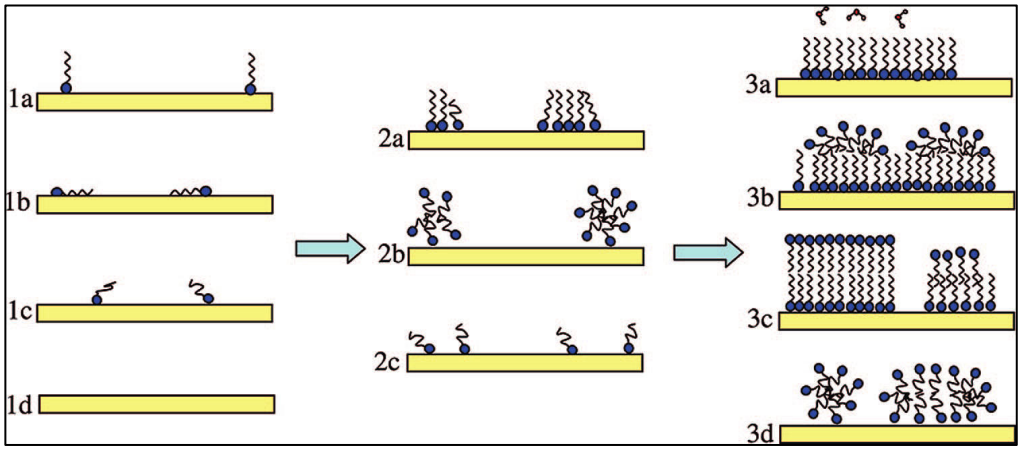

Figure 2-3: Cartoons displaying different morphologies that may form during the adsorption of a soluble surfactant to a clean hydrophilic substrate (1d). At very low coverage, the hydrocarbon chains of the adsorbed surfactant may be lie perpendicular to the surface (1a), parallel to the surface (1b), or be randomly oriented (1c). As the coverage increases, the molecules may be randomly distributed in a single layer (Langmuir behavior, 2c) or interactions between surfactant molecules may lead to the formation of hemimicelles (2a) or admicelles (2b). At high coverages, a range of structures are conceivable: monolayer (3a), hemimicelles on a monolayer (3b), bilayer (3c) or admicelles (3d) [14]

2.3.1 Equilibrium Adsorption of Ionic Surfactants onto Silica

Two principal models have been proposed in the literature to describe the adsorption of ionic surfactants to hydrophilic surfaces; (i) the two-step model [21, 22] and (ii) the four-region model [23] [24]. The general shape of the adsorption isotherm and the proposed molecular model for these two models are depicted in Figure 2-4. At the lowest concentrations (region I in both models), surfactant adsorbs onto oppositely charged surface sites via electrostatic interactions. At the highest concentrations (around the CMC), hydrophobic interactions result in the formation of aggregates of admicelles at the solid-water interface (region IV in both

models). The difference between these two models lies in the relative importance of electrostatic and hydrophobic interactions at intermediate concentrations. In the two-step model, there is only low coverage of isolated molecules bound electrostatically to the substrate, which nucleate the formation of admicelles in the steeply rising part of the isotherm. In the four-region model, there is stronger adsorption at lower concentrations leading to the formation of hemimicelles before the attachment of a second layer through hydrophobic interactions [14].

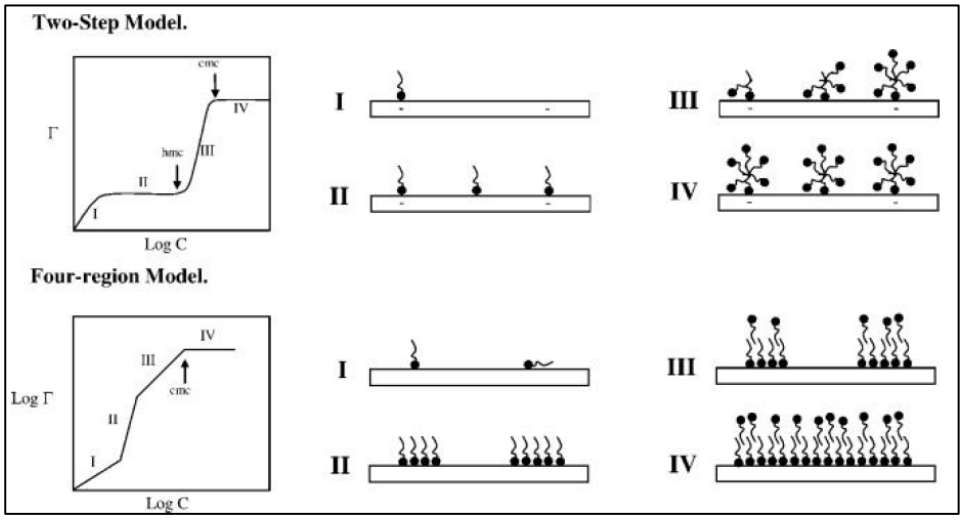

Figure 2-4: General shape of adsorption isotherm and proposed molecular model for two-step and four-region adsorption models [21, 23].

Adsorption of CTAB to silica without added salt has been extensively studied previously using a number of techniques including solution depletion [16], ellipsometry [25], optical reflectrometry [26-28] and neutron reflection [29]. An example of CTAB adsorption isotherm of CTAB obtained from the total internal reflection Raman scattering (TIR-Raman) technique is shown in Figure 2-5 [14]. In general, the surface excess and the overall shape of the isotherm are comparable to the two-step adsorption model or "Langmuir-S shape model. At concentrations just below CMC, formation of distinct aggregates was first detected, with the peak-to-peak distances between aggregates in the order of 10nm for concentrations above the CMC [28]. However, there is some disagreement in the literature regarding the shape of the aggregates. Some have reported spherical [30] (full micelle or a half-micelle of a flat monolayer) aggregates, and others have reported rod-like [28] aggregates, though the co-existence of both spherical and short rods was reported at a concentration just below the CMC [28]. Nevertheless, it is important to note that neutron reflectivity studies have established that the SiO_2 surface is always incompletely covered and that the thickness of the CTAB layer remain essentially constant in the range of 2.8 to 3.4 nm, for concentrations as low as 0.01 CMC [29].

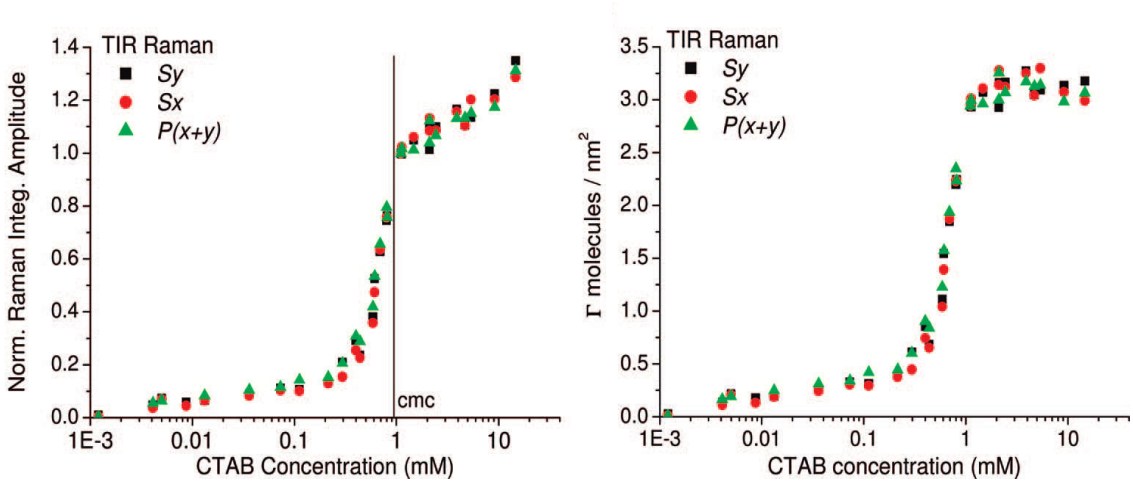

Figure 2-5: Adsorption isotherm of CTAB on SiO_2 as reported by Tyrode et al [14]

SDS, as an anionic surfactant, is not readily adsorbed onto negatively charged colloidal surface due to electrostatic repulsion [31, 32]. On the contrary, other groups have reported that SDS does adsorb onto negatively charged silica surfaces. Litton and co-workers [33, 34] attributed the adsorption of small amount of SDS on silica surfaces due to heterogeneities. Ahualli et. al [35] studied the adsorption of SDS on silica nanoparticles using small angle x-ray scattering (SAXS) and dynamic light scattering (DLS). They observed adsorption of SDS on the silica NP surface which resulted in a supercharging effect at the SDS-silica interface [35]. The hydroxyl groups on silica surface are not alike and can have different dissociation constants [36] thus causing non-uniformities on the surface. Nonetheless, anionic SDS can be made to adsorb at higher specific concentrations onto silica in the presence of pre-adsorbed polyethylene oxide (PEO) onto the surface [31, 37]). Maltesh et al [31] reported the adsorption isotherm of SDS onto silica in the presence of PEO with two different molecular weights at room temperature (23 ± 2°C) and neutral pH (6.5 to 7) as illustrated in Figure 2-6, and it can be observed that SDS adsorbed onto silica to a considerable extent regardless of polymer molecular weight.

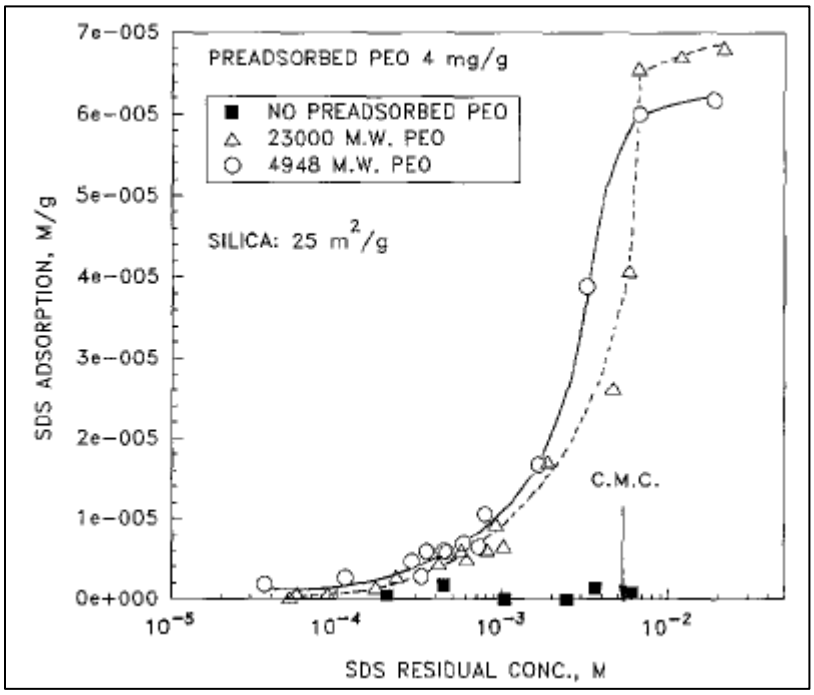

Figure 2-6: Adsorption of SDS onto silica and silica pretreated with polyethylene oxide at room temperature (23 ± 2°C) and neutral pH (6.5 to 7) [31]

2.3.2 Equilibrium Adsorption of Non-Ionic Surfactants onto Silica

The adsorption of non-ionic surfactants on solid-liquid interface has not been studied as extensively as the ionic surfactants. Generally the adsorption isotherms of non-ionic surfactants follow the Langmuir isotherm [38]. Non-ionic surfactants are physically adsorbed rather than electrostatically or chemisorbed. However, non-ionic surfactants differ from ionic surfactants in that, small changes in concentration, temperature or molecular structure of the adsorbent may induce a large effect on the adsorption. This is due to adsorbate-adsorbate and adsorbate-solvent interaction, which causes surfactant aggregation in bulk solution, thus leading to change in orientation and packing of surfactant at the surface [39].

From the pioneering work of Levitz and Van Damme [40, 41], it is known that non-ionic surfactants such as Triton X-100 (TX100) can form adsorbed micelles on silica surface and further work by Giordano-Palmino et al reported the adsorption of TX100 on silica nanoparticles [42]. The adsorption mechanism is as follows [40-42]; the first surfactant molecules adsorb on the silica surface through hydrogen bonding of their oxyethylene units to the surface silanols. Then an association process around these first adsorbed molecules occurs, leading to the formation of surface micelles, bounded by the same hydrogen bonds. This process occurs below the CMC, since adsorbed micelles have a lower free energy than free micelles. The shape of the adsorption isotherm of TX100 on two types of silica suspensions (Ludox HS40 and Syton W30) is shown in Figure 2-7 below [42].

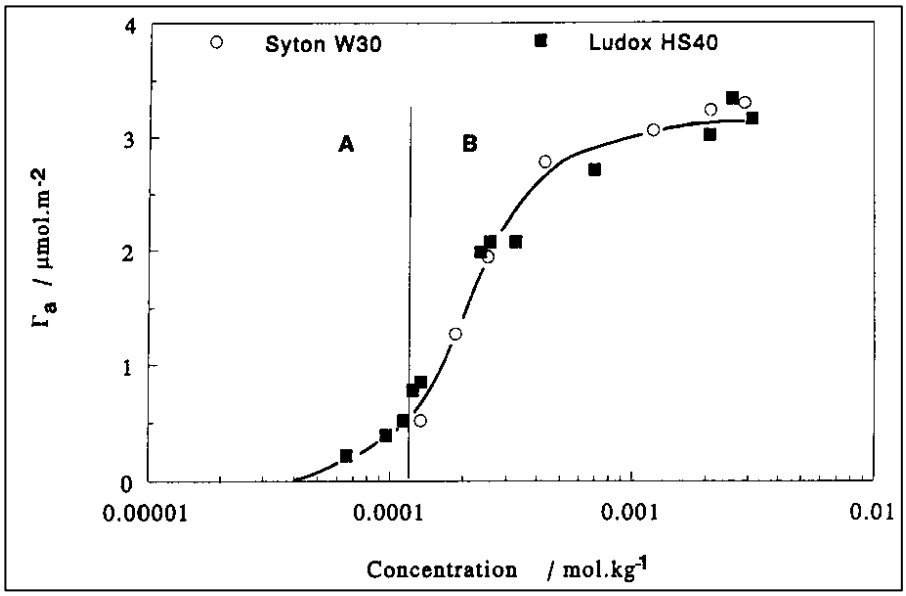

Figure 2-7: Adsorption isotherms of TX100 on Syton W30 and Ludox HS40 at pH 6 [42]

The adsorption of TX100 on silica surface is also highly dependent on the pH of the solution, as presented in Figure 2-8 [42]. Generally, the isotherms exhibit three characteristic regions: a slow increase of the adsorption at low equilibrium concentrations, a drastic rise in the adsorption at TX100 concentration of ~ 0.5 CMC and a plateau at concentration > CMC. However, as the pH increases, the surface charge increases thus decreasing the amount of undissociated silanol groups which are adsorbing sites for TX100 [42]. Nevertheless the same study also showed that the enthalpies of displacement (reported for two different pH values) was only dependent on the surface concentration of TX100, indicating that the main driving force of adsorption is due to the aggregation process, as expected in a “weakly bound adsorbate-adsorbent system”.

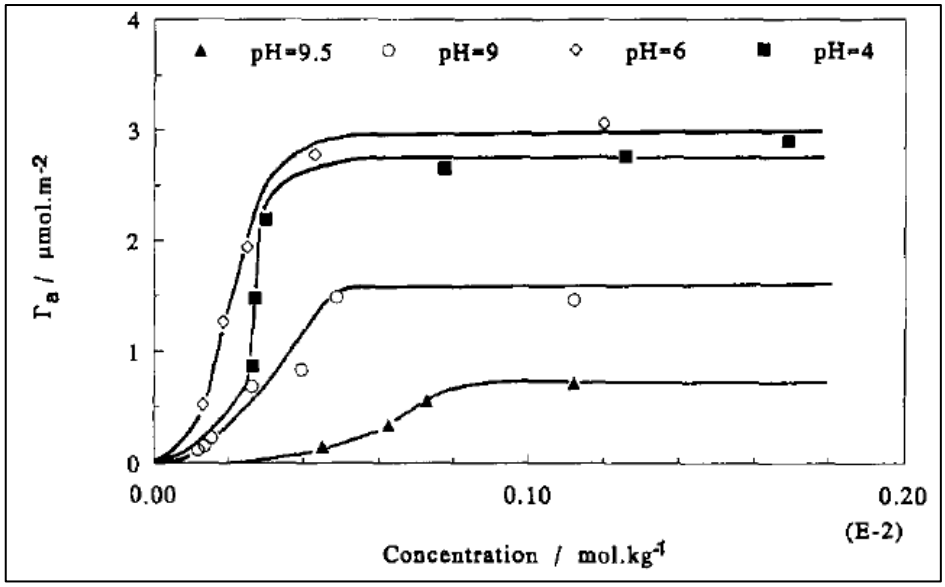

Figure 2-8: Adsorption isotherms of Triton X-100 on Syton W30 at various pH [42].

2.3.3 Effect of CTAB on System Stability

Properties of CTAB

Hexacetyltrimethylammonium bromide (CTAB) is a cationic surfactant, which is comprised of a cationic head and a hydrophobic tail, as depicted in Figure 2-9:

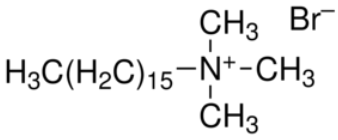

Figure 2-9: CTAB structure: cationic head and hydrophobic tail.

Due to the amphiphilic nature of surfactants, they are able to self-assemble into organised molecular assemblies or micelles. The concentration (actually an arbitrary concentration within a narrow range) above which micelles are formed is called the critical micelle concentration (CMC). Above the CMC, monomers and micelles exist in a dynamic equilibrium [43]. The CMC of CTAB has been reported to be 0.92 ± 0.05 mM [44] at 25^{o}C while Modaressi et al.[45] have cited 0.89 mM, Gao et al [46] with 0.92 mM, and Maiti et al [47] have given 0.8 mM at the same temperatures. CTAB is easily dissociated into cationic CTA^{+} and bromide ion (Br^{-}) and its speciation is not influenced by pH changes [48]. However, the Krafft temperature or critical micelle temperature of CTAB, which is the minimum point below which it remains in crystalline form is about 25^{o}C [49].

Effect of CTAB on Particle-Particle Surface Interaction

The adsorption of CTAB on SiO_2 NPs could affect aggregation of these particles due to the following reasons; CTAB, which is composed of a cationic polar head and a hydrophobic tail could aggregate with negatively charged SiO_2 by both surface charge neutralisation. When surfactant concentration increases, hydrophobic interactions between surfactant chains will occur [4, 26, 50]. Each individual or combined effect would make SiO_2 NPs less stable, and thus aggregate [4, 26, 50]. With regards to the structures of CTAB formed on SiO_2 surface, several groups have presented simplified schemes of CTAB 'tail-to-tail' bilayer and multilayer on SiO_2/water interface, however the real structure of CTAB-coated SiO_2 is more versatile and complicated [4, 5, 16].

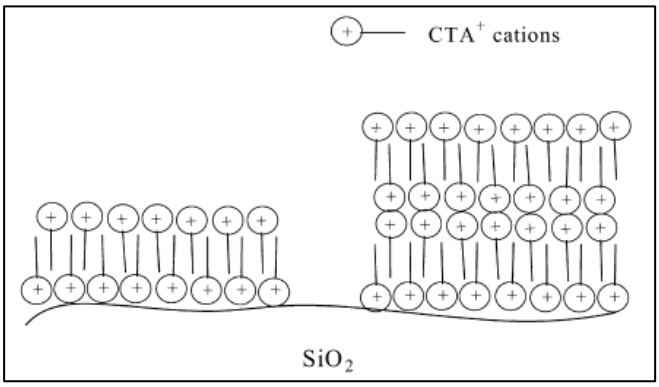

Figure 2-10: Simplified scheme of CTAB 'tail to tail' bilayer and multilayer formation on SiO_2-water interface [50].

In a recent study by Liu et al [44], they proposed the following interactions between SiO_2 NPs and CTAB as follows: initially small quantities of CTAB would form a monolayer on the SiO_2 surface controlled by electrostatic interaction between positively charged surfactant head groups and siloxane groups ($-SiO^-$). Furthermore, it is known that adsorption of CTAB on SiO_2 surface could overcome micelles formation in bulk water [50, 51], which could elucidate why good aggregation can still be obtained at CTAB concentrations near or higher than CMC.

However, when the concentration of CTAB is much higher than the CMC (e.g. 100 mM), the bilayer structure owing to hydrophobic interaction between surfactant hydrocarbon tails could be formed, and which may lead to the restabilization of CTAB-SiO_2 NP-water systems [44]. Liu and co-workers [44] proposed a possible scheme of the aggregation of 0.15% wt SiO_2 NPs (Klebosol 30R50 colloidal silica suspension) as concentration of CTAB increases (Figure 2-11). At CTAB concentrations much below the CMC (<0.1 mM), the repulsion between negatively charged surface reduces but it may not be enough to destabilize the suspension (Step 1). When the quantity of CTAB increases, the negative surface charge of the SiO_2 could further reduce and aggregation may occur even before complete charge neutralisation (Step 2). By continuously increasing the quantity of CTAB, the SiO_2 surface would be neutralised and the hydrophobic interaction could still cause aggregation (Step 3). However when the CTAB concentration is high enough, a bilayer of CTAB could envelop the particle surface thus restabilise the nano-SiO_2 suspension (Step 4).

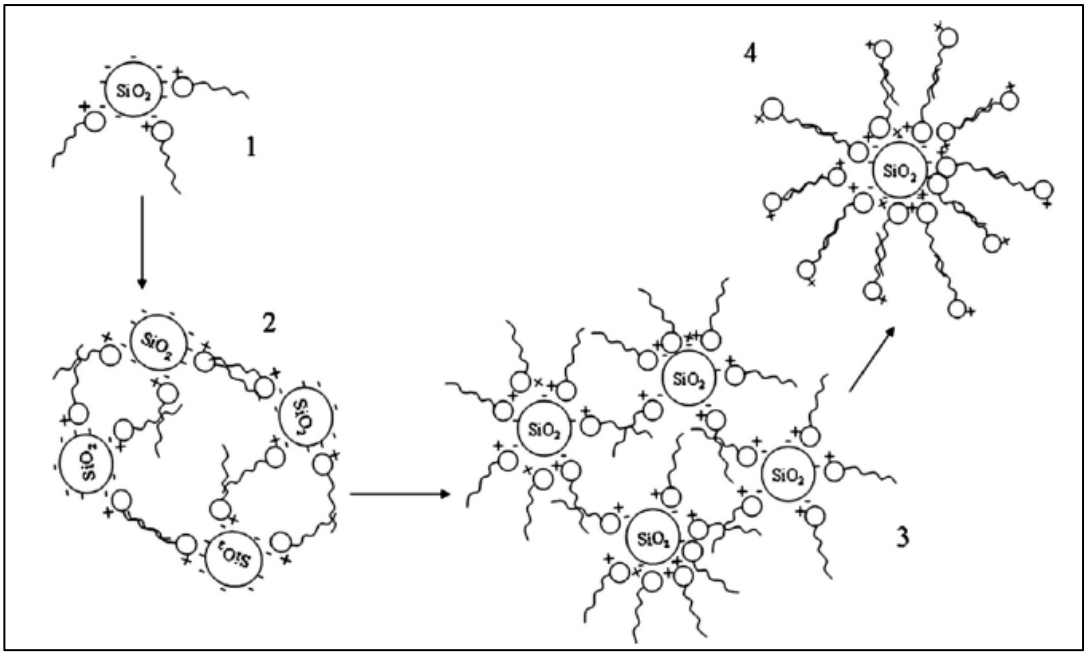

Figure 2-11: Possible simplified scheme of CTAB-SiO_2-water interface as proposed by Liu and co-workers [44]. Counterions Br- are omitted for clarity.

2.3.4 Effect of SDS on System Stability

Properties of SDS

Sodium dodecyl sulphate (SDS) is an anionic surfactant, which is comprised of an anionic sulphate head and a 12-carbon hydrophobic tail, as depicted in Figure 2-12 below:

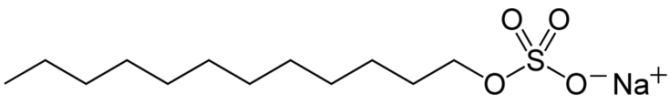

Figure 2-12: Structure of SDS: anionic head and hydrophobic tail.

Singh & Song [52] reported that the CMC of SDS in water was determined to occur at approximately 8mM at room temperature using conductivity measurements. This value concurs with other measurement methods such as calorimetry [53], surface tension [54] and light scattering [55]. The shape of SDS micelles formed is influenced by ionic strength; micelles are reported to be cylindrical at aqueous solutions with 0.6 M NaCl [56], and are spherical in aqueous solutions with lower ionic strength. The surfactant is highly soluble in aqueous solutions at room temperature because it is well above the Krafft temperature for dodecyl sulphate (8-9^{o}C) [52]. Micelle radius is reported to be approximately 2.2 ± 0.2nm [57].

Effect of SDS on Particle-Particle Surface Interaction

As mentioned previously, several studies have shown that SDS could be adsorbed on colloidal SiO_2 surface. Ahualli et al [35] observed that the effective charge of the negatively charged silica NPs and hence the repulsion between particles. Furthermore, other groups have reported that a small amount of SDS is adsorbed onto silica surface due to the heterogeneities on the colloid surface [33, 34]. The existence of charge heterogeneity on the colloid surface has been found to decrease the electrostatic repulsions for the same average surface potential [28, 33]. As such, adsorption of the negatively charged SDS to mask the heterogeneities on the colloid surface may result in a more uniform and higher negatively charged surface thus resulting in greater electrostatic repulsion between the SDS adsorbed colloidal particles [52].

2.3.5 Effect of TX100 on System Stability

Properties of Triton X-100

Triton X-100 (TX100) is a non-ionic surfactant that has a hydrophilic polyethylene oxide (PEO) chain (on average it has 9-10 ethylene oxide units) and an aromatic hydrocarbon hydrophobic group, which is a 4-(1,1,3-3-tetramethylbutyl)-phenyl group, as depicted in Figure 2-13 below.

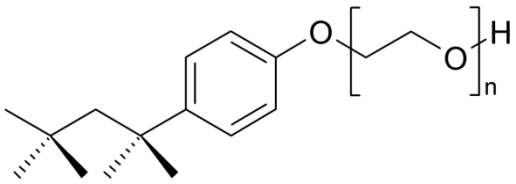

Figure 2-13: Structure of non-ionic surfactant Triton X-100.

The CMC of TX100 have been reported to range from 0.24 mM [42] to 0.33 mM [58] at room temperature. The size of TX-100 micelles has been reported to have an average radius of 20-25 Å [59]. Other studies reported that TX100 micelles are oblate ellipsoids, with the major axis of about 45 Å and a minor axis of about 25 Å [60],

Effect of TX100 on Particle-Particle Surface Interaction

The structure of TX100 adsorption layers formed on silica surface at pH 6.5 was studied in detail by fluorescence spectroscopy [40, 41]. At low concentrations, TX100 is adsorbed on the silica surface as individual molecules with hydrocarbon radicals oriented at a certain angle to the surface. The range of TX100 concentrations correspond to the hydrophobization of the silica surface. At later stages of adsorption, hydrophobic interactions between hydrocarbon

radicals of non-ionic surfactant molecules adsorbed on the solid surface and those present in the bulk solution come into play. These interactions result in the formation of surfactant associates on the solid surface and since the polar groups are oriented towards the bulk solution, the silica surface becomes hydrophilic [61].

According to Levitz et al [40, 41] at low degrees of surface coverage (0.17-0.5), the adsorbed phase is a fragmented medium made of small aggregates which are similar to the spherical micelles formed by TX100 in micellar solution. However with high degrees of surface coverage (above 0.8) the adsorbed phase may be considered as a continuous medium, forming either extended bilayer assemblies or an interconnected network of pseudomicellar aggregates [41].

Table 1 summarises the main characteristics of the surfactants used in this study.

Table 1: Characteristics of surfactants studied.

Surfactant name	**Acronym/ Abbreviation**	**Structural Formula**	**CMC (mM)**	**Temperature @ CMC (K)**	**Krafft temperature (K)**
Cetyltrimethylammonium bromide	CTAB	$C_{16}H_{33}N^{+}(CH_3)_3Br^{-}$	0.89 - 0.92 [44, 45, 47]	298	298 [25]
Sodium dodecyl sulfate	SDS	$C_{12}H_{25}NaO_4S$	~8 [52]	298	290 [25] 282 [28]
Polyethylene glycol *tert*-octylphenyl ether	Triton X-100	$C_{14}H_{22}O(C_2H_4O)_n$ (n=9-10)	0.24 - 0.33 [42, 58]	298	<0 ($64^{o}C$ [1])

[1] Cloud point temperature of Triton X-100 is $64^{o}C$ [33]

2.4 Colloidal Fouling & Concept of Critical Flux

Fouling is in inevitable consequence in membrane processes. It is one of the major phenomena responsible for the reduction of flux to far below the theoretical capacity of the membrane hence the deterioration of the process performance. Colloidal fouling in membrane filtration systems is a complex process as there are different physical and chemical phenomena that occur simultaneously. The complexity of colloidal fouling is generally attributed to hydrodynamic conditions, inter-particle interactions, and particle-membrane interactions, which would be eventually reflected by the fouling properties on the membrane surface.

The simplest approach to consider filtration of particles is to consider a single colloid driven towards the porous surface by a convective flux, J. Mass transfer during filtration is then the result from a balance between the convective term and a diffusive term described by an interaction potential which can be modelled using, for instance the DLVO theory [62]. Equation 5 describes the net flux of particles towards the membrane, N, which is the combined effect of convective flux which drives the particles towards the membranes, and fluxes which tend to remove particles away from the wall effects hence termed “dispersive” effects [63].

$$N = J\phi - D\frac{d\phi}{dz} - \frac{D}{kT}\phi\frac{dV}{dz} \qquad \text{Equation 5}$$

On the right hand side of Equation 5, $J\phi$ is the convective contribution to the flux; the second term $D\frac{d\phi}{dz}$ represents the diffusive contribution whilst the third term $\frac{D}{kT}\phi\frac{dV}{dz}$ represents the term for migration of solutes/particles due to surface interactions with the membrane [62]. This is shown schematically in Figure 2-14, where F_v is the convective contribution to the flux, F_d is the diffusive contribution, and F_a and F_r represent the electrostatic interaction due to attractive and repulsive forces, respectively.

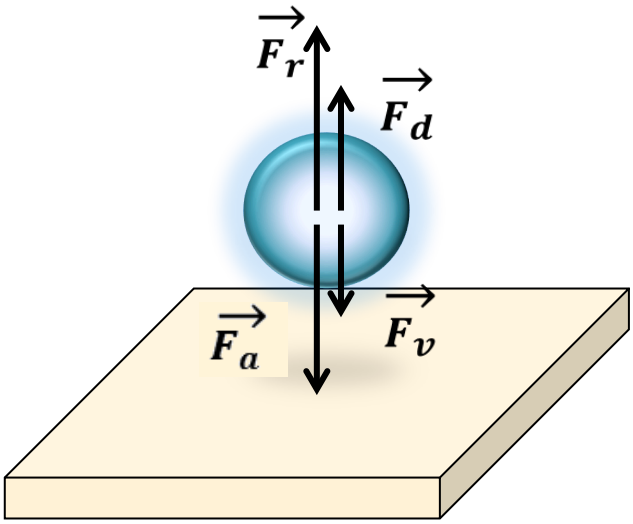

Figure 2-14: Schematic of the forces that are involved in a dead end filtration process.

According to Aimar et al. [12], from a microscopic point of view, fouling starts to occur when the convective forces of these particles towards the membrane is equal to or exceeds the total force imposed by the diffusive and electrostatic interaction between the particle and membrane surface.

A widely accepted methodology to investigate fouling behaviour in membrane filtration systems is to identify the so-called critical flux, $J_{crit.}$ [64-66]. The critical flux is generally considered as the flux above which particle deposition occurs on the membrane surface, as the drag force acting on the particle is not high enough to overcome the repulsion between the particle and the membrane [62].

According to Field et al [67], there are two forms of critical flux. The so-called strong form of critical flux is the highest flux at which the permeability of a fouling solution is the same as the permeability for pure solvent (water) at the same flux. The weak form is said to exist when the permeability of the fouling solution is lower than that for the pure solvent under subcritical operation, but is independent of the imposed flux ([67]. In the real world, feeds which result in the strong form of flux is rarely observed [67].

Operation above the critical flux causes fouling. Critical flux can be a good indicator for performance of the membrane system to keep its productivity constant with advantage of operational cost [66]. It is also often in many industrial UF installations, that it is necessary to operate the system under sub-optimum conditions, which may mean operation below or above the critical flux. As such, it is also imperative to understand the fouling behaviour over a broad range of sub- and super-critical fluxes.

The most widely accepted method to determine critical flux is usually based on the flux-step method. In this method, flux is increased in small steps while change in the transmembrane pressure (TMP) is monitored. Several groups have also performed decremental flux steps in some critical flux tests to evaluate the effects of fouling history on hysteresis[68, 69]. There are varying flux-step methods, some are carried out with uninterrupted flux increments [65], while others incorporate flow decreases or stoppage steps for relaxation [64] and backwash steps [70, 71].

Van der Marel et al [64] developed an improved flux-step method, which includes an intermediate relaxation step as a cleaning mechanism, to determine the critical flux and critical flux for irreversibility in a membrane reactor. Their method applied successive flux-steps of constant increment up to a maximum and back. Each flux is applied until a certain amount of permeate is collected, and reveals a constant TMP when operated below the critical flux [64]. An advantage of this method is that they could discriminate between reversible and irreversible fouling. They also observed that the influence of fouling history in the MBR was reduced by incorporating an intermediate relaxation step in their process.

Typically in UF processes, there are four mechanistic models that are used to describe fouling [72]. Complete blocking assumes that particles close off pore entrances thus preventing flow. Intermediate blocking is similar to complete blocking however it assumes that only a portion of the particles seal off pores while the rest accumulate on top of other deposited particles. Cake filtration occurs when particles accumulate on the surface of the membrane in a permeable cake, which increases in thickness and adds resistance to flow. Standard blocking, on the other hand, assumes that particles accumulate on the inside of the membrane wall, which constricts the pores over time and the permeability decreases [73].

In a colloidal system, it is unquestionable that the presence of surfactants in a silica suspension would have an influence on the interaction between the colloidal particles, as well as influence on the particle-membrane surface interaction, which subsequently would have an impact on the filtration process. Nonetheless, the effect of surfactants on colloidal fouling in membrane processes has not been very well studied and as such in this work, we attempt to study systematically the influence of different types of surfactant and concentration on colloidal fouling in a semi-dead end UF system. Considering the significance of the critical flux in membrane filtration process, a flux-step approach was used to investigate the effect of surfactants on the critical flux. Essentially, the systematic, step-wise nature of this method could act as a probe to determine the critical fluxes of the various surfactant-silica systems. Furthermore, to be industrially relevant, it is imperative to understand the effect of flux on filtration and fouling behaviour as filtration processes are typically operated in a constant flux and often at sub-optimal critical fluxes.

3. EXPERIMENTAL

3.1 Feed Solutions

Colloidal silica Ludox TM-50 (22 nm) in form of 50% silica nanoparticles, purchased from Sigma-Aldrich, was used as model silica nanoparticles. All solutions were prepared using ultrapure water (Milli-Q, >18.2 MOhm). ACS grade NH_4HCO_3-$(NH_4)_2CO_3$, HCl and NaOH (Sigma Aldrich) were used to adjust the pH and ionic strength of the solutions used in this research. Sodium dodecyl sulfate (SDS), hexacetyltrimethylammonium bromide (CTAB) and Triton X-100 (TX100) were purchased from Sigma-Aldrich. All chemicals were used without further purification.

Filtration feed solutions used in this work were prepared in following way: Feed solutions were prepared with Milli-Q water with different concentrations of surfactants as summarized in Table 2. 1mM of NH_4HCO_3-$(NH_4)_2CO_3$ buffer solution was then added to maintain a pH 8 feed solution. Subsequently, the commercial suspension of Ludox particles was introduced to obtain 50 mg/L of silica nanoparticles in the feed solution. This concentration was selected to maintain a realistic colloidal concentration found in actual wastewater, as well as to keep the concentration of surfactants to silica in a range where there is more than sufficient surfactant to adsorb on silica. Furthermore, at this concentration, we are also able to characterize the feed with the techniques available. Lower silica concentrations will render the characterization techniques unsuitable. At the end of the procedure, pH was adjusted again with either 0.1 M NaOH or 0.1 M HCl, if necessary. The temperature of the feed solution was maintained at 30°C by immersing in a temperature-controlled stirred water bath. Filtration experiments were carried out immediately after preparation of the feed solution.

Note: The Krafft temperature or critical micelle temperature of CTAB, which is the minimum point below which it remains in crystalline form is about 25°C [49]. Therefore, all experimental conditions and surfactant/SiO_2/water systems were prepared and measured at a temperature higher than 25°C to ensure that CTAB was sufficiently dissolved in solution.

Table 2: Filtration feed solutions at pH 8 and 30°C

Silica-Surfactant Solutions	Surfactant Concentration		Silica Concentration (mg/L)
	mM	c_{surf} /c_{CMC}	
SiO_2	--	--	50
SiO_2-SDS	1	0.125	50
	4	0.5	50
	8	1	50
	8	1	0
SiO_2-CTAB	0.115	0.125	50
	0.46	0.5	50
	0.92	1	50
	0.92	1	0
SiO_2-TX100	0.025	0.125	50
	0.1	0.5	50
	0.24	1	50
	0.24	1	50

The scattering intensity of the silica nanoparticles in the presence of CTAB, SDS and TX100 surfactants of various concentrations were measured by static light scattering using Dawn® Heleos™ 8, supplied by Wyatt Technology Corporation. Light scattering data collection and analysis was performed using Astra® 6.1 (Wyatt Technology Corportion), to determine its relative scattering intensity in relation to pure silica nanoparticles solution. The aim of this measurement was to obtain a qualitative quantity which can be related to the size of the aggregates, i.e. the higher the scattering intensity, the larger the aggregates compared to pure silica nanoparticle

As colloidal systems are optically inhomogenous, there is net light intensity in directions deviating from the direction of propagation, or scattering. The principle of a light scattering experiment is given in Figure 3-1, whereby the intensity, I_θ (Wm^{-2}) of the light scattered by a sample at an angle θ (^{o}) is measured by a detector at a distance r (m) from the beam. The detection plane is given by incoming beam and sample-detector line and is usually taken horizontally. The scattering volume, V_S (m^3) in this case is defined by the cross section of the incoming beam and the observed beam [74].

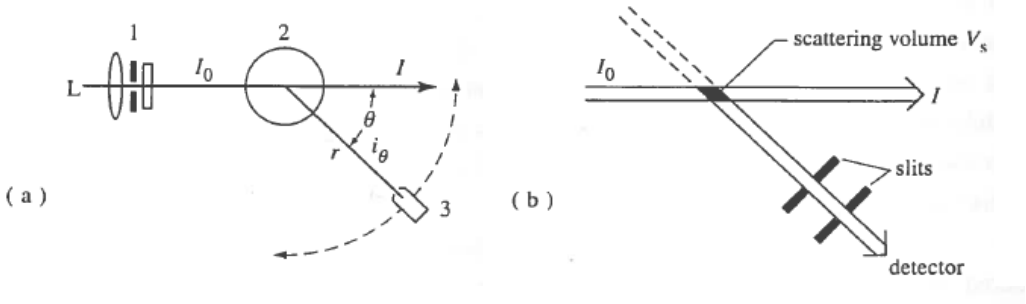

Figure 3-1: (a) Top view of the principle of light scattering set-up. L: light source; 1: Filters, lenses; 2: Sample cell; 3: Mobile detector. (b) Definition of scattering volume Vs in a cross-section of the incoming beam and detection beam [74].

Scattering intensity, i_θ is obtained by considering the amplitudes of all the scattered waves, and by taking into account their phases, and it can be given by the following Rayleigh equation [74]:

$$i_\theta = \frac{I_\theta}{V_S} = I_o(n_d^2 - n_m^2)^2 \frac{\pi^2 N v^2}{r^2 \lambda_o^4} \quad [Wm^{-5}] \qquad \text{Equation 6}$$

where I_o (Wm^{-2}) is the incoming light intensity, n_d and n_m (-) are the refractive index of particle and medium, respectively; N is the number of particles per cubic meter of scattering volume (particles/m^3); where each particle has a volume v (m^3), and λ_o is the wavelength (nm). Indeed, the Rayleigh theory predicts that light scattering depends strongly on particle radius, *a*, namely as $v^2 \sim a^6$. A quantity called the *Rayleigh ratio*, defined in Equation 7

$$R_\theta = i_\theta r^2 / I_o \quad [m^{-1}] \qquad \text{Equation 7}$$

is the reduced scattered intensity under angle θ, and may be regarded as the relative scattering per steradian. This value relates to the size of the nanoparticles and allows an observation of the aggregation in the presence of surfactants [74].

In this study, static light scattering measurements of nanoparticle-surfactant solutions were carried out at an angle of 90^o with a wavelength of 658 nm at 30$\pm$1°C. They were also undertaken for surfactant-only solutions to account for static light scattering of surfactant monomers and/or micelle. All measurements were repeated at least three times, and the average of the *Rayleigh ratios* was obtained.

Electrophoretic mobility measurements of the silica nanoparticles were determined via electrophoresis measurements using Malvern ZetaSizer 3000Hsa (Malvern Instruments) to obtain the zeta potential of the nanoparticles. Zeta potential is derived from the accumulation of electrical charges at a solid-liquid interface where an electrical double layer is formed [75].

In addition to being experimentally accessible, the zeta potential can be correlated with particle stability; i.e. highly stable colloidal systems are characterized by high zeta potentials while less stable systems show low zeta potentials [76]. Indeed the deposition of particles onto membrane surfaces is also controlled by the zeta potential of the nanoparticles and membrane surface [76].

In the electrophoresis process, when an electric field is applied across an electrolyte, charged particles in the electrolyte are attracted towards the electrode of opposite charge. However, viscous forces acting on the particles tend to oppose this movement. When equilibrium is reached between these two opposing forces, the particles move with constant velocity (electrophoretic velocity). Zeta potential of the particles was approximated by the measured electrophoretic mobility using the Smoluchowski equation [76].

Both light scattering and zeta potential measurements were conducted using 50 mg/L nanoparticles solution prepared by dilution of commercial surfactants in ultrapure water (Refer to Table 3). The nanoparticle concentration in the feed and permeate solutions was measured by inductively coupled plasma mass spectrometry (ICP-MS) (Thermo Fisher X-series 2), evaluating the total silicon content, while the surfactant concentration was evaluated using total organic carbon (TOC) analysis.

Table 3: Silica-surfactant suspensions for static light scattering and zeta potental measurements at pH 8.

Silica-Surfactant Solutions	**Surfactant Concentration**		**Silica Concentration (mg/L)**
	mM	**c_{surf} /c_{CMC}**	
SiO_2	--	--	50
SiO_2 – SDS	0.5	0.0625	50
	1	0.125	50
	2	0.25	50
	4	0.5	50
	8	1	50
	16	2	50
SiO_2 – CTAB	0.05	0.0625	50
	0.115	0.125	50
	0.23	0.25	50
	0.46	0.5	50
	0.92	1	50
	1.8	2	50

Silica-Surfactant Solutions	Surfactant Concentration		Silica Concentration (mg/L)
	mM	c_{surf} /c_{CMC}	
SiO_2 –TX100	0.0125	0.0625	50
	0.025	0.125	50
	0.05	0.25	50
	0.1	0.5	50
	0.24	1	50
	0.48	2	50

3.2 Membranes

Membranes used in the experiments were commercially available inside-out polyether sulfone-poly vinyl pyrrolidone (PES-PVP) ultrafiltration (UF) membranes supplied by Pentair X-Flow BV (UFCLE type, MWCO 150 kDa). UF filtration modules were prepared by potting 15 hollow-fibre membranes (inner diameter 0.8 mm) in a PVC tube (outer diameter 120 mm) with two-component polyurethane glue to give a final filtration area of 52 cm^2 (Figure 3-2).

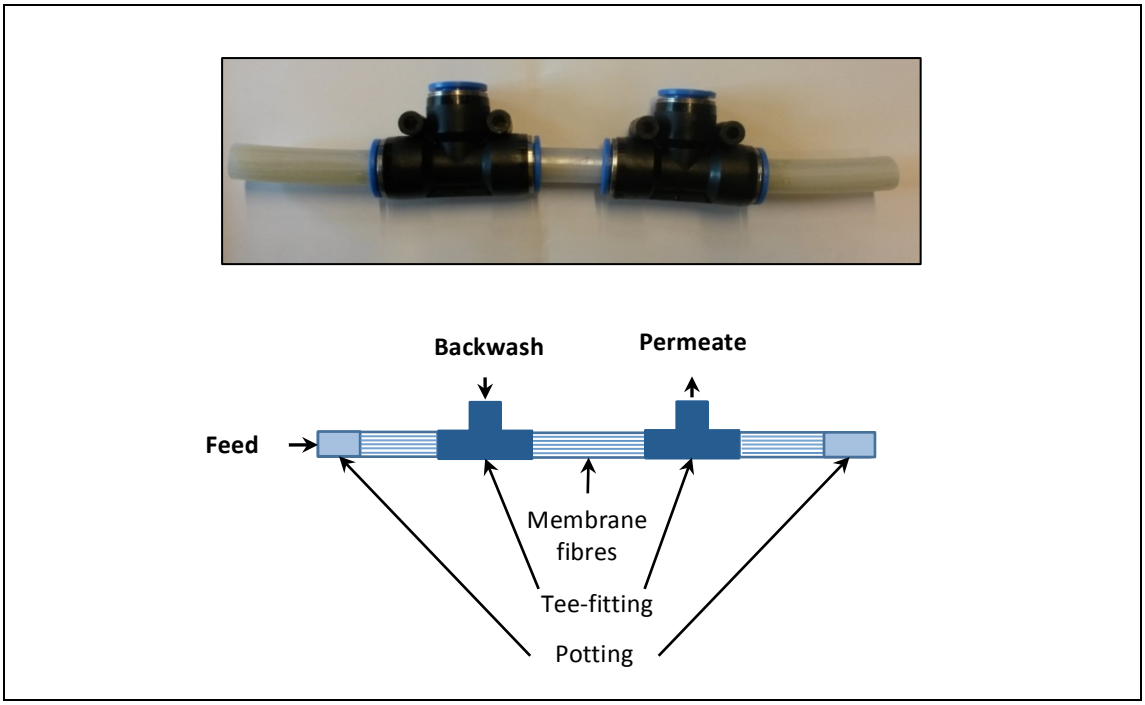

Figure 3-2: An example of a filtration module and a schematic describing the module operating in a semi dead-end configuration.

The membrane was characterized in term of pure water permeability, scanning electron microscopy analysis (SEM), inner surface charge and pore size distribution. For SEM analysis, small pieces of the dry native membrane and fouled membrane were sputtered with

thin platinum layer using a Jeol JFC-1300 fine coater. The SEM images were taken using high resolution SEM microscope (Jeol JSM-6000F).

The pore size distribution of the membrane was measured using the permporometry technique. This technique is based on the controlled stepwise blocking of pores by condensation of a vapour, linked with the simultaneous measurement of oxygen flux through the membrane [77]. It is imperative to select a vapour, typically present as a component of a gas mixture, which should not swell the membrane. At a relative pressure equal to unity, all the pores are filled with liquid and no gas permeation occurs. When relative pressure is reduced, the condensed vapour is removed from the largest pores according to the Kelvin equation:

$$\ln \frac{P}{P_o} = \left(-\frac{\gamma v}{RT}\right) \cos\theta \left(\frac{1}{r_{k1}} + \frac{1}{r_{k2}}\right) \qquad \text{Equation 8}$$

where P is the vapour pressure (Pa), P_o the saturated vapour pressure (Pa), γ the surface tension (N/m), v the molar volume of the liquid (m^3/mol), R is the universal gas constant, T the temperature (K), the contact angle θ (^{o}) and r_K is the Kelvin radius describing the curvature of the liquid-gas interface (m). As the Kelvin radius (r_K) is related to the specific vapour pressure, a measurement of gas flow can provide information about the number of these specific pores and thus allowing pore size distribution to be obtained [78]. A schematic representation of the permporometer setup is shown in Figure 3-3. Along both sides of the membrane, a mixture of condensable gas and non-condensable gas was flushed; on one side air was used as the non-condensable gas while nitrogen was used on the other side. Cyclohexane was used as the condensable vapour in our setup and the practical measurement range of this method is 0.5 – 50 nm.

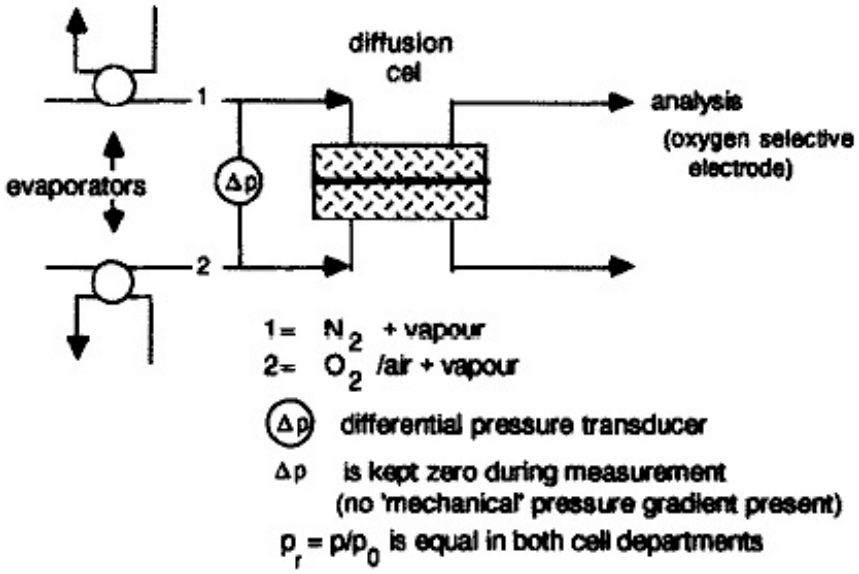

Figure 3-3: Schematic representation of permporometer setup [77].

The surface potential of the inner membrane was determined via streaming potential measured with an electrokinetic analyser SurPASS (Anton Paar GmbH). Similarly, the surface potential is also dependent on the properties of the solid surface and the surrounding electrolyte medium; and can provide information on the charge and adsorption characteristics of the membrane [75]. In the streaming potential measurement, the salt solution is forced to flow through a porous plug material across a channel formed by two plates or down a capillary, by an external pressure. The liquid in the channel having a net charge, flows in the channel thus gives rise to a streaming current thereby generating a potential difference [75]. In our experiments, 1 mM KCl was used as a background electrolyte solution; the pH was adjusted using aqueous 0.1 M NaOH and 0.1 M HCl solutions. Zeta potential was calculated according to the Fairbrother-Mastin equation (Equation 9).

$$\zeta = \frac{dU}{dp} \cdot \frac{\eta}{\varepsilon_r \varepsilon_0} \cdot \frac{\kappa_h R_h}{R_{cell}} \qquad \text{Equation 9}$$

where ζ is the zeta potential (V), dU/dp the slope of streaming potential versus pressure ($V.Pa^{-1}$), η the electrolyte viscosity (Pa.s), ε_r the dielectric constant of electrolyte, ε_0 the vacuum permittivity ($CV^{-1}m^{-1}$), κ_h the specific conductivity of the electrolyte solution (S/m), and R_h and R_{cell} the electrical resistance (Ω) of the cell filled with high salt concentration and with the working salt concentration, respectively [79].

3.3 Flux-Step Experiments

All the flux-step permeation experiments were performed using a flux-step method adopted from van der Marel [64] in a semi dead-end filtration mode using the 'OSMO Inspector' filtration setup developed and automatized by Convergence Industry B.V. (Enschede, The Netherlands) and shown schematically in Figure 3-4, and a pictorially in Figure 3-5.

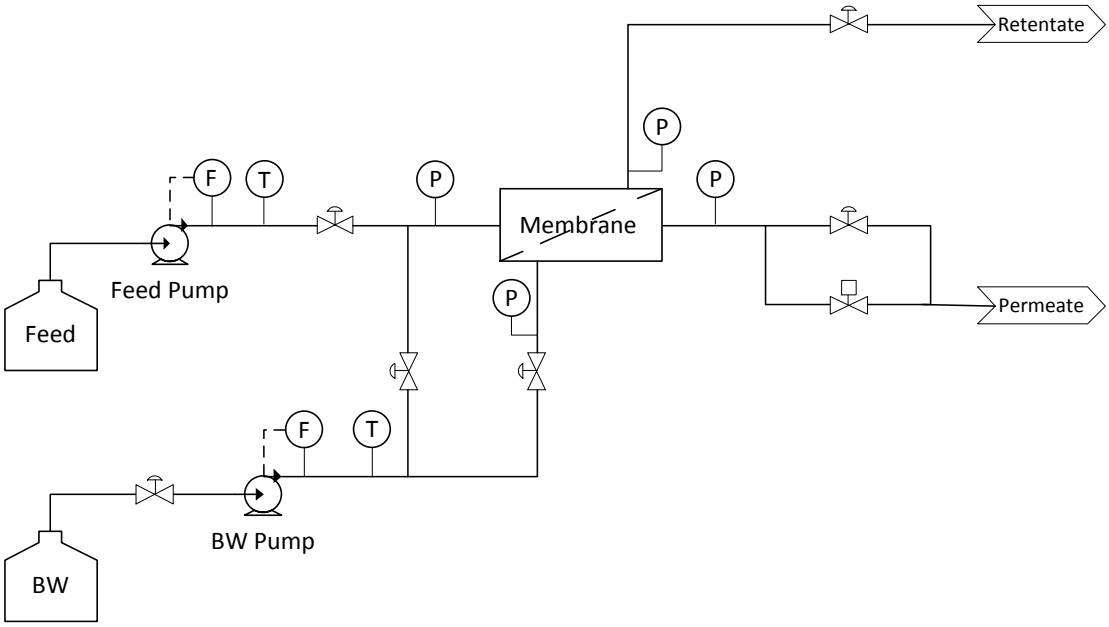

Figure 3-4: Flowsheet of the OSMO filtration setup. BW and Feed are backwash water and feed water tanks respectively. The flows are controlled by two mass flow controllers (F). Pressure (P) is measured in the feed, backwash, permeate and retentate. Temperature is monitored in the feed and downstream of the backwash pump.

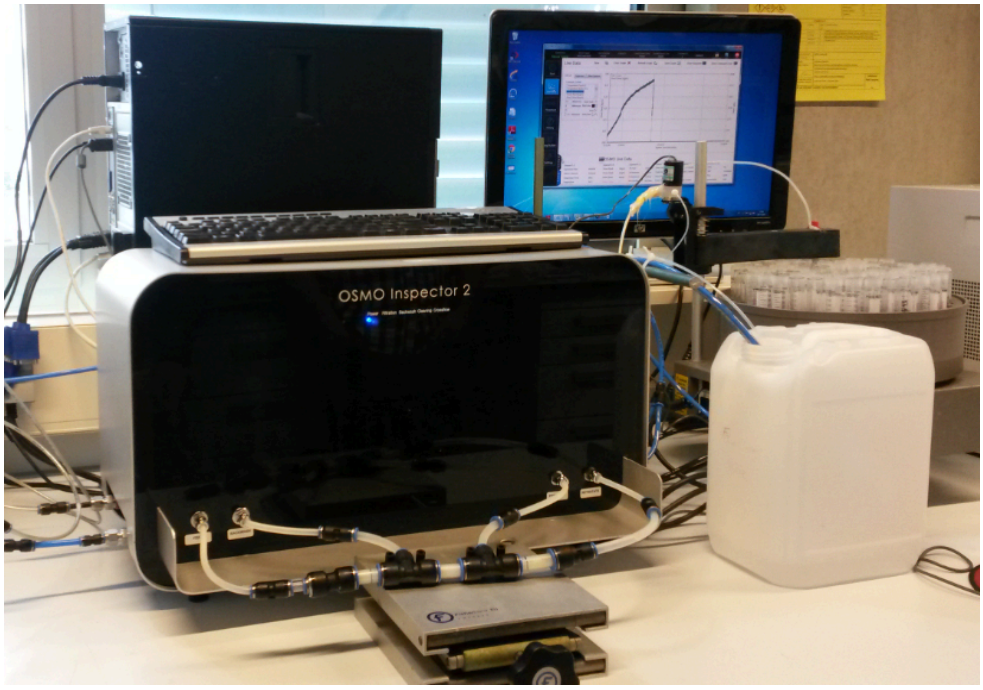

Figure 3-5: Picture of the OSMO Inspector filtration setup.

The system contains a feed and backwash pump (Liquiport® NF100, KNF). By means of solenoid switching valves (Plast-o-matic), the water from the backwash tank can be fed either

to the feed or permeate side of the membrane, enabling the integration of automatic pure water flux experiments. Two high precision mass flow controllers (Cori-Flow^{TM} model M15, Bronkhorst Cori-Tech, NL.) are installed to measure and control the feed and backwash fluxes. Before filtration of the nanoparticle solution, the feed solution was left in a temperature controlled stirred water bath to allow the temperature to equilibrate at 30°C.

It is noted that glycerol is used to preserve the UF membranes by preventing pore collapse. The membranes are immersed in glycerol solution after preparation which stays in the pores. Since glycerol does not evaporate the pores cannot collapse as a result of evaporation and/or capillary forces. As such, to avoid the leaching of glycerol into the permeate samples, ultrapure water was filtered through the membrane modules at high pressure (2 bar) for 30 mins to remove the glycerol. Following that, the pure water flux of the individual module was checked to be approximately the same as the expected from pure water flux experiments. Due to the nature of the potting procedure, there was always a difference in the membrane surface area between individual modules, hence pure water flux varied to a small extent for every module. Only modules with about similar pure water fluxes were chosen ($\pm$15%) for further filtration with silica nanoparticles.

After the determination of initial pure water flux, the fouling experiments were started. The OSMO software was programmed to perform filtration-backwash cycles at fluxes from 0.1 kg/hr, with an increment of 0.1 kg/hr at each step up to 1.0 kg/hr, followed by a downward step from 1.0 to 0.1 kg/hr with a similar decrement of 0.1 kg/hr. As such a single filtration experiment is comprised of 10 ascending and 9 descending flux-steps. At the onset of each flux-step, the sequence is described as follows and is shown schematically in Figure 3-6:

i. Pure water permeability check at 0.2 kg/hr, 0.4 kg/hr and 0.8 kg/hr. The purpose of this step was to observe and investigate the effect of irreversible fouling of the membrane module;
ii. Flush the shell side with feed solution at 1 kg/hr for 1 minute, to fill the module with feed solution;
iii. Filtration with feed solution to obtain a permeate volume of 100 mL;
iv. Flush the shell side with pure water at 2.5 kg/hr for 1 minute, to remove the permeate from the shell side of the module; and
v. Backwash of membrane module with Milli-Q water at 2.5 kg/hr for 1 minute, to clean the membrane before the next flux-step.

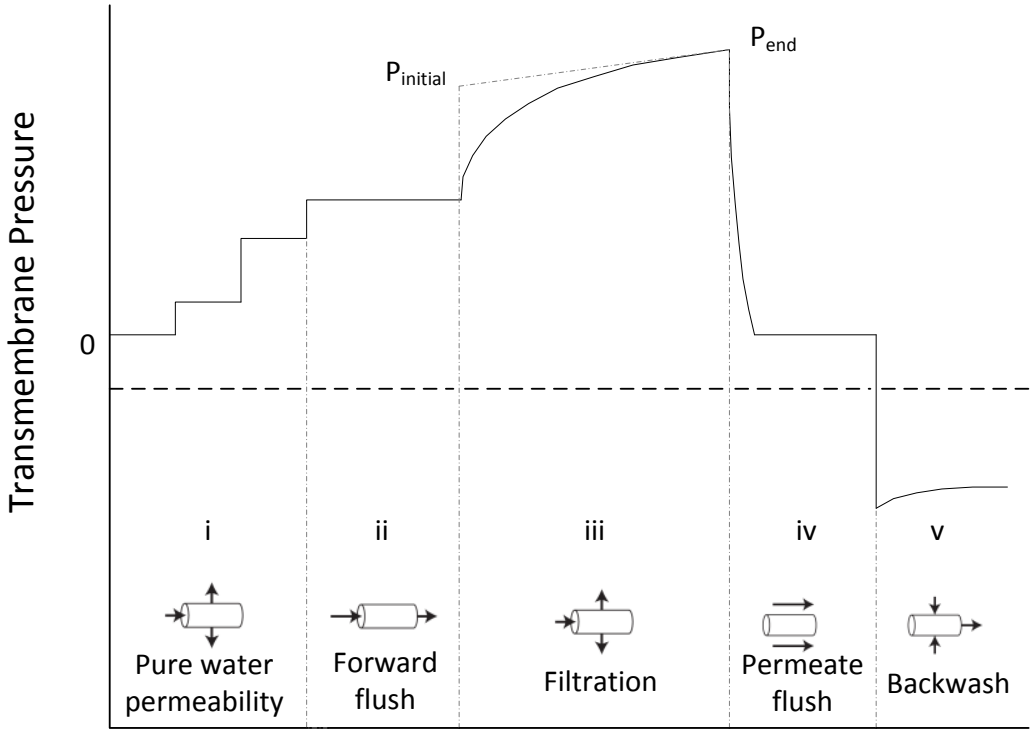

Figure 3-6: Layout of one filtration-backwash cycle (Adapted from van de Ven [80]).

Filtration at each flux step was applied until 100 mL of permeate sample were collected. The silica and surfactant content of the samples were determined using ICP-MS and total organic carbon (TOC), respectively. 50 mL of permeate was collected for ICP-MS analysis, and 20 mL of permeate was collected in glass vials for TOC analysis. ICP-MS and TOC analyses were carried ut by Dutch water supply company Vitens NV.

3.3.1 Analysis of the Result

The evolution of transmembrane pressure (TMP) with time at each flux step, J_H was monitored, as shown schematically in Figure 3-7. The total fouling rate (F_{total}) which includes both reversible and irreversible fouling, can be calculated by the change in TMP with time at each flux step, J_H, i.e. P_{end} (Pa) and $P_{iinitial}$ (Pa) in Figure 3-8, using Equation 10.

Total fouling rate, $$F_{total} = \frac{dR_{total}}{dt} = \frac{P_{end} - P_{initial}}{\eta J_H} \frac{1}{\Delta t}$$ Equation 10

where R is the resistance (m^{-1}), J is the flux ($m^3m^{-2}s^{-1}$), η is the viscosity of the permeate corrected to experimental temperature (Pa s), t is the flux-step duration (s) and $P_{initial}$, P_{end}, and P_2 are the pressures as defined above. The total fouling rate, F_{total} is inversely proportional to the permeate viscosity, as such the permeate viscosity has been corrected with respect to 25° C.

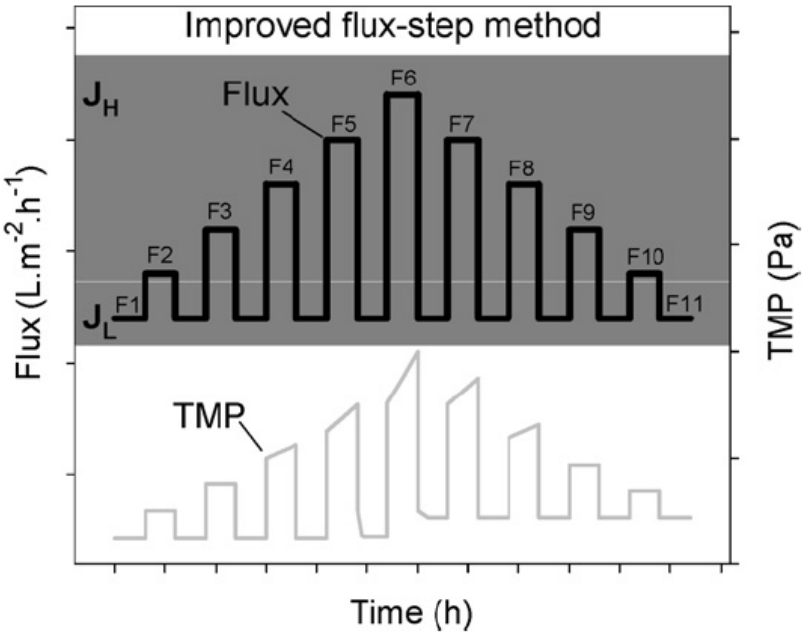

Figure 3-7: TMP-Flux profile of a flux step filtration experiment (adapted from van de Marel [64]).

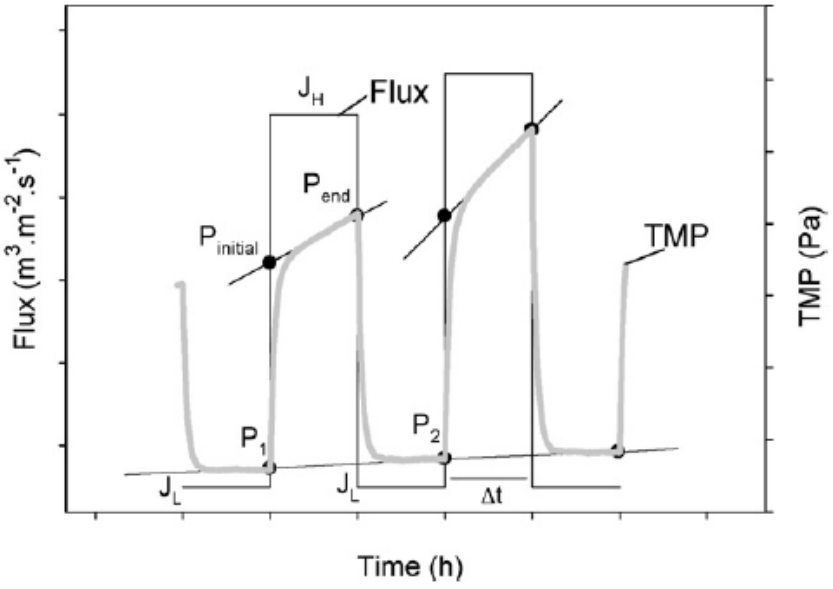

Figure 3-8: Schematic representation of the flux-step protocol as developed by van der Marel et al [64].

To determine the critical flux in the filtration experiments, an arbitrary minimum increase in TMP of 10 Pa min^{-1} was used [64], whereby the critical fouling rate (F_{crit}) was calculated for each flux by applying this minimum increase in TMP into Equation 10 above. The critical fouling rate is an asymptote to zero with increasing flux, as a fixed TMP with time is divided by the flux. The critical flux is achieved when F_{total} *becomes equals to* F_{crit}.

The fouling rate can be obtained graphically by plotting the increment in membrane resistance due to fouling against time, and calculating the gradient of the linear portion [35]. From this method of analysis, the total fouling rate and critical fouling rate for each flux-step were determined. Pure water permeability of the membrane module was determined from the slope of the flux against TMP and the comparison or the pure water permeability in between flux steps allows identification of the irreversible fouling rates.

The removal efficiency, or rejection of silica nanoparticles (R_{SiO2}) and surfactant (R_{surf}) were defined as:

$$R_{SiO2} = \left(1 - \frac{C_{p,SiO2}}{C_{f,SiO2}}\right) \times 100\% \quad \text{Equation 11}$$

$$R_{surf} = \left(1 - \frac{C_{p,surf}}{C_{f,surf}}\right) \times 100\% \quad \text{Equation 12}$$

where C_p and C_f (mg/L) represent the concentration of SiO_2 and surfactant in the permeate and feed, respectively.

The permeability recovery (PR) of the membrane was defined as:

$$PR = \frac{Pe_{bw}}{Pe_w} \quad \text{Equation 13}$$

where Pe_{bw} and Pe_w ($Lm^{-2}h^{-1}bar^{-1}$) are the pure water permeability of the membrane after backwashing and the pure water permeability of the clean membrane, respectively. The purpose of this parameter was to ascertain the effect of surfactants and extent of irreversible fouling on the membrane.

4. RESULTS AND DISCUSSION

4.1 Membrane Characterisation

Pore size distribution of the investigated ultrafiltration PES-PVP membrane is presented in Figure 4-1. According to permporometry measurements, pore diameter varies between 5 nm and 45 nm, while the mean pore diameter is found to be 24 nm. SEM images in Figure 4-2 show that membrane appears to be highly asymmetric with the selective layer of several hundred nanometers thickness on the inside. As can be seen from the SEM images, the membrane is far from an ideal membrane where pores are cylindrical, straight and all of equal dimensions. Zeta potential of the inner surface of the membrane as a function of pH is plotted in Figure 4-3 below. It is noted at pH 8, i.e. the pH at which filtration experiments were conducted, the zeta potential of the inner surface of the membrane was about -24 ± 3 mV.

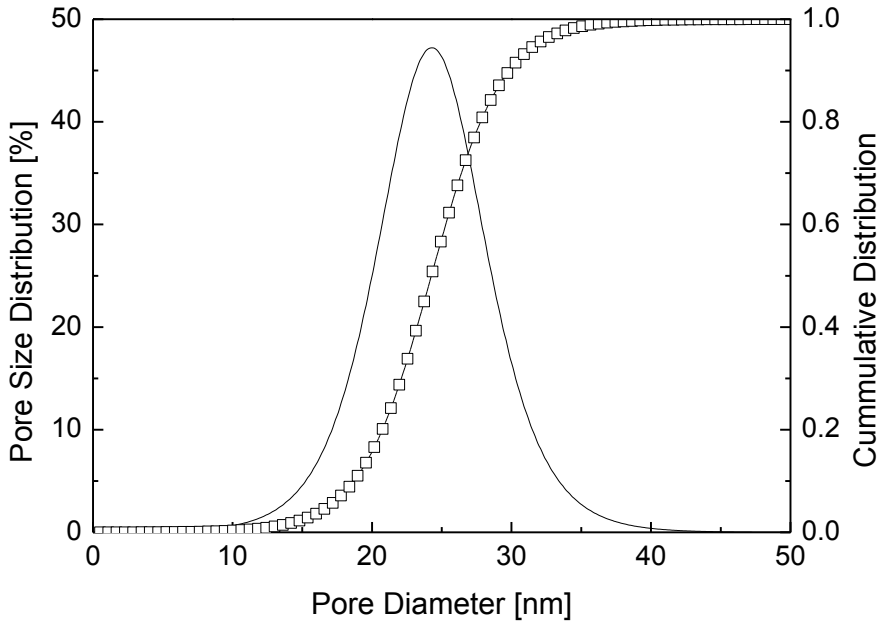

Figure 4-1: Pore size distribution of the investigated UF PES-PVP hollow fibre membrane based on permporometry measurements.

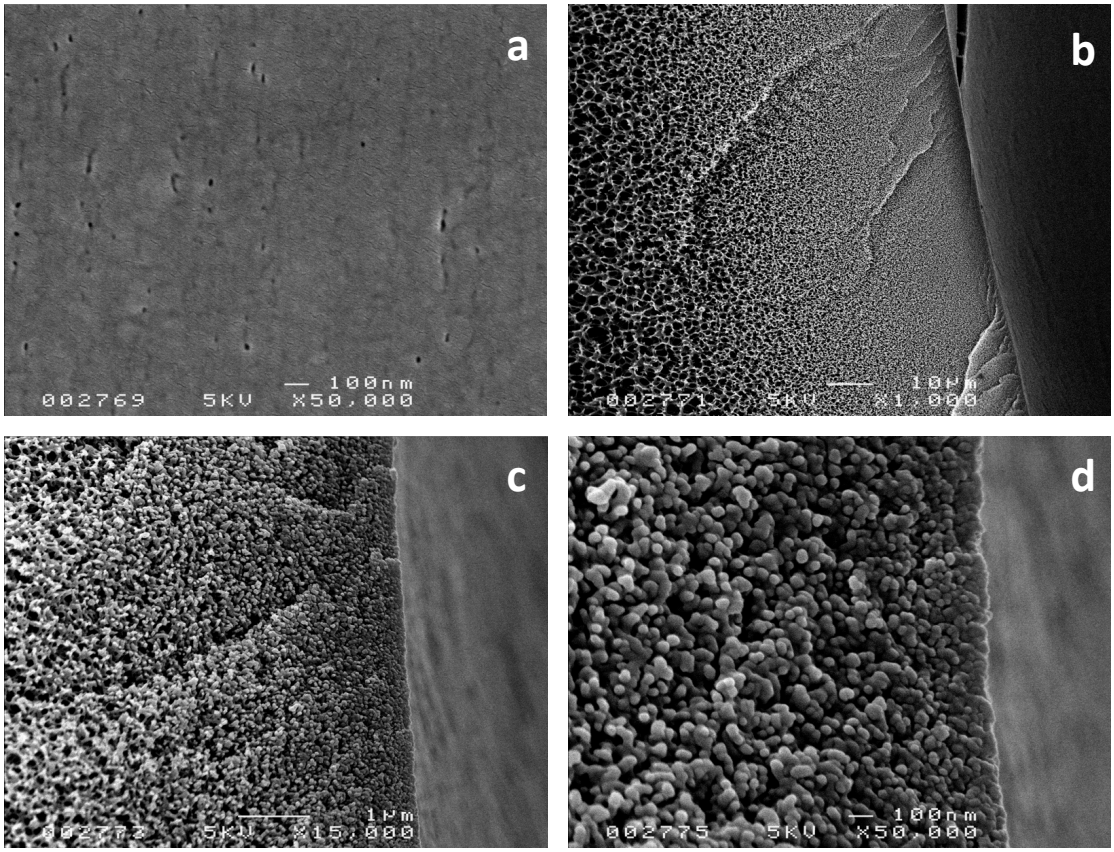

Figure 4-2: SEM images of the UF PES-PVP hollow-fibre membrane (a) shell surface and (b-d) cross-section at the shell side of the native membrane at various magnifications.

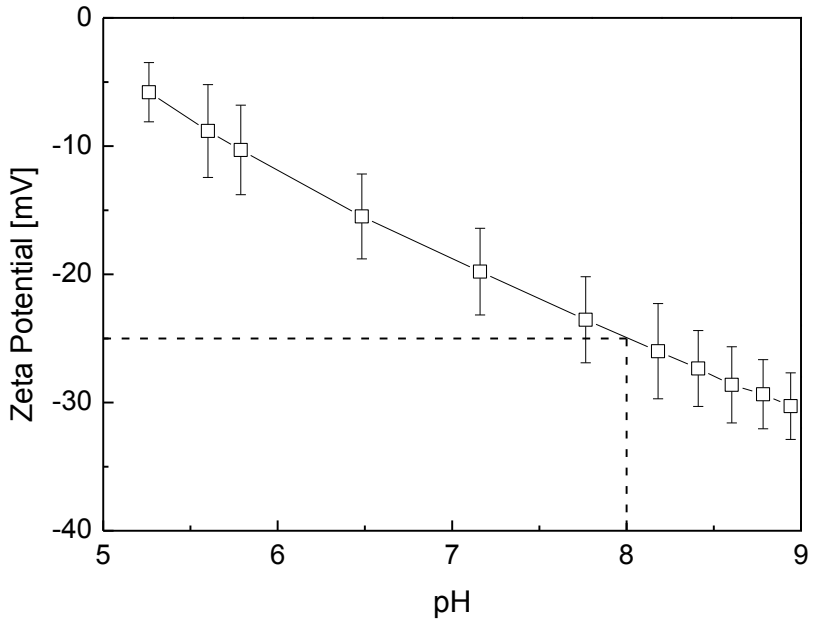

Figure 4-3: Zeta potential at inner surface of the investigated UF PES-PVP UF hollow fibre membrane as a function of pH.

From literature, we note that PES-PVP membranes are considered to be hydrophilic, as the purpose of PVP as an additive was to increase the hydrophilicity of the PES membrane as well as to prevent macrovoid formation. The most common method to determine the hydrophilicity or wettability of a membrane is by contact angle measurements, unfortunately, hydrophilicity of the membrane could not be characterised using this method as the membrane is in a hollow fibre configuration.

4.2 Particle Characterisation and Surface Modification

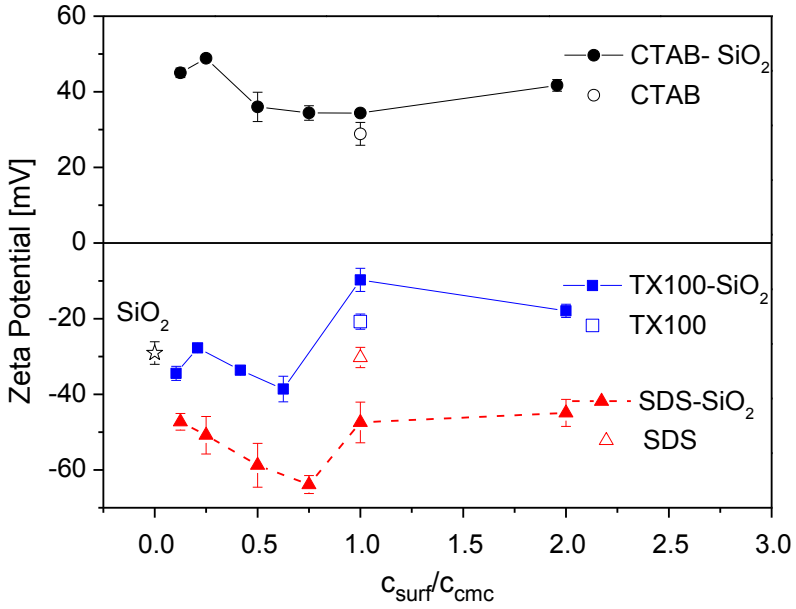

Figure 4-4: Zeta potential of CTAB-silica, TX100- silica and SDS- silica and the pure surfactants (single points) as a function of surfactant concentration versus CMC at pH 8.

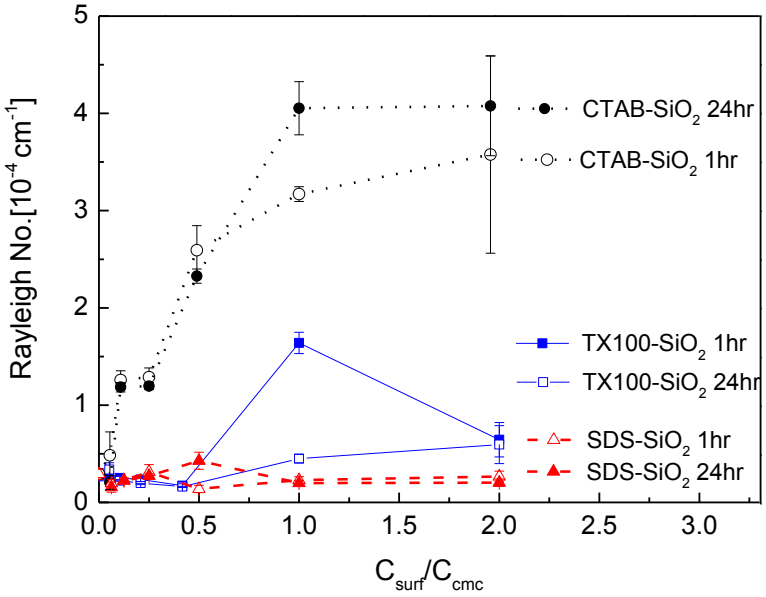

Figure 4-5: Rayleigh numbers for CTAB-silica, TX-100-silica and SDS-silica systems as a function of surfactant concentration versus CMC at pH 8. Open symbols denote measurements after 1 hour and closed symbols denote measurements after 24 hours.

Figure 4-4 shows the zeta potential measurements of the silica nanoparticles without the addition of any surfactants, as well as for silica with different concentrations of SDS, CTAB and TX100 at pH 8. To account for the artefacts due to surfactant monomers and micelles, zeta potential measurements were also conducted on surfactant solutions at CMC, and are represented as hollow symbols. Figure 4-5 shows the relative static light scattering intensities of silica nanoparticles expressed as Rayleigh number, as a function of surfactant concentration. Light scattering also reveals the time dependence of aggregation, as we observed that there was a change in relative scattering intensity if measurements were made after 1 hour (closed symbols) or after 24 hours (open symbols).

In Figure 4-4, it can be observed that the zeta potential of silica nanoparticles becomes more negatively charged in the presence of SDS compared to silica without any added SDS. These observations are rather surprising as both silica and SDS are negatively charged, hence we would not expect any interaction between SDS and silica [32]. Nonetheless, our observations indicated that SDS could be adsorbed in small amounts on the silica surface, despite being negatively charged. Ahualli et al [35] also reported a similar observation for electrophoretic mobility measurements of silica NPs in SDS solutions ranging from 0.01 mM to 8 mM SDS. They saw an increase in negative mobility and zeta potential, or super charging effect by increasing the effective charge of the silica (possible because only part of the interaction between silica and SDS is electrostatic) [35]. Another possible explanation for this observation could be due to adsorption of small amounts of SDS on heterogeneities on the

colloidal silica surface [33, 34]. We postulate that the adsorbed SDS on the silica surface may result in limited aggregation of the colloidal silica due to the 'hydrophobic interaction' between the SDS hydrocarbon tails. This can be seen in Figure 4-5, where the light scattering intensities of SDS-SiO_2 particles were slightly higher than pure SiO_2. Nonetheless, we note that the absolute difference between zeta potential for 8mM SDS and 8mM SDS-SiO_2 is not significantly large, so it is also possible that this could be due artefacts from the measurements. We note that measurements were undertaken at CMC, at which the free micelles start to form. Therefore, it is possible that only a small amount of micelles were formed in solution at that stage, and zeta potential measurements were inaccurate due to the small amounts of micelles.

However in this instance, we observed that these systems showed evidence of formation of small aggregate, which may suggest that it is possible that only part of the interaction between silica and SDS is electrostatic [35], and the hydrophobic interaction between SDS tails may be more dominant.

In the case of CTAB-silica systems, the addition of CTAB modified the silica surface (ζ) from negatively to positively charged, implying adsorption of CTAB at the silica surface. By continuously increasing CTAB concentration, it appears that the zeta potential reaches an apparent minimum at CMC and then became more positive above the CMC. Adsorption of CTAB on silica has been studied extensively using different techniques [14, 26, 27, 81] and has been well documented. These studies conclude that CTAB is adsorbed onto silica surface due to (i) surface charge neutralisation, (ii) hydrophobic effect from long hydrocarbon tail, or (iii) a combined effect of these two mechanisms [14, 50]. In this study, we could also observe that with the addition of CTAB to silica nanoparticles, light scattering intensity increased indicating formation of larger aggregates (Figure 4-5). As such we can conclude that aggregation occurs due to the adsorption of CTAB on silica surface. Furthermore, studies have shown that adsorption of CTAB on silica surface is preferential over micelle formation in bulk water [50, 51]. This may be the reason why high degree of aggregation can still be obtained at near or higher than CMC. Nevertheless, one could conclude that under the range of CTAB concentrations investigated in this study, a high degree of aggregation of 50 mg/L silica NPs was achieved.

In support of our observations, a study by Kumar and co-workers [32] showed that there is strong attractive interaction between cationic dodecyltrimethyl ammonium bromide (DTAB) and silica nanoparticles which led to the formation of aggregates. It is noted that DTAB and CTAB share a similar structure, the difference being DTAB has a shorter hydrocarbon chain length of 12 whereas CTAB. has a hydrocarbon chain length of 16. They characterised these aggregates by their fractal structure, and was found to have a fractal dimension of 2.3, consistent with an aggregate-type morphology. The concept of fractal geometry provides a

means of quantitatively describing the compactness of fractal aggregates and gives information about the internal structure. The fractal dimension of an object of mass M and radius r is defined by the relation $M \propto \rho(4/3)\pi r^{Df}$ where D_f <3 is the fractal dimension of the object [82]. Indeed the larger the value of D_f the more compact the structure of the fractal aggregates.

At the CMC of TX100 (0.24 mM), the zeta potential of pure surfactant at CMC $\zeta_{TX100,cmc}$ = -21mV. It is surprising that a negative zeta potential was observed for pure surfactant, as TX100 is a non-ionic surfactant, albeit less negatively charged than SDS at pH 8. This could be associated with the pH of the experiments, as we conducted all the experiments at pH8. In the results presented in **Figure 4-4**, the addition of TX-100 to silica suspensions at concentrations below the CMC, the zeta potential became increasingly negative. At CMC and above, this value became less negative. This was somewhat unexpected and the exact mechanism of this phenomenon could not be explained without further in depth studies. From the work of Levitz et al [40, 41], Giordano-Palmino et al [42] and Alexeev [58], it was shown that TX100 is adsorbed onto colloidal silica surface as individual molecules at low concentrations through hydrogen bonding followed by the formation of surface micelles through association at higher concentrations. This process occurs below the CMC since surface adsorbed micelles have a lower free energy than free micelles.

In general, the light scattering intensities for SDS-silica and TX100-silica were smaller than CTAB-silica. A reduced degree of scattering indicates formation of smaller aggregates, suggesting that CTAB-silica aggregates were larger in comparison to TX100-silica and SDS-silica aggregates. The presence of CTAB in silica suspensions altered the zeta potential of the aggregates to be more positive; SDS altered the zeta potential to be more negative, whilst TX100 altered the zeta potential of silica NPs both more negatively and more positively, depending on the surfactant concentration.

From this study, we could only observe general trends between the surfactant-silica interaction. Further characterization techniques, as well as zeta potential and light scattering experiments at a wider range of concentrations (c_{surf} /c_{cmc}) will be required to elucidate the interaction mechanism between silica and surfactants.

4.3 Filtration Experiments - Flux-Step Method

4.3.1 Fouling Development and Critical Flux

In this section, the fouling strength of the colloidal feed water is discussed in terms of the fouling rate as the membrane resistance per unit time.

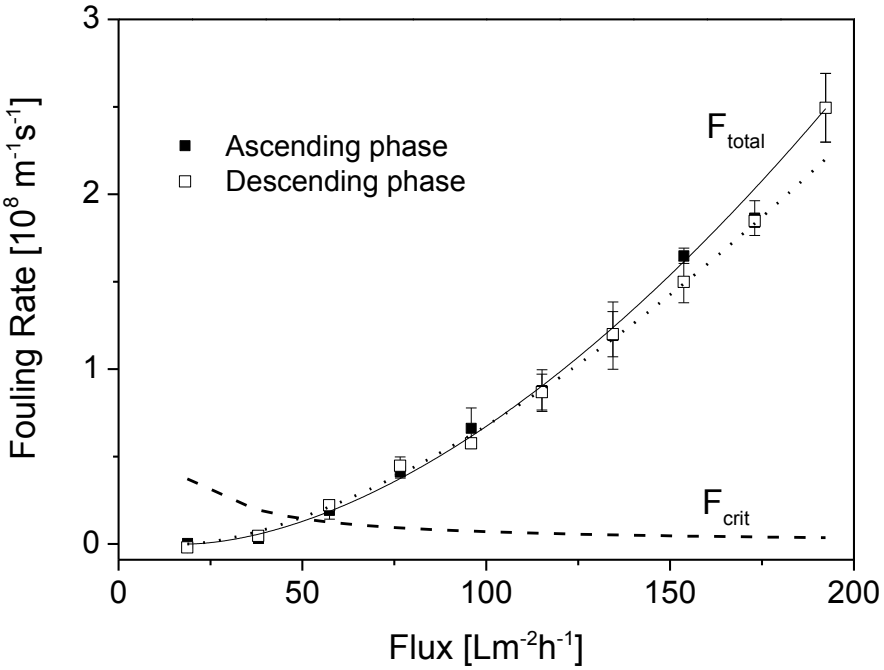

Figure 4-6: Total fouling rate and critical fouling rate for a filtration of 50 mg/L Ludox TM-50 SiO_2 at pH 8. Open symbols and closed symbols denote fouling rates in ascending phase and descending phase, respectively.

In Figure 4-6, fouling rates in the ascending phase are denoted by the closed symbols and connected with by a solid line, whereas the descending phase have open symbols and are connected by a dotted line for clarity. The critical flux for 50 mg/L silica suspension at pH 8 in the absence of added surfactants was determined to be 52 $Lm^{-2}h^{-1}$. It can be inferred that there is ample effect of fouling history by comparing the total fouling rate in the ascending phase and the descending phase. These two fouling rates almost completely overlapped each other revealing a very small hysteresis [64].

Analysis of the critical flux for filtration of CTAB-SiO_2, SDS-SiO_2 and TX100-SiO_2 systems at various concentrations is shown in Table 4. The fouling development of each of the surfactant-silica system will be discussed in further detail in sections below.

In general, the critical flux for SDS-silica systems were lower than for pure silica systems. It was also observed that as concentration of SDS increased, the critical flux was also reached earlier. In the case of filtration of SDS solution and SDS-SiO_2 system at CMC (8 mM), critical flux was immediately reached during the first ascending step and could not be quantified experimentally. The significance of having a lower critical flux is that fouling will occur at a lower flux and therefore would require more membrane area to treat the same amount of feed flowrate compared to systems with a higher critical flux, before fouling occurs. As such, it can

be considered as undesirable to have lower critical fluxes in terms of productivity and operating cost.

Table 4: Critical flux for SDS-SiO_2, CTAB-SiO_2 and TX100- SiO_2 systems at pH 8 & 30°C.

Silica-Surfactant Solutions	Surfactant Concentration		Silica Concentration	Critical Flux, J_{crit} [$Lm^{-2}h^{-1}$]	
	mM	c_{surf} /c_{CMC}	mg/L	Ascending Phase	Descending Phase
SiO_2	--	--	50	52	49
SDS- SiO_2	1	0.125	50	44	45
	4	0.5	50	31	28
	8	1	50	Immediate[1]	Immediate[1]
	8	1	--	Immediate[1]	Immediate[1]
CTAB- SiO_2	0.115	0.125	50	77	64
	0.46	0.5	50	31	30
	0.92	1	50	Immediate[1]	Immediate[1]
	0.92	1	--	Immediate[1]	Immediate[1]
TX100-SiO_2	0.025	0.125	50	61	55
	0.1	0.5	50	45	48
	0.24	1	50	38	37
	0.24	1	--	35	29

[1] Fouling rate for the first flux step exceeded critical fouling rate F_{crit} , as such the critical flux could not be determined experimentally.

For the 0.115 mM (0.125 CMC) CTAB-silica system, we observed a higher critical flux compared to critical flux of 50 mg/L silica suspension, at 76 $Lm^{-2}h^{-1}$ and 52 $Lm^{-2}h^{-1}$, respectively. This could be seen as an improvement to the productivity and operational parameters of the membrane system On the other hand, when 0.46 mM (0.5 CMC) CTAB was added to the silica suspension, the critical flux became lower (at 38 $Lm^{-2}h^{-1}$) than for reference solution without surfactants. Filtration of 0.92 mM (CMC) CTAB and 0.92 mM (CMC) CTAB-SiO_2 resulted in the critical flux being reached during the first ascending step and could not be quantified experimentally.

In the case of TX100, we observed that the critical flux for 0.025 mM (0.125 CMC) TX100-SiO_2 system was slightly higher compared to critical flux of 50 mg/L silica suspension. However the critical flux was reached earlier during the filtration of suspensions with higher TX100 concentrations, whereby the highest decrease in critical flux occurred for the 0.24 mM (CMC) TX100 systems.

4.4 Influence of Surfactants on Fouling Rate

4.4.1 Influence of SDS on Colloidal Fouling Rate

The effect of SDS on colloidal fouling rate during membrane filtration was investigated at pH 8. The concentration of SDS in the feed solution was varied from 1 mM (0.125 CMC) to 8 mM (CMC) and the evolution of fouling potential as a function of flux is shown in Figure 4-7(a). To clearly show the evolution of fouling rate at lower fluxes, an expanded section of the graph is depicted in Figure 4-7(b).

It was observed that the addition of SDS at 1 mM (0.125 CMC), 4 mM (0.5 CMC) and 8 mM (CMC) to colloidal SiO_2 suspensions resulted in a higher fouling rate compared to the filtration without any SDS. At the same time, we observed that zeta potential of the silica particles was found to be more negative with the addition of SDS, which may suggest SDS is slightly adsorbed onto silica particles by masking of heterogeneities on the silica surface [34]. Static light scattering studies of SDS-SiO_2 suspensions indicated that the static scattering intensity was low, suggesting aggregation of silica NPs occurred to a small extent, or the presence of small aggregates in the suspension.

In SDS-SiO_2 filtration systems, we could postulate that there are a number of fouling mechanisms that are occurring simultaneously; namely (i) the interaction between surfactant monomers with PVP, resulting in the formation of micelle-like aggregates on the membrane surface by association [83] (ii) attachment of SDS monomers on membrane surface due to hydrophobic interaction between hydrophobic tails of SDS and hydrophobic groups on the membrane surface [84, 85], and (iii) formation of a fouling cake layer during filtration.

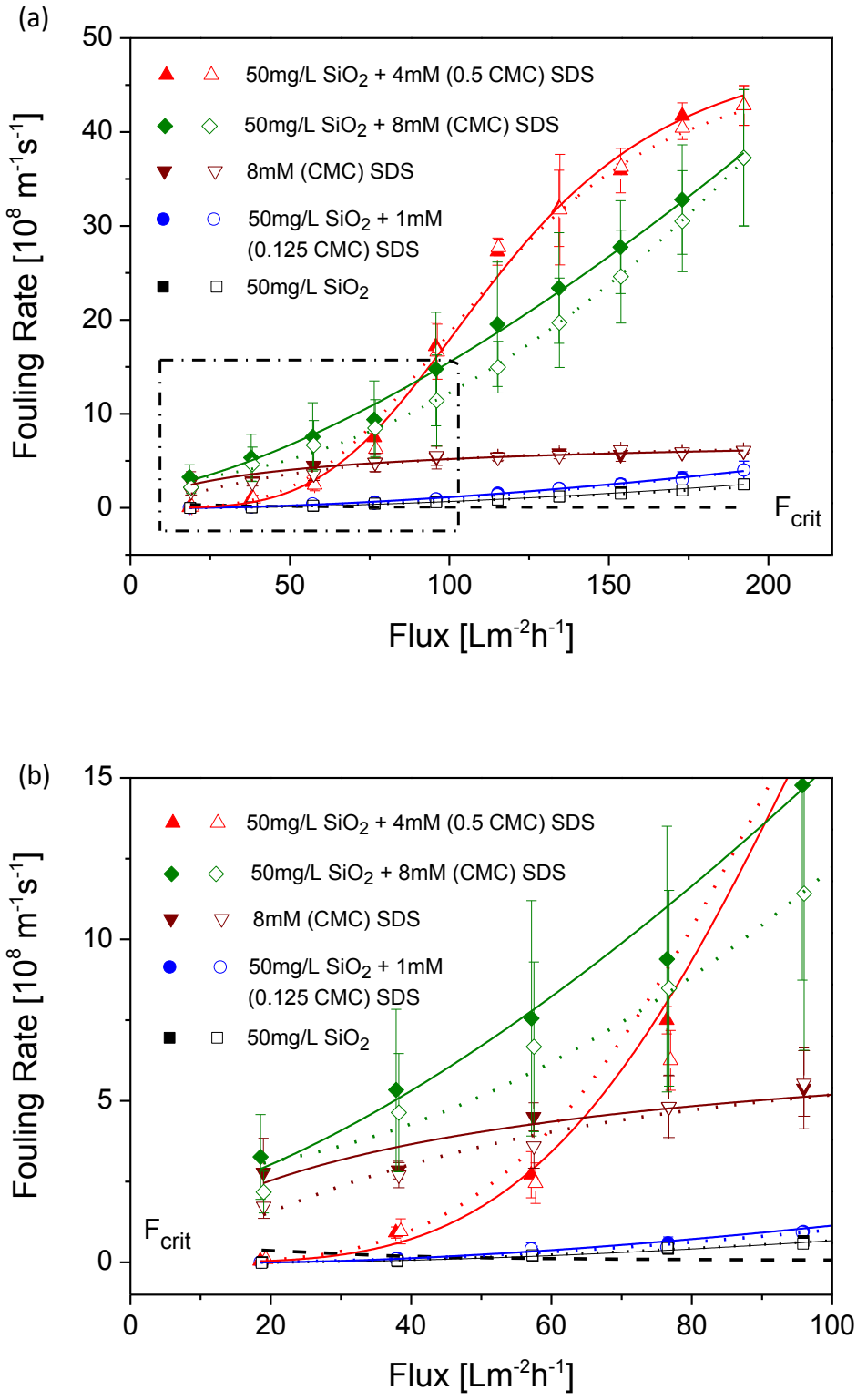

Figure 4-7: Profile of fouling rates for SDS-SiO_2 systems at various surfactant concentrations at pH 8 and 30°C. Open symbols and closed symbols denote fouling rates in ascending phase and descending phase, respectively.

SDS interacts strongly with neutral polymer such as PVP [83, 86, 87]. The SDS-PVP interaction has been extensively studied by various techniques such as surface tension [83], calorimetry [88], potentiometric measurements [89], light scattering [83, 86, 87]. Polarizable pyrrolidone side groups in the PVP can acquire positive charge in the nitrogen ring, at which an anionic group such as SDS can interact [87]. Due to this interaction, aggregation of SDS can occur at a much lower concentration than its aqueous CMC. The concentration at which aggregation occurs due to association is known as the critical association concentration (CAC). The CAC of SDS in the presence of PVP is independent of the concentration of PVP in the solution and is reported to be between 1.4 and 2.1 mM [83], which is considerable lower than the CMC of 8 mM of pure surfactant.

Moreover, SDS monomers, having sizes much smaller than membrane pore size, are able to enter the pores and be adsorbed onto the walls due to hydrophobic interaction with hydrophobic groups on the membrane (e.g. PES) [84]. This may result in constriction of the pore [73, 84, 90], as a consequence fouling will occur. Adsorption of surfactant inside membrane pores generally causes irreversible fouling [91].

Another fouling mechanism that may occur is the formation of a cake layer on the membrane surface. It is noted that the average pore size of the membrane was 24 nm and the average size of SiO_2 particles as reported by the manufacturer was 22 nm [92]. Given such similar sizes particle and pore sizes, silica nanoparticles are not able to penetrate through the membrane pores. They may therefore be retained on the surface during filtration and may cause complete pore blocking. Over time, a cake layer could be formed on the membrane surface during filtration. However it is noted that the inner surface of the membrane is negatively charged. Surfactant monomers and micelles are also negatively charged. Therefore, in principle, there should also be an electrostatic repelling force between the surfactant monomers and micelles from the membrane surface.

For the 1mM SDS-SiO_2 system, we observed that the total fouling rate was only slightly higher in comparison to the SiO_2 system. Previous studies have shown that the addition of low concentrations of SDS up to 0.3 mM [52] showed a reduction in the fouling potential of SDS-SiO_2 systems, which they attributed to the masking effect of heterogeneities, resulting in a more uniform and more negatively charged SiO_2 particle. Singh and Song [52] postulated that a more loosely packed cake layer on their UF membrane was formed, hence lower fouling potential. Unfortunately, we were not able to observe this, as the lowest amount of SDS added was 1mM, which was already higher than the experimental conditions at which this phenomenon was observed by Singh and Song [52].

In the 8 mM SDS-SiO_2 system, (i.e. at the CMC) the fouling rate was already much higher than at 1 mM (0.125 CMC) SDS-SiO_2 and 4 mM (0.5 CMC) SDS-SiO_2 at the onset of

experiment, which was expected. As the flux increased, we observed an exponential increase in total fouling rate. If we consider that SDS is adsorbed onto silica surfaces due to heterogeneities at low concentrations, it is likely that SDS will not be adsorbed on SiO_2 surface anymore after the masking effect at low concentration. However, SDS can also dissociate in aqueous solution and can therefore act a salt. Hence the ionic strength of the suspension would be increased [85]. This may result in the compression of the electrical double layer around the colloids, causing destabilisation and subsequently higher fouling rates [52, 85]. We can also postulate that the SDS concentration at the vicinity of the membrane surface is at least equal or higher than the bulk concentration due to concentration polarization. Hence, the local concentration of SDS at the membrane surface could very well exceed the CMC of SDS. If the concentration at the membrane surface is higher than CMC, a larger number of negatively charged micelles could be formed. These micelles may co-deposit in the cake layer of SDS-SiO_2 forming a thicker cake layer, resulting in higher fouling rate. We postulate that the compression of this micellar-silica nanoparticle cake layer may cause it to overcome the electrostatic repulsion between the micelles and may become like a continuous gel layer. Furthermore, in our investigations, PVP is present on the membrane surface as it is used as an additive during the manufacture of the membrane. Studies have shown that, even at low concentrations of PVP, there is evidence of association of SDS and PVP below its CAC [86, 87]. As such, we cannot exclude the interaction between SDS monomers and micelles with PVP molecules on the membrane surface. These are some of the possible explanations as to why we observe exponential increase in fouling rates as the flux is increased.

However, for the 4 mM (0.5 CMC) SDS-SiO_2 system, we observed an unexpected trend in the total fouling rate profile. Upon addition of 4 mM (0.5 CMC) SDS up to fluxes of about 80 LMH, we observed an exponential increase of fouling rate with flux, where they lie in between the fouling rates of 1 mM (0.125 CMC) SDS-SiO_2 and 8 mM (CMC) SDS-SiO_2 systems. In any case, this profile was as expected. This behaviour was observed at lower range of fluxes up to approximately 80LMH. However, at higher fluxes (80 LMH and above), the trend deviated from the expected, as fouling rate increased in a more pronounced exponential manner, eventually surpassing the fouling rate of 8mM (CMC) SDS-SiO_2 at the same fluxes. This suggests that there are some other fouling mechanisms that are in play.

This behaviour may be explained by the following speculation: in the 4 mM (0.5 CMC) SDS-SiO_2 suspension, free micelles are not expected to be formed in the bulk solution, however surface micelles could be formed on the membrane surface via association with PVP molecules. As previously discussed, we can also consider that the concentration of SDS near the membrane surface could be higher than the bulk concentration due to concentration polarization. However, in the case for 4 mM (0.5 CMC) SDS-SiO_2, it is possible that a smaller amount of micelles are formed in the lower fluxes because concentration polarization effect is

too low. When flux was increased, concentration polarization was enhanced, and in both 4 mM and 8 mM SDS-SiO_2 cases, micelles and a gel-like cake layer was formed. However, since there is less SDS in the 4 mM solution, the repulsive interactions are weaker and the fouling cake layer is denser, resulting in a higher fouling rate. Whereas, in the 8 mM (CMC) SDS-SiO_2 system, the micelles co-deposited in the cake layer have a highly negatively charged exterior and this would result in depletion and stronger structural repulsion between the colloidal particles [52] resulting in a more open structured cake layer.

To further understand the effect of surfactant-membrane interaction and flux dependence on the fouling potential at CMC, filtration experiments were conducted with 8 mM SDS only solutions. We observed that the fouling rate for the 8 mM SDS solution and 8 mM SDS-SiO_2 suspension were comparable at low fluxes (Figure 4-7). This suggests that surfactant-membrane interaction dominates at lower fluxes. As flux increases, we saw that the fouling rate for 8 mM SDS system reached a plateau at approximately $5x10^8$ $m^{-1}s^{-1}$ while 8 mM SDS-SiO_2 systems increased exponentially. Here we can attribute this to the effect of fouling due to SDS-SiO_2 aggregates on the membrane surface. Furthermore we hypothesize that at higher fluxes, the physical compression of SDS-SiO_2 aggregates at the membrane interface may cause a collapse of the micelles or is sufficiently high enough to overcome the electrical double layer, resulting in a more closely packed and/or continuous fouling layer. With regards to the plateau observed for the filtration of 8 mM SDS, it may be due to the collapse of micelles at higher fluxes.

4.4.2 Influence of CTAB on Colloidal Fouling Rate

The effect of CTAB on colloidal fouling potential during membrane filtration was investigated at pH 8. The feed concentration of CTAB was varied between 0.115 mM (0.125 CMC) to 0.92 mM (CMC) and the evolution of the fouling potential as a function of flux is shown in Figure 4-8(a). An expanded section of fouling rate profile at lower fluxes is shown in Figure 4-8(b).

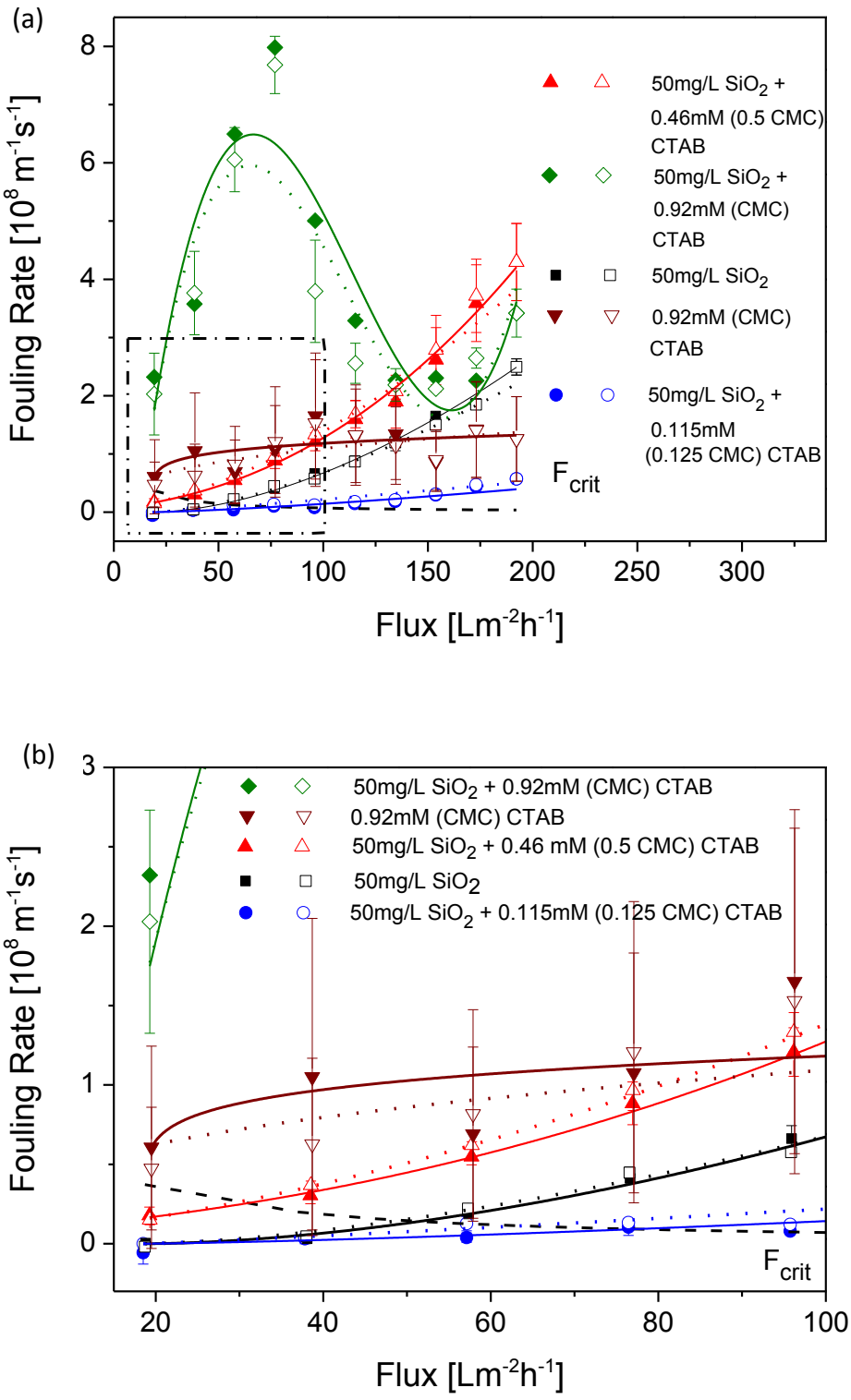

Figure 4-8: Profile of fouling rates for CTAB-SiO_2 systems at various surfactant concentrations at pH 8 and 30°C. Open symbols and closed symbols denote fouling rates in ascending phase and descending phase, respectively.

From Figure 4-8(a), we observed that the addition of CTAB in 50 mg/L silica suspensions reduced the fouling rate at low concentration (0.115 mM) but the fouling rate was increased with higher CTAB concentrations of 0.46 mM (0.5 CMC) and 0.92 mM.(CMC)

Similar to fouling mechanisms in SDS-SiO_2 filtration systems, we could also postulate that there are a number of fouling mechanisms that are occurring in CTAB-SiO_2 filtration systems. CTAB monomers, which are comprised of a positively charged head and a hydrophobic tail, may penetrate into the membrane pores and interact with the membrane surface in the following manner: (i) the positively charged head of CTAB may be attracted to the negatively charged membrane, and (ii) hydrophobic interaction between hydrophobic tails and hydrophobic groups on the membrane. The adsorption of surfactants on the walls of the membrane may result in constriction of the pore and/or pore blocking [73, 83, 84, 90], which may also contribute to irreversible fouling [91].

Similarly, the formation of fouling cake layer on the membrane surface may also occur during filtration for the reason that the average size of nanoparticles are similar to the average membrane pore size. Furthermore, we have shown evidence of colloidal aggregation due to CTAB addition, which meant that the average size of aggregates was even bigger than without surfactants. However, we hypothesize that the cake layer formed may be more porous than the cake layer formed in SDS-SiO_2 systems as silica nanoparticles formed larger aggregates in the presence of CTAB already in the bulk solution. Indeed, static light scattering intensity measurements indicate that larger aggregates were formed when CTAB was added (Figure 4-5). This was also observed visually. As silica nanoparticles were injected into the CTAB solution, white, opaque clusters of aggregates were formed immediately.

When 0.115 mM (0.125 CMC) CTAB was added to the SiO_2 suspension, we observed a marked improvement in fouling rate compared to pure SiO_2 suspensions. This drop in fouling potential could be interpreted as the effect of adsorption of CTAB on silica surface resulting in aggregation of colloidal silica due to the hydrophobic interaction of CTAB tails. As a consequence, a more porous fouling cake layer of on the membrane may be deposited on the membrane surface. It can be seen that, although the charge of CTAB monomers are positive and the surface potential of the membrane was negative, we still observed a drop in fouling potential compared to pure SiO_2 suspensions. This indicates that the electrostatic attraction between CTAB monomers and membrane surface may not be dominant and we postulate that the effect of having a more loosely packed cake layer may be the dominant effect. A study by Kumar et al [32] revealed that there is a strong attractive interaction of silica nanoparticles with cationic dodecyltrimethyl ammonium bromide (DTAB) micelles which led to the formation of aggregates. These aggregates were characterised by a fractal structure and was found to have a fractal dimension, D_f of 2.3, consistent with an aggregate-type

morphology. It is noted that a D_f of 2.3 is considered a compact structure, and bearing in mind that CTAB has a similar structure and charge properties to DTAB, this lends to the hypothesis that a CTAB-silica aggregates could form a more open cake structures.

In the case where the concentration of CTAB was increased to 0.46 mM (0.5 CMC), the total fouling rate was higher compared to fouling rates in both the pure 50 mg/L SiO_2 and 0.115 mM (0.125 CMC) CTAB-SiO_2 systems (Figure 4-8) at the same fluxes. Light scattering intensity measurements suggest that silica aggregates were larger in 0.46 mM (0.5 CMC) CTAB than 0.115 mM (0.125 CMC) CTAB solutions, and as such we may expect a more porous cake layer, thus lower fouling rate. However the opposite trend was observed. A plausible explanation could be that at the higher concentration of 0.46 mM, there were more CTAB monomers in the bulk solution to interact with the membrane surface. As such, a more close-packed layer of surfactant on the membrane surface may be formed [84]. A higher fouling rate suggests that surfactant-membrane surface interaction may be more dominant than the effect of having a loosely packed cake layer on the membrane surface. Furthermore at the membrane-feed solution interface, the local concentration of CTAB is expected to be higher compared to the concentration in the bulk due to concentration polarization, and as such the formation of micelles near the membrane surface could not be excluded.

Upon addition of 0.92mM CTAB to a silica suspension (i.e. at the CMC of CTAB), a very different fouling rate profile as a function of flux was observed. Instead of attaining the maximum fouling rate at the highest flux as expected, the maximum fouling rate in filtration of 0.92 mM CTAB-SiO_2 was observed at a much lower flux at about 77 $Lm^{-2}h^{-1}$. Above this flux, the fouling rate appeared to decrease to a pseudo-minimum at approximately 160 $Lm^{-2}h^{-1}$. Following that, the fouling rate increased again with flux.

At the onset of filtration of 0.92 mM CTAB-SiO_2 suspensions, the fouling rate already showed an exponential increase at the lower range of fluxes of up to 77 $Lm^{-2}h^{-1}$. We may consider this observation to be the combined effect of a few fouling mechanisms; that is (i) highly positively charged micelles may be attracted to the negatively charged membrane surface, as well as the adsorption of CTAB monomers on the membrane surface, resulting in the constriction of the membrane pores; (ii) formation of a fouling cake layer on the membrane surface. All of these fouling mechanisms would indeed contribute to the increase in fouling rate.

However when fluxes were increased further and we observed a decline in the fouling rate. As explanation we postulate the following; CTAB micelles could also be formed within the cake layer of silica nanoparticles. These micelles would have a highly positively charged and may be more strongly repulsed by the CTAB-SiO_2 aggregates. Consequently a more loosely packed cake layer could form instead [52]. Furthermore, it has been reported that CTAB could form ‘tail-to-tail’ or bilayers on silica surface [44, 50] and may restabilise the silica

suspension [44]. This could explain why we observed a decline in fouling rate at higher fluxes. However, in depth studies, preferably at the membrane interface are required to elucidate this fouling behaviour. To further investigate the effect of aggregates on membrane fouling, filtration of 0.92mM CTAB solution without silica nanoparticles was performed. It was interesting to note that the evolution of fouling rate was similar to the one observed for filtration of 8mM SDS. That is, a relatively high fouling rate was observed at the onset of experiment, quickly followed by a plateau at higher fluxes. Again, we attributed this to the collapse of micelles due to the higher fluxes.

4.4.3 Influence of TX100 on Colloidal Fouling Rate

In this section, the effect of non-ionic surfactant, TX100 on colloidal fouling potential during membrane filtration was investigated at pH 8. The feed concentration of TX100 was varied between 0.025 mM (0.125 CMC) to 0.24 mM (CMC) and the evolution of the fouling potential as a function of flux is shown in Figure 4-9(a) .An expanded section of fouling rate profile at lower fluxes is shown in Figure 4-9(b).

It was observed that the addition of 0.025 mM (0.125 CMC) TX100 to the SiO_2 colloidal suspension resulted in only a slight, if not negligible reduction in the fouling potential when compared to filtration of pure SiO_2 suspension. We can postulate that the dominant fouling mechanism in this instance is attributed to the formation of cake layer for the following reasons; (i) average size of SiO_2 nanoparticles is approximately the average pore size, (ii) static light scattering measurements indicated that only small aggregates were formed (Figure 4-5), and (iii) the zeta potential of the pure silica nanoparticles was comparable to the zeta potential of 0.025 mM TX100-SiO_2 aggregates (Figure 4-4).

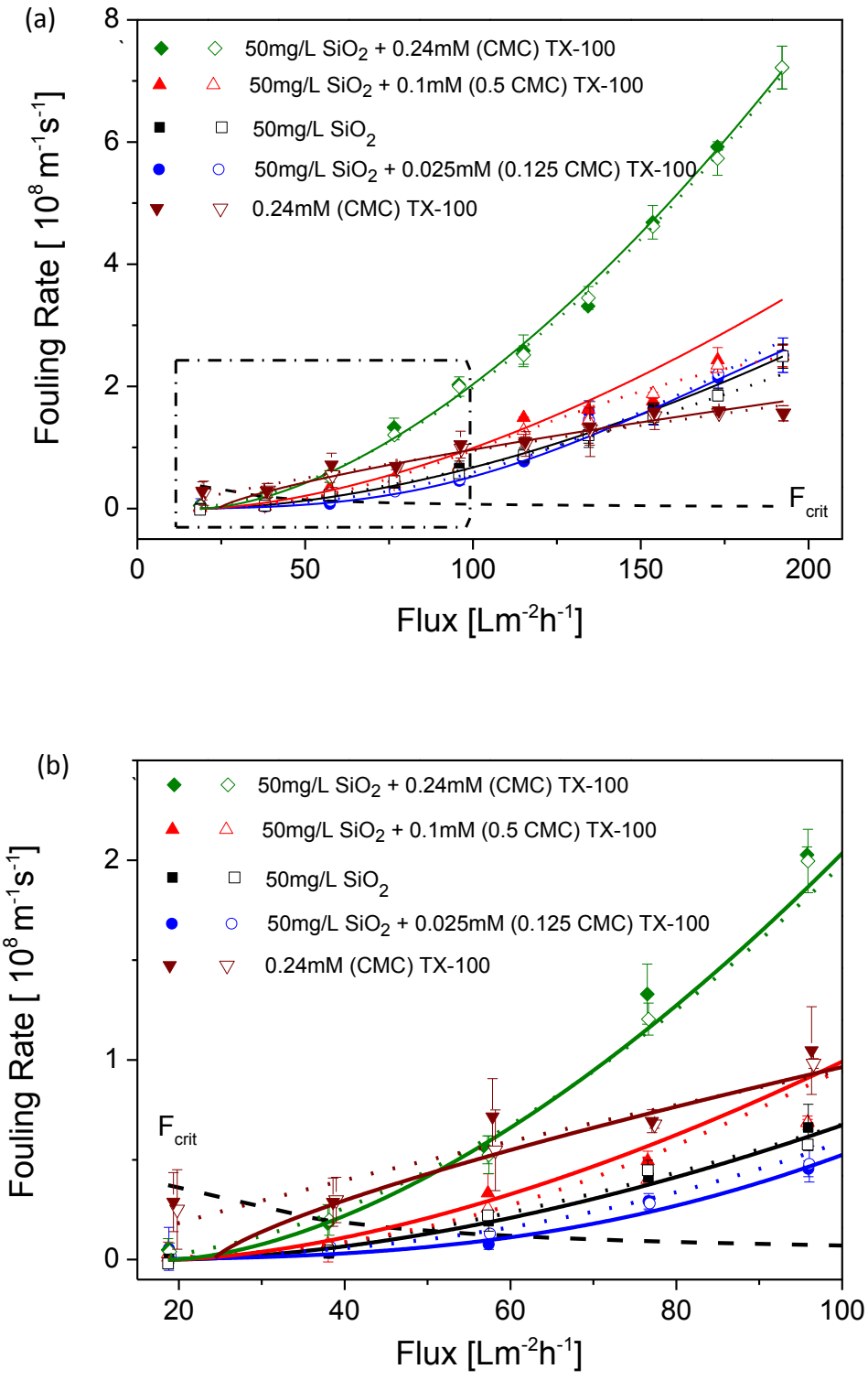

Figure 4-9: Profile of fouling rates for TX100-SiO_2 systems at various surfactant concentrations at pH 8 and 30°C. Open symbols and closed symbols denote fouling rates in ascending phase and descending phase, respectively.

When the concentration of TX100 in the feed solution was increased to 0.1 mM (0.5 CMC) and 0.24mM (CMC), we observed that the fouling rate increased more steeply with increasing concentration and flux, as expected. In these instances, other fouling mechanisms may have an influence on the fouling rate. Similar to ionic surfactants, the hydrophobic tail of the TX100 monomers can interact with hydrophobic groups on the membrane surface [84, 90]. These monomers can penetrate the membrane pores and be adsorbed on the membrane surface, thus constricting the pore, resulting in a higher fouling rate. TX100 monomers can also interact with PVP molecules on the membrane surface [93], whereby micelles could be formed by association at the membrane surface. The CAC for TX100 has been reported to be about 0.6 times the CMC of TX100 [93]. This indicates that the TX100-PVP interaction is less strong compared to the interaction between SDS-PVP given that the CAC of SDS-PVP is approximate 0.25 times of CMC. In addition, we observed that the fouling rate for all TX100-SiO_2 systems at the onset of the filtration experiments were very similar except for the filtration of TX100 only at CMC. This may also indicate that the interaction between TX-100–PVP on the membrane surface is not as extensive as the degree of SDS-PVP interaction.

The increase in fouling rate could also be attributed to the formation of a cake layer on the surface of the membrane.

An overall comparison of total fouling rates for surfactant-silica systems indicated that SDS-silica systems showed fouling rates of an order of magnitude higher than those of CTAB-silica and TX100-silica systems at the same c_{surf}/c_{CMC} ratio. Based on the static light scattering and zeta potential results of the silica-surfactant systems obtained in this study, we found this result unexpected, as one would expect the CTAB-SiO_2 systems to exhibit higher fouling rates compared to SDS-silica and TX100-silica systems. Nevertheless, there are several fouling mechanisms that are occurring simultaneously in these silica-surfactant filtration systems, which make it challenging to understand and explain the extent of the different mechanisms that are occurring. However, we may attribute this difference in overall fouling rate to the following mechanisms: (i) the strong interaction between SDS and PVP on the membrane surface, which promoted the formation of aggregates via association at the membrane surface, (ii) the effect of fractal structure of the aggregates of CTAB-silica systems, whereby the aggregates formed were irregular and therefore a more open cake structure could be formed in the fouling layer. In the case of SDS-silica, the aggregates formed were smaller in comparison and as such the packing density of the aggregates was higher.

4.5 Influence of Surfactant on Membrane Separation Properties

4.5.1 Influence of Surfactants on Silica Rejection

The influence of the SDS, CTAB and TX100 at various concentrations on silica nanoparticle rejection as a function of flux was investigated and shown in Figure 4-10, Figure 4-11 and Figure 4-12, respectively. The silica rejection in the ascending phase is depicted with closed symbols while the rejection in the descending phase has open symbols.

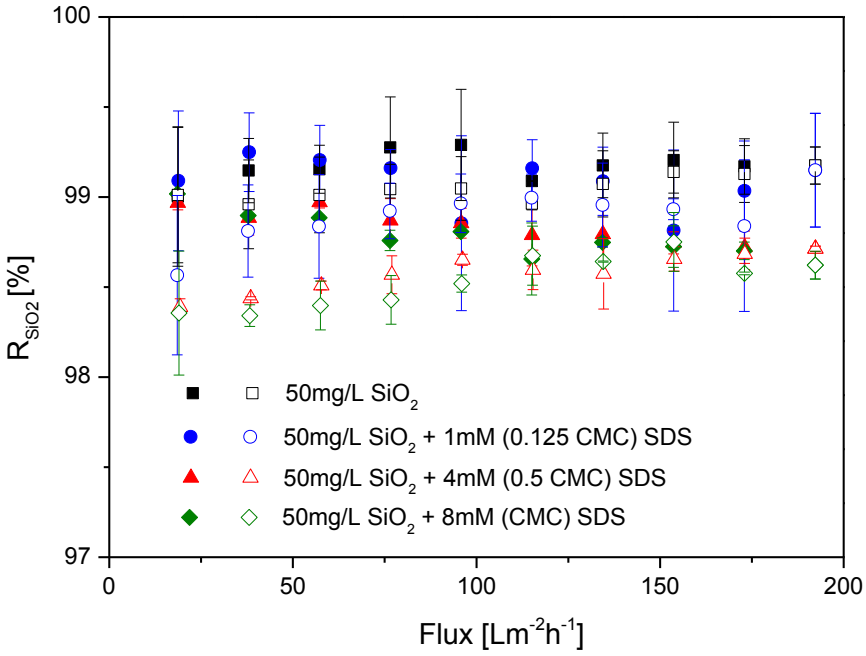

Figure 4-10: Silica rejection for filtration of SDS-SiO_2 systems at pH 8 and 30 °C (CMC SDS: 8 mM). Open symbols and closed symbols denote fouling rates in ascending phase and descending phase, respectively.

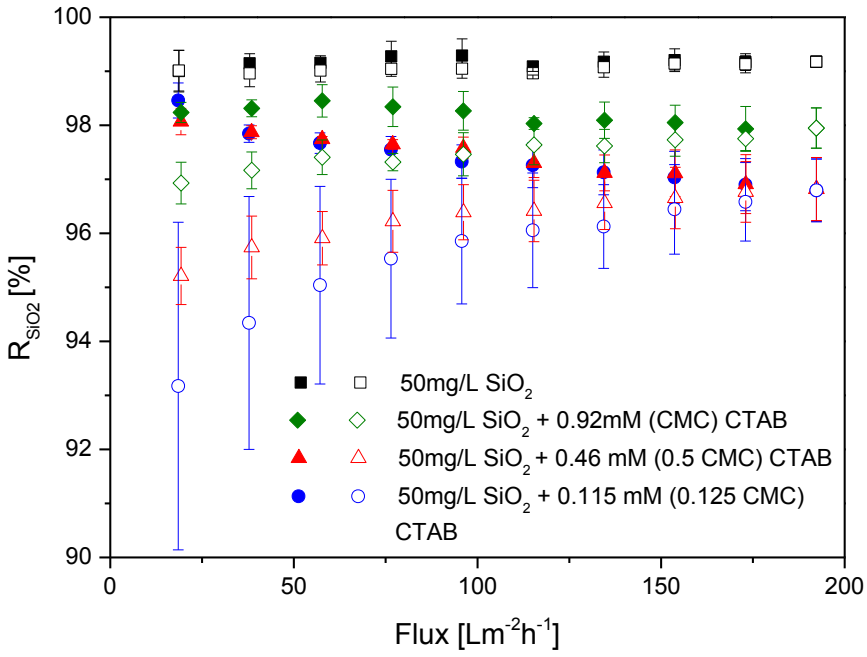

Figure 4-11: Silica rejection for filtration of CTAB-SiO_2 systems at pH 8 and 30 °C (CMC CTAB: 0.92 mM). Open symbols and closed symbols denote fouling rates in ascending phase and descending phase, respectively.

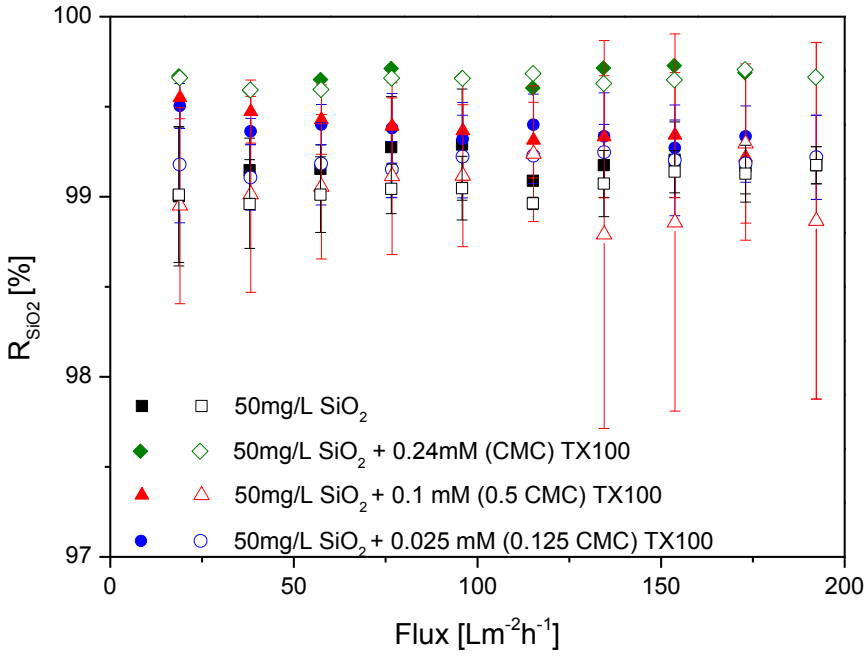

Figure 4-12: Silica rejection for filtration of TX100-SiO_2 systems at pH 8 and 30°C. (CMC TX100: 0.24 mM). Open symbols and closed symbols denote fouling rates in ascending phase and descending phase, respectively.

In general, the rejection of silica nanoparticles for all the systems investigated was high; in the range of 90% and above. Such a high rejection rate was expected as (i) the average pore size is approximately the average size of the silica nanoparticle which implies that silica nanoparticles are retained on the surface of the membrane, (ii) we expect the formation of a cake layer of silica particles on the surface of the membrane, resulting in an additional barrier for silica nanoparticles. Indeed, SEM images of membranes taken after a backwashing at the end of the filtration experiment in Figure 4-13, clearly shows the presence of a layer of silica nanoparticles deposited on the membrane surface. This layer of nanoparticles was observed for all surfactant-silica systems after the backwash step, which was part of the filtration experiment. As such, we can conclude that the backwash was insufficient to remove this fouling layer.

SDS-SiO_2 and TX100-SiO_2 systems showed very similar silica rejection between 98 to 99.5%, however CTAB-SiO_2 systems showed slightly lower rejection of down to 93%. Nevertheless, it is noted that this difference is within the experimental error, as such no conclusive trends or fouling mechanism other than cake filtration could be deduced from this data.

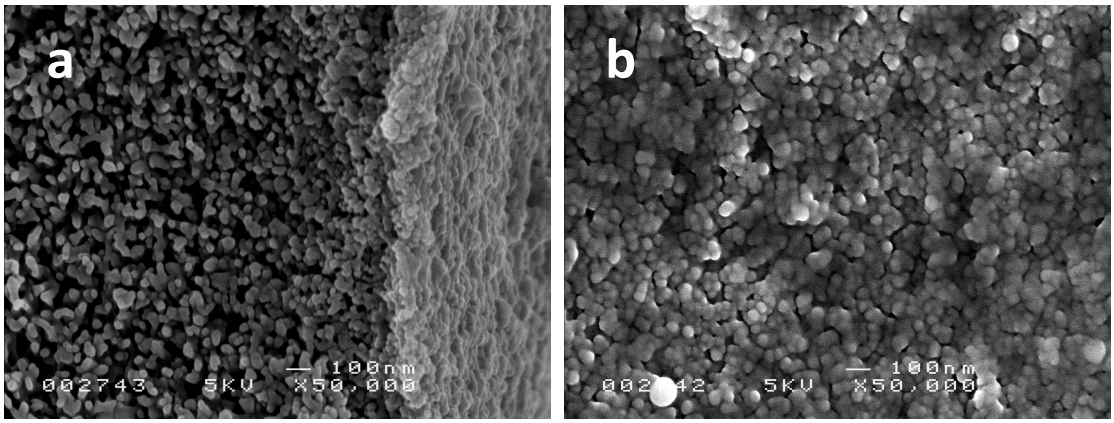

Figure 4-13: SEM images- (a) cross-section and (b) surface images of UF PES-PVP membrane after filtration of SDS-silica solution, and was observed for all membranes after filtration.

4.5.2 Influence of Concentration on Surfactant Rejection

The influence of the SDS, CTAB and TX100 concentration on surfactant rejection as a function of flux was investigated and the graphs can be found in Appendix B.

In most cases, we could observe rejection of surfactant, however for some cases, we also observed negative rejection of surfactants, particularly for the first few flux steps in the ascending phase. Noting that the size of monomers and micelles are significantly smaller than the average membrane pore size, we could attribute the rejection of surfactants to several mechanisms. Surfactants could be rejected due to adsorption to the silica

nanoparticles, electrostatic interaction with the membrane surface, as well as electrostatic interaction with the fouling layer formed on the membrane surface. With regards to negative rejection, we could not explicitly explain the reason for this observation, however we could attribute this to leaching of surfactants that were adsorbed in the membrane during filtration in the previous step, since we have established that the backwashing step was unable to remove the fouling layer. Furthermore, it was also possible that the glycerol-purging step was insufficient to remove glycerol from the membranes, as such glycerol was leached into the permeate. Other possible reasons could also include contamination from the equipment itself, e.g. tubing. Another observation on the surfactant rejection in this investigation was that there was no observable flux dependency on the rejection.

It was also noted that for TOC analysis, we were unable to undertake these measurements ourselves in-house and we relied on an external partner (water supply company, Vitens NV) to conduct TOC analysis. As such there was a lag-time of a few days up to a few weeks before analysis could be performed, which could have resulted in contamination due to bacterial growth, deterioration of samples etc. Overall, the data obtained from TOC analysis were considered not reliable. As such, there is the need to repeat these measurements under the same experimental conditions and to also ensure that the time between sample collection and analysis should be as short as possible, if not directly after experiments.

4.6 Influence of Surfactant on Pure Water Permeability

As described in the methodology, pure water permeability check was undertaken after the backwash of the membrane module; the purpose of this was to ascertain the effect of surfactants and extent of irreversible fouling on the membrane. The extent of irreversible fouling could then be characterised qualitatively by the *permeability recovery (PR),* which is defined as the ratio of pure water permeability of the membrane after backwash to the pure water permeability of the clean membrane. In theory, if irreversible fouling occurs, we would expect to see a PR of <1. With this in mind we will discuss the effect of SDS, CTAB and TX100 on this parameter.

4.6.1 Influence of SDS on Permeability Recovery of UF Membranes

The effect of SDS on membrane permeability recovery (PR) as a function of flux is shown in Figure 4-14. PR in the ascending phase is represented by closed symbols and connected by a solid line, while PR in the descending phase is shown by open symbols and are connected by a dashed line. In principle, it is noted that the initial PR of all the systems should be 1.

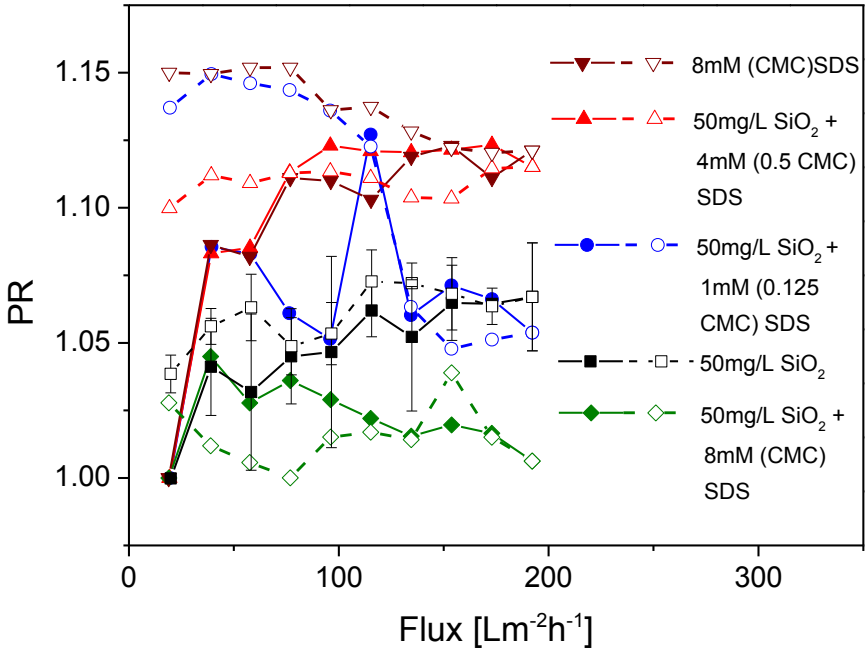

Figure 4-14: Permeability recovery (PR) for SDS-SiO_2 systems at various surfactant concentrations. Open symbols and closed symbols denote fouling rates in ascending phase and descending phase, respectively.

The PR of membrane modules used in the filtration of 50 mg/L SiO_2 suspension ranged from 1.00 to 1.07. Blank filtration experiments conducted with Milli-Q water showed that the pure water permeability of clean modules fluctuated within 10%. As such, in the case of PR of 50 mg/L SiO_2 suspension, we can consider that no detectable irreversible fouling was observed. However, it was also unexpected that when 1 mM (0.125 CMC) SDS or 8 mM (CMC) SDS was added to the SiO_2 suspension, the PR of the membranes were also within the 'no detectable irreversible fouling' range. It is likely that the sensitivity of PR was insufficient to detect the extent of irreversible fouling here. On the contrary, the 4 mM (0.5 CMC) SDS-SiO_2 and 8mM SDS systems showed an appreciable increase in PR, and while we could not observe any distinct relationship between SDS concentration and PR, it was interesting to note that filtration of the 8 mM SDS only solution resulted in the biggest increase in PR of about 15%.

Differences in pure water permeability can be caused by several reasons: Firstly we have established earlier that SDS monomers and micelles are able to interact with PVP on the membrane surface. Given that the size of SDS micelles are the range of 5 nm [94], and the average membrane pore size is 24 nm, we can postulate that surfactant monomers and micelles can penetrate the membrane pores and interact with both PES and PVP on the membrane surface. Water flux is related to hydophilicity or wettability [95]. It is hypothesized that an improved wetting of the membrane surface can cause this increase after hydrophobic

adsorption between non-polar tails of SDS and the membrane. Singh and Song [28] reported contact angle measurements of flat sheet polysulfone membranes, which show that membrane became more hydrophilic after filtration with increasing SDS concentration of SDS. SEM images of membranes after filtration experiment, as shown in Figure 4-13 also show that there was still a layer of silica nanoparticles on the membrane surface, indicating that the backwash step was insufficient. In addition, we cannot discount the effect of adsorption kinetics, as we could observe distinct differences in PR, for instance when 4mM or 8mM SDS was added to SiO_2 suspensions.

4.6.2 Influence of CTAB on Permeability Recovery of UF Membranes

The effect of CTAB on membrane permeability recovery (PR) as a function of flux is illustrated in Figure 4-15. PR in the ascending phase is represented by closed symbols and connected by a solid line, while PR in the descending phase is shown by open symbols and are connected by a dashed line.

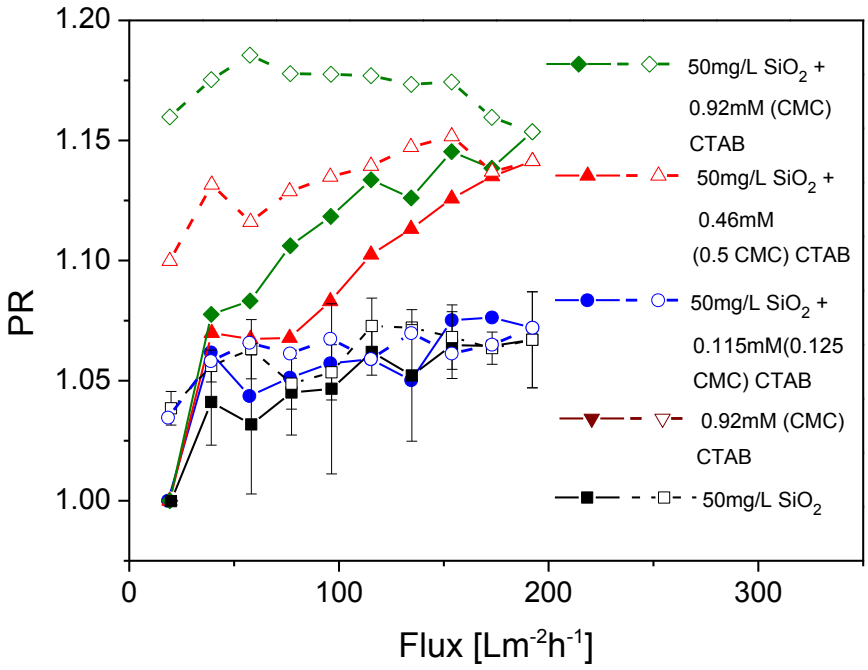

Figure 4-15: Permeability recovery (PR) for CTAB-SiO_2 systems at various surfactant concentrations. Open symbols and closed symbols denote fouling rates in ascending phase and descending phase, respectively.

In general, we observed that CTAB caused an increase in pure water permeability of the membrane module. This was similar to the trend observed for anionic surfactant SDS-SiO_2 systems. Furthermore, it appears that the change in PR increased with increasing CTAB concentration (i.e. $PR_{0.92mM\ CTAB\text{-}SiO2} > PR_{0.46mM\ CTAB\text{-}SiO2} > PR_{0.115mM\ CTAB\text{-}SiO2} \approx PR_{SiO2}$), which

suggests some dependency of irreversible fouling on surfactant concentration. We postulate that at low surfactant concentration, there are less monomers available to interact with the membrane surface. As concentration of surfactant is increased, more surfactant monomers would be forced into the membrane pores. These monomers may then be adsorbed to the hydrophobic groups on the membrane surface, improving surface wettability. The size of CTAB micelles is also much smaller than the average pore size of the membrane, at 3.5 nm [84] and 24 nm, respectively. Therefore it is likely that free CTAB monomers and micelles can penetrate into the membrane pores. Indeed, adsorption of surfactant inside membrane pores is generally irreversible [73, 91], which would explain why we observed the PR in the ascending phase is generally lower that the PR in the descending phase for both SDS and CTAB systems (Figure 4-14 and Figure 4-15).

4.6.3 Influence of TX100 on Permeability Recovery of UF Membranes

Figure 4-16 shows the permeability recovery trend for TX100-silica systems as a function of flux. Similarly, PR in the ascending phase is represented by closed symbols and connected by a solid line, while PR in the descending phase is shown by open symbols and are connected by a dashed line.

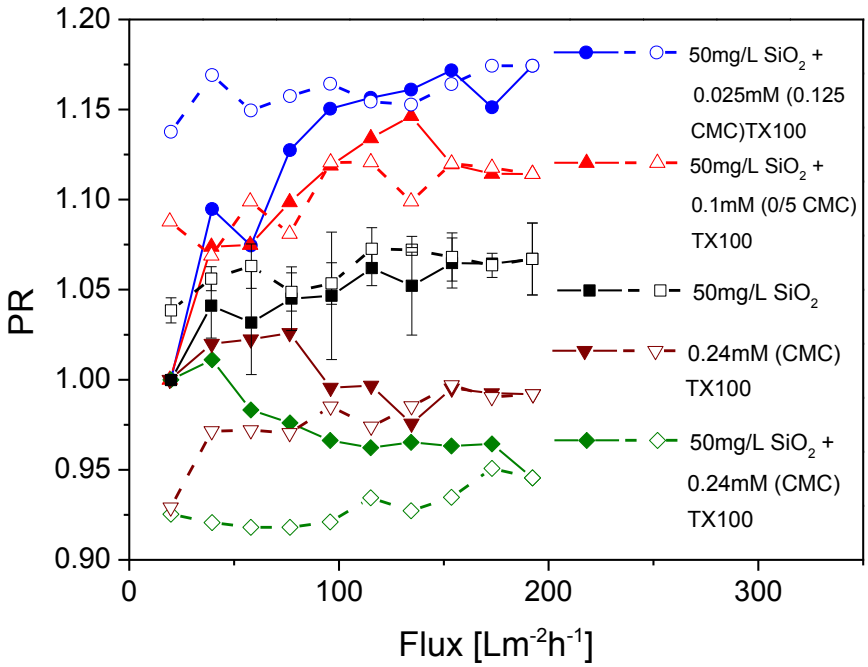

Figure 4-16: Permeability recovery (PR) for TX100-SiO_2 systems at various surfactant concentrations. Open symbols and closed symbols denote fouling rates in ascending phase and descending phase, respectively.

In the case of TX100 systems, we observed that the PR for 0.24 mM (CMC) TX100-SiO_2 and 0.24 mM (CMC) TX100 systems were also within the 10% experimental error. On the other

hand, the PR for 0.025 mM (0.125 CMC) TX100-SiO_2 and 0.1 mM (0.5 CMC) TX100-SiO_2 showed an increase in PR with time and flux.

It was also interesting to note that PR of 0.025 mM (0.125 CMC) TX100-SiO_2 was higher than PR of 0.1 mM (0.5 CMC) TX100. This can be partially explained according to these two competing mechanisms: in filtration of non-ionic surfactant systems: (i) adsorption of surfactants to hydrophobic groups on the membrane surface, leading to permeability increase and (iii) adsorption of surfactants to hydrophilic groups on the membrane surface, leading to permeability decrease. At low concentrations, monomers will adsorb to hydrophobic groups on the membrane surface, improving surface wettability. When concentrations in increased, since all the hydrophobic groups are adsorbed already, hydrophilic interactions may then take place, thus decreasing surface wettability [90]. The resulting permeability will probably depend on which mechanism is dominant.

5. CONCLUSIONS

To the best of our knowledge, this is the first time a colloidal system with surfactant was investigated in a flux-step manner, which allowed an insight into the dependency of fouling rates over a wide range of fluxes. The effect of three different types of commercial surfactants, CTAB, SDS and TX100, on colloidal silica fouling in an ultrafiltration membrane system was investigated. Stability of a colloidal silica system was found to be dependent on the type of surfactant, whereby aggregation or de-stabilisation of colloidal silica was most prominent with the addition of CTAB, followed by TX100 and SDS. We hypothesized that the main mechanism involved in the aggregation is the charge screening effects between surfactants and the negatively charged silica surface.

In terms of the performance of a membrane filtration system, we also observed that the fouling potential of a colloidal-surfactant suspension was dependent on the type of surfactant. A comparison of the overall fouling potential for surfactant-silica systems showed that SDS-silica systems showed fouling rates of an order of magnitude higher than those of CTAB-silica and TX100-silica systems at the same c_{surf}/c_{CMC} ratio. This was an unexpected finding, as we would expect stable colloidal systems such as SDS-silica systems would exhibit lower fouling than unstable colloidal systems (e.g. CTAB-silica systems). Furthermore, for each surfactant, the fouling potential of the colloidal feed water also generally increased with higher concentrations of surfactants. We postulate that the main fouling mechanisms involved were due to the following:

- adsorption of monomer on membrane surface due to electrostatic interaction,
- pore blocking due to hydrophobic interaction between monomer and hydrophobic groups on surface,
- interaction between surfactant monomer and PVP on the membrane, and
- pore blocking due to formation of cake layer.

With regards to irreversible fouling, we could make any conclusive remarks on the impact of surfactants on the extent of irreversible fouling of the membranes. This was probably due to the presence of surfactants which lowered the surface tension during pure water permeability measurements. However we could observe deposits on the membrane surface after backwashing from SEM imaging.

An overall comparison of total fouling rates for surfactant-silica systems indicated that SDS-silica systems showed fouling rates of an order of magnitude higher than those of CTAB-silica and TX100-silica systems at the same c_{surf}/c_{CMC} ratio. Based on the static light scattering and

zeta potential results of the silica-surfactant systems obtained in this study, we found this result unexpected, as one would expect the CTAB-SiO_2 systems to exhibit higher fouling rates compared to SDS-silica and TX100-silica systems.

In summary, there are many opposing/additive interactions that are occurring simultaneously in the filtration of a colloidal-surfactant system, such as particle-particle interaction, particle-membrane interaction, surfactant-membrane interaction, hydrodynamic conditions, kinetics of adsorption etc. As such it is very difficult to clearly distinguish what is occurring in the bulk suspension and solution-membrane interface.

6. RECOMMENDATIONS & FUTURE WORK

In light of the major results presented above, it is the author's recommendation that the following further work may be undertaken to assist in elucidating and clarifying the effect of different surfactants on the filtration of colloidal silica systems over a wide range of fluxes.

- Characterisation of zeta potential of silica-surfactant systems at a wider range of surfactant concentration, for instance, at concentrations higher than CMC;
- Different characterisation techniques of the silica- surfactant aggregates such as evaluation of fractal dimension
- Use different analytical techniques, such as small-angle neutron scattering (SANS), fluorescence etc to analyse the interaction between surfactant and silica in bulk solution, as well as membrane-solution interface, and use nanoparticle tracking analysis (NTA) technique to observe this behaviour in-situ;
- Undertake filtration experiments of 50 mg/L SiO_2 suspension with the addition of 8mM of monovalent salt (eg. NaCl) to distinguish the effect of salts;
- Undertake filtration experiments of surfactant-silica systems, at surfactant concentration much higher than CMC, to remove any ambiguity on whether micelles are formed or not;
- Undertake longer term constant volume experiments at a fixed fluxes, to observe the evolution of fouling profile as a function of time.
- Undertake filtration experiments with 'looser' pores, or membranes with bigger pore size or MWCO, to investigate the effect of surfactants on irreversible fouling, or experiments with flat sheet membranes instead. Using flat-sheet membranes may allow other characterisation techniques that are not possible with hollow-fibre configuration, such as surface contact angle etc.
- Re-design and/or modify the improved flux step filtration sequence, to include a longer backwash step to remove the cake layer.
- Repeat pure water permeability measurements to check reproducibility.
- TOC analysis of permeate samples should be completed without too much delay.
- SEM imaging of membranes after backwash to be undertaken without too much delay, to avoid any contamination, such as bacterial growth.

REFERENCES

1. Ostiguy, C., et al., *Nanoparticles:Actual Knowledge about Occupational Health and Safety Risks and Prevention Measures.* 2006, IRSST – Les Nanoparticules: Connaissances Actuelles Sur Les Risqué Et Les Measures De Prévention En SST (IRSST): Montréal, Quebec.
2. Schäfer, A.I., et al., *Microfiltration of colloids and natural organic matter.* Journal of Membrane Science, 2000. **171**(2): p. 151-172.
3. Vert, M., et al., *Terminology for biorelated polymers and applications (IUPAC recommendations 2012).* Pure and Applied Chemistry, 2012. **84**(2): p. 377-410.
4. Atkin, R., et al., *Mechanism of cationic surfactant adsorption at the solid-aqueous interface.* Advances in Colloid and Interface Science, 2003. **103**(3): p. 219-304.
5. Iler, R.K., *The Chemistry of Silica: Solubility, Polymerization, Colloid and Surface Properties and Biochemistry of Silica*. 1979, New York: Wiley.
6. Bolt, G.H., *Determination of the Charge Density of Silica Sols.* The Journal of Physical Chemistry, 1957. **61**(9): p. 1166-1169.
7. Koopal, L.K.a.G., T., *Surfactant Adsorption and Surface Solubilization.*, ed. I.R. Sharma. Vol. 615. 1995, Washington, DC: ACS. 78.
8. Kissa, E., *Dispersions: characterizations, testing and measurement.* . 1999, New York: Marcel Dekker.
9. Zhuravlev, L.T., *Concentration of hydroxyl groups on the surface of amorphous silicas.* Langmuir, 1987. **3**(3): p. 316-318.
10. Metin, C.O., et al., *Stability of aqueous silica nanoparticle dispersions.* Journal of Nanoparticle Research, 2011. **13**(2): p. 839-850.
11. Shi, J., *Steric Stabilization*, in *Department Materials Science & Enginnering* 2002, The Ohio State University: Ohio.
12. Aimar, P. and P. Bacchin, *Slow colloidal aggregation and membrane fouling.* Journal of Membrane Science, 2010. **360**(1-2): p. 70-76.
13. Gögelein, C., *Phase Behaviour of Proteins and Colloid-Polymer Mixtures*. 2008, Heinrich-Heine-Universitat Dusseldorf: Dusseldorf.
14. Tyrode, E., M.W. Rutland, and C.D. Bain, *Adsorption of CTAB on hydrophilic silica studied by linear and nonlinear optical spectroscopy.* Journal of the American Chemical Society, 2008. **130**(51): p. 17434-17445.
15. Brinck, J., B. Jönsson, and F. Tiberg, *Kinetics of nonionic surfactant adsorption and desorption at the silica-water interface: One component.* Langmuir, 1998. **14**(5): p. 1058-1071.
16. Goloub, T.P., et al., *Adsorption of cationic surfactants on silica. Surface charge effects.* Langmuir, 1996. **12**(13): p. 3188-3194.
17. Brinck, J., B. Jönsson, and F. Tiberg, *Kinetics of Nonionic Surfactant Adsorption and Desorption at the Silica-Water Interface: Binary Systems.* Langmuir, 1998. **14**: p. 5863-5876.
18. Fuerstenau, D.W., *The adsorption of surfactants at solid/water interfaces.* The chemistry of biosurfaces., ed. H. ML. Vol. 1. 1971, New York: Marcel Dekker.
19. Zhang, R. and P. Somasundaran, *Advances in adsorption of surfactants and their mixtures at solid/solution interfaces.* Advances in Colloid and Interface Science, 2006. **123-126**: p. 213-229.
20. Böhmer, M.R. and L.K. Koopal, *Adsorption of ionic surfactants on constant charge surfaces. Analysis based on a self-consistent field lattice model.* Langmuir, 1992. **8**(6): p. 1594-1602.
21. Gao, Y., J. Du, and T. Gu, *Hemimicelle formation of cationic surfactants at the silica gel-water interface.* Journal of the Chemical Society, Faraday Transactions 1: Physical Chemistry in Condensed Phases, 1987. **83**(8): p. 2671-2679.
22. Rupprecht, H. and T. Gu, *Structure of adsorption layers of ionic surfactants at the solid/liquid interface.* Colloid & Polymer Science, 1991. **269**(5): p. 506-522.
23. Somasundaran, P. and D.W. Fuerstenau, *Mechanisms of alkyl sulfonate adsorption at the alumina-water interface.* Journal of Physical Chemistry, 1966. **70**(1): p. 90-96.

24. Fan, A., P. Somasundaran, and N.J. Turro, *Adsorption of alkyltrimethylammonium bromides on negatively charged alumina.* Langmuir, 1997. **13**(3): p. 506-510.
25. Eskilsson, K. and V.V. Yaminsky, *Deposition of monolayers by retraction from solution: Ellipsometric study of cetyltrimethylammonium bromide adsorption at silica-air and silica-water interfaces.* Langmuir, 1998. **14**(9): p. 2444-2450.
26. Atkin, R., V.S.J. Craig, and S. Biggs, *Adsorption kinetics and structural arrangements of cationic surfactants on silica surfaces.* Langmuir, 2000. **16**(24): p. 9374-9380.
27. Howard, S.C. and V.S.J. Craig, *Very slow surfactant adsorption at the solid-liquid interface is due to long lived surface aggregates.* Soft Matter, 2009. **5**(16): p. 3061-3069.
28. Velegol, S.B., et al., *Counterion effects on hexadecyltrimethylammonium surfactant adsorption and self-assembly on silica.* Langmuir, 2000. **16**(6): p. 2548-2556.
29. McDermott, D.C., et al., *Study of an Adsorbed Layer of Hexadecyltrimethylammonium Bromide Using the Technique of Neutron Reflection.* Journal of Colloid And Interface Science, 1994. **162**(2): p. 304-310.
30. Ducker, W.A. and E.J. Wanless, *Adsorption of hexadecyltrimethylammonium bromide to mica: Nanometer-scale study of binding-site competition effects.* Langmuir, 1999. **15**(1): p. 160-168.
31. Maltesh, C. and P. Somasundaran, *Binding of sodium dodecyl sulfate to polyethylene oxide at the silica-water interface.* Journal of Colloid and Interface Science, 1992. **153**(1): p. 298-301.
32. Kumar, S., V.K. Aswal, and J. Kohlbrecher, *Size-dependent interaction of silica nanoparticles with different surfactants in aqueous solution.* Langmuir, 2012. **28**(25): p. 9288-9297.
33. Litton, G.M. and T.M. Olson, *Colloid deposition rates on silica bed media and artifacts related to collector surface preparation methods.* Environmental Science and Technology, 1993. **27**(1): p. 185-193.
34. Litton, G.M. and T.M. Olson, *Colloid Deposition Kinetics with Surface-Active Agents: Evidence for Discrete Surface Charge Effects.* Journal of Colloid and Interface Science, 1994. **165**(2): p. 522-525.
35. Ahualli, S., et al., *Adsorption of anionic and cationic surfactants on anionic colloids: Supercharging and destabilization.* Langmuir, 2011. **27**(15): p. 9182-9192.
36. Walz, J.Y., *The effect of surface heterogeneities on colloidal forces.* Advances in Colloid and Interface Science, 1998. **74**(1–3): p. 119-168.
37. Somasundaran, P., et al., *Effect of adsorption of non-ionic surfactant and non-ionic-anionic surfactant mixtures on silica-liquid interfacial properties.* Colloids and Surfaces, 1992. **63**(1-2): p. 33-37.
38. Clunie, S.J. and B.T. Ingram, *Adsorption from Solution at the Solid/Liquid Interface*, ed. C.H. Rochester. 1983, New York: Academic Press.
39. Paria, S. and K.C. Khilar, *A review on experimental studies of surfactant adsorption at the hydrophilic solid-water interface.* Advances in Colloid and Interface Science, 2004. **110**(3): p. 75-95.
40. Levitz, P. and H. Van Damme, *Fluorescence decay study of the adsorption of nonionic surfactants at the solid-liquid interface. 2. Influence of polar chain length.* Journal of Physical Chemistry, 1986. **90**(7): p. 1302-1310.
41. Levitz, P., H. Van Damme, and D. Keravis, *Fluorescence decay study of the adsorption of nonionic surfactants at the solid-liquid interface. 1. Structure of the adsorption layer on a hydrophilic solid.* Journal of Physical Chemistry, 1984. **88**(11): p. 2228-2235.
42. Giordano-Palmino, F., R. Denoyel, and J. Rouquerol, *Interfacial Aggregation of a Nonionic Surfactant: Effect on the Stability of Silica Suspensions.* Journal of Colloid and Interface Science, 1994. **165**(1): p. 82-90.
43. Domínguez, A., et al., *Determination of critical micelle concentration of some surfactants by three techniques.* Journal of Chemical Education, 1997. **74**(10): p. 1227-1231.
44. Liu, Y., et al., *Silica nanoparticles separation from water: Aggregation by cetyltrimethylammonium bromide (CTAB).* Chemosphere, 2013. **92**(6): p. 681-687.
45. Modaressi, A., et al., *CTAB aggregation in aqueous solutions of ammonium based ionic liquids; conductimetric studies.* Colloids and Surfaces A: Physicochemical and Engineering Aspects, 2007. **296**(1-3): p. 104-108.

46. Gao, H., et al., *Properties of polyethylene glycol (23) lauryl ether with cetyltrimethylammonium bromide in mixed aqueous solutions studied by self-diffusion coefficient NMR.* Journal of Colloid and Interface Science, 2004. **273**(2): p. 626-631.
47. Maiti, P.K., et al., *Cross-linking of micelles by gemini surfactants.* Langmuir, 2000. **16**(8): p. 3784-3790.
48. Lien, C.Y. and J.C. Liu, *Treatment of polishing wastewater from semiconductor manufacturer by dispersed air flotation.* Journal of Environmental Engineering, 2006. **132**(1): p. 51-57.
49. Vautier-Giongo, C. and B.L. Bales, *Estimate of the ionization degree of ionic micelles based on Krafft temperature measurements.* Journal of Physical Chemistry B, 2003. **107**(23): p. 5398-5403.
50. Bryleva, E.Y., et al., *Interfacial properties of cetyltrimethylammonium-coated SiO2 nanoparticles in aqueous media as studied by using different indicator dyes.* Journal of Colloid and Interface Science, 2007. **316**(2): p. 712-722.
51. Bi, Z., W. Liao, and L. Qi, *Wettability alteration by CTAB adsorption at surfaces of SiO2 film or silica gel powder and mimic oil recovery.* Applied Surface Science, 2004. **221**(1-4): p. 25-31.
52. Singh, G. and L. Song, *Influence of sodium dodecyl sulfate on colloidal fouling potential during ultrafiltration.* Colloids and Surfaces A: Physicochemical and Engineering Aspects, 2006. **281**(1-3): p. 138-146.
53. Kresheck, G.C. and W.A. Hargraves, *Thermometric titration studies of the effect of head group, chain length, solvent, and temperature on the thermodynamics of Micelle formation.* Journal of Colloid And Interface Science, 1974. **48**(3): p. 481-493.
54. Quina, F.H., et al., *Growth of sodium dodecyl sulfate micelles with detergent concentration.* Journal of Physical Chemistry, 1995. **99**(46): p. 17028-17031.
55. N.M. van Os, J.R. Haak, and L.A.M. Rupert, *Physico-chemical Properties of Selected Anionic, Cationic and Nonionic Surfactants.* 1993, Amsterdam: Elsevier Science Publishers.
56. Israelachvili, J.N., *Intermolecular and Surface Forces* 2nd ed. 1991, London: Academic Press.
57. Adamczyk, Z., P. Weroński, and E. Musiał, *Colloid particle adsorption at random site (heterogeneous) surfaces.* Journal of Colloid and Interface Science, 2002. **248**(1): p. 67-75.
58. Alexeev, V.L., et al., *Dispersions of silica particles in surfactant phases.* Langmuir, 1996. **12**(10): p. 2392-2401.
59. Oberdisse, J., *Small angle neutron scattering and model predictions for micelle-decorated colloidal silica beads.* Physical Chemistry Chemical Physics, 2004. **6**(7): p. 1557-1561.
60. Robson, R.J. and E.A. Dennis, *The size, shape, and hydration of nonionic surfactant micelles. Triton X-100.* Journal of Physical Chemistry, 1977. **81**(11): p. 1075-1078.
61. Kharitonova, T.V., N.I. Ivanova, and B.D. Summ, *Adsorption of cationic and nonionic surfactants on a SiO2 surface from aqueous solutions: 1. Adsorption of dodecylpyridinium bromide and Triton X-100 from individual solutions.* Colloid Journal, 2005. **67**(2): p. 242-248.
62. Bacchin, P., et al., *Colloidal surface interactions and membrane fouling: Investigations at pore scale.* Advances in Colloid and Interface Science, 2011. **164**(1-2): p. 2-11.
63. Bacchin, P., P. Aimar, and V. Sanchez, *Model for Colloidal Fouing of Membranes.* AICHe Journal, 1995. **41**(2): p. 368-376.
64. van der Marel, P., et al., *An improved flux-step method to determine the critical flux and the critical flux for irreversibility in a membrane bioreactor.* Journal of Membrane Science, 2009. **332**(1-2): p. 24-29.
65. Le Clech, P., et al., *Critical flux determination by the flux-step method in a submerged membrane bioreactor.* Journal of Membrane Science, 2003. **227**(1-2): p. 81-93.
66. Bacchin, P., P. Aimar, and R.W. Field, *Critical and sustainable fluxes: Theory, experiments and applications.* Journal of Membrane Science, 2006. **281**(1-2): p. 42-69.
67. Field, R.W., et al., *Critical flux concept for microfiltration fouling.* Journal of Membrane Science, 1995. **100**(3): p. 259-272.

68. Espinasse, B., P. Bacchin, and P. Aimar, *On an experimental method to measure critical flux in ultrafiltration.* Desalination, 2002. **146**(1–3): p. 91-96.
69. Wu, D., J.A. Howell, and R.W. Field, *Critical flux measurement for model colloids.* Journal of Membrane Science, 1999. **152**(1): p. 89-98.
70. Diez, V., et al., *A modified method for evaluation of critical flux, fouling rate and in situ determination of resistance and compressibility in MBR under different fouling conditions.* Journal of Membrane Science, 2014. **453**: p. 1-11.
71. Jeison, D. and J.B. van Lier, *Cake formation and consolidation: Main factors governing the applicable flux in anaerobic submerged membrane bioreactors (AnSMBR) treating acidified wastewaters.* Separation and Purification Technology, 2007. **56**(1): p. 71-78.
72. Bolton, G., D. LaCasse, and R. Kuriyel, *Combined models of membrane fouling: Development and application to microfiltration and ultrafiltration of biological fluids.* Journal of Membrane Science, 2006. **277**(1-2): p. 75-84.
73. Broeckmann, A., et al., *Modeling of pore blocking and cake layer formation in membrane filtration for wastewater treatment.* Desalination, 2006. **189**(1-3 SPEC. ISS.): p. 97-109.
74. Cohen Stuart, M.A., *Lecture Notes - Colloid Science*. 2006, Wageningen, Netherlands: Wageningen University.
75. Salgin, S., U. Salgin, and N. Soyer, *Streaming potential measurements of polyethersulfone ultrafiltration membranes to determine salt effects on membrane zeta potential.* International Journal of Electrochemical Science, 2013. **8**(3): p. 4073-4084.
76. Kim, J. and D.F. Lawler, *Characteristics of zeta potential distribution in silica particles.* Bulletin of the Korean Chemical Society, 2005. **26**(7): p. 1083-1089.
77. Cuperus, F.P., D. Bargeman, and C.A. Smolders, *Permporometry. The determination of the size distribution of active pores in UF membranes.* Journal of Membrane Science, 1992. **71**(1-2): p. 57-67.
78. Mulder, M., *Basic Principles of Membrane Technology*. 1991, Dordrecht, The Netherlands: Kluwer Academic Publishers.
79. Bukšek, H., T. Luxbacher, and I. Petrinić, *Zeta potential determination of polymeric materials using two differently designed measuring cells of an electrokinetic analyzer.* Acta Chimica Slovenica, 2010. **57**(3): p. 700-706.
80. van de Ven, W., *Towards optimal Saving in Membrane Operation: The development of process inspection and feedwater characterization tools*. 2008, Universiteit Twente: Enschede .
81. Biswas, S.C. and D.K. Chattoraj, *Kinetics of adsorption of cationic surfactants at silica-water interface.* Journal of Colloid and Interface Science, 1998. **205**(1): p. 12-20.
82. Hiemenz, P.C. and R. Rajagopalan, *Principles of Colloid and Surface Chemistry*. 3rd ed. 1997, New York: Marcel Dekker.
83. Prasad, M., R. Palepu, and S.P. Moulik, *Interaction between sodium dodecyl sulfate (SDS) and polyvinylpyrrolidone (PVP) investigated with forward and reverse component addition protocols employing tensiometric, conductometric, microcalorimetric, electrokinetic, and DLS techniques.* Colloid and Polymer Science, 2006. **284**(8): p. 871-878.
84. Jonsson, A.S. and B. Jonsson, *The influence of nonionic and ionic surfactants on hydrophobic and hydrophilic ultrafiltration membranes.* Journal of Membrane Science, 1991. **56**(1): p. 49-76.
85. Majewska-Nowak, K., I. Kowalska, and M. Kabsch-Korbutowicz, *Ultrafiltration of SDS solutions using polymeric membranes.* Desalination, 2005. **184**(1-3): p. 415-422.
86. Minatti, E., D.P. Norwood, and W.F. Reed, *Surfactant/polymer assemblies. 2. Polyelectrolyte properties.* Macromolecules, 1998. **31**(9): p. 2966-2971.
87. Norwood, D.P., E. Minatti, and W.F. Reed, *Surfactant/polymer assemblies. 1. Surfactant binding properties.* Macromolecules, 1998. **31**(9): p. 2957-2965.
88. Bury, R., B. Desmazières, and C. Treiner, *Interactions between poly(vinylpyrrolidone) and ionic surfactants at various solid/water interfaces: A calorimetric investigation.* Colloids and Surfaces A: Physicochemical and Engineering Aspects, 1997. **127**(1-3): p. 113-124.

89. Gilányi, T. and E. Wolfram, *Interaction of ionic surfactants with polymers in acqueous solution.* Colloids and Surfaces, 1981. **3**(2): p. 181-198.
90. Cornelis, G., et al., *Nanofiltration of nonionic surfactants: Effect of the molecular weight cutoff and contact angle on flux behavior.* Industrial and Engineering Chemistry Research, 2005. **44**(20): p. 7652-7658.
91. Bakx, A., A.M.D.E. Timmerman, and G. Frens, *Shear stimulated adsorption of surfactants from micellar solutions.* Colloids and Surfaces A: Physicochemical and Engineering Aspects, 2001. **183-185**: p. 149-157.
92. Sigma-Aldrich, *Product Specification - LUDOX® ™- 50 colloidal silica*. 2014.
93. Feng, Y., et al., *Interaction of poly(vinylpyrrolidone) with cationic and nonionic surfactants in aqueous solution studied by 1H NMR.* Colloid and Polymer Science, 2003. **281**(9): p. 902-906.
94. Duplâtre, G., M.F. Ferreira Marques, and M. Da Graça Miguel, *Size of sodium dodecyl sulfate micelles in aqueous solutions as studied by positron annihilation lifetime spectroscopy.* Journal of Physical Chemistry, 1996. **100**(41): p. 16608-16612.
95. Roudman, A.R. and F.A. Digiano, *Surface energy of experimental and commercial nanofiltration membranes: Effects of wetting and natural organic matter fouling.* Journal of Membrane Science, 2000. **175**(1): p. 61-73.

Appendix A: Flux and Transmembrane Pressure for a Complete Filtration Experiment

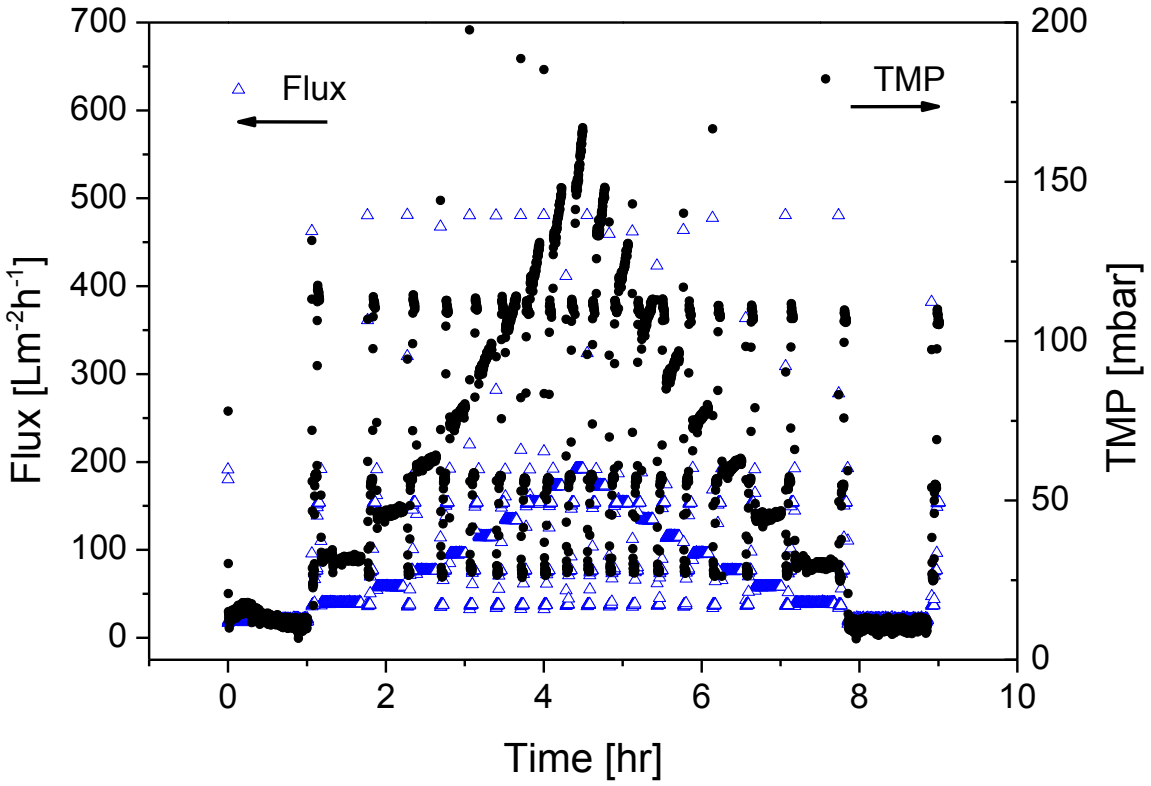

Figure B-1: Flux and transmembrane pressure profile for a complete filtration experiment. The open triangle symbols denote flux, while the full circle symbols denote the transmembrane pressure.

Appendix B: Surfactant Rejection Data for Colloidal Silica Systems in SDS, CTAB and TX-100 solutions

Surfactant rejection for SDS, CTAB and TX100 systems and shown in Figure B-1, Figure B-2 and Figure B-3, respectively. The surfactant rejection in the ascending phase is depicted with closed symbols while the rejection in the descending phase has open symbols. Note that the surfactant rejection for 0.115 mM (0.125 CMC) CTAB-SiO_2 was omitted from the figure as we observed very negative rejections (-990% to -50%), of which we considered the data was unreliable.

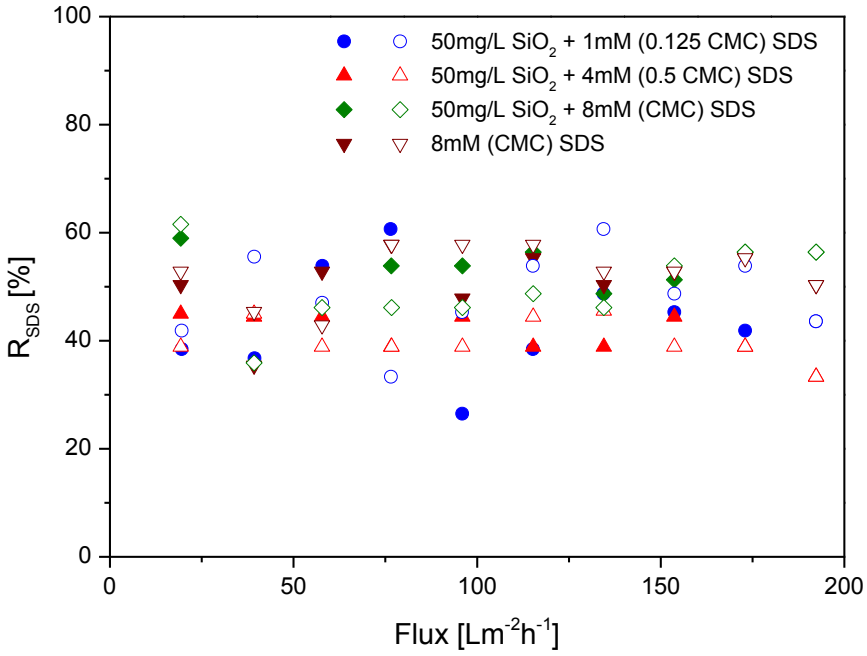

Figure B-1: Effect of concentration on SDS rejection in filtration of SDS-silica systems. Open symbols and closed symbols denote fouling rates in ascending phase and descending phase, respectively.

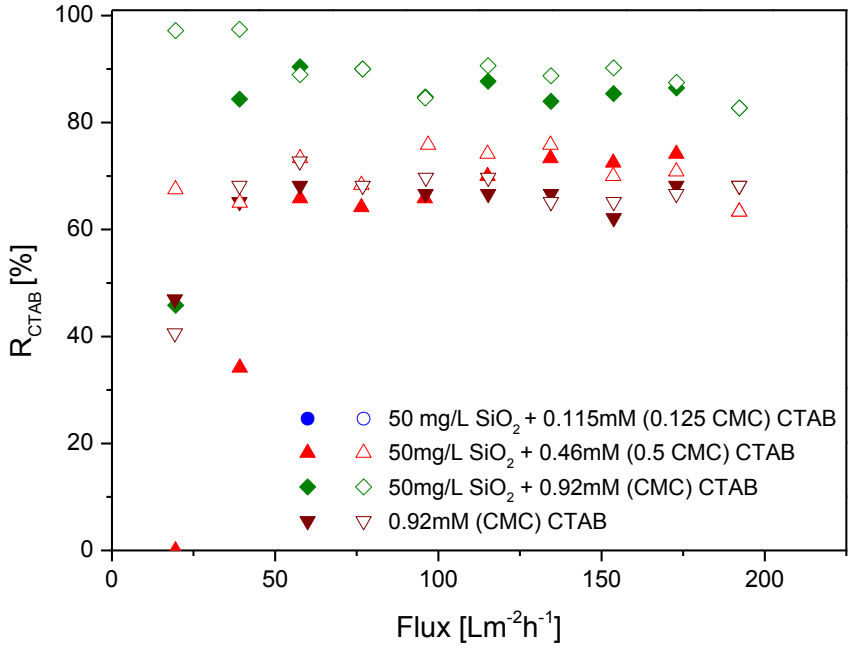

Figure B-2: Effect of concentration on CTAB rejection in filtration of CTAB-silica systems. Open symbols and closed symbols denote fouling rates in ascending phase and descending phase, respectively.

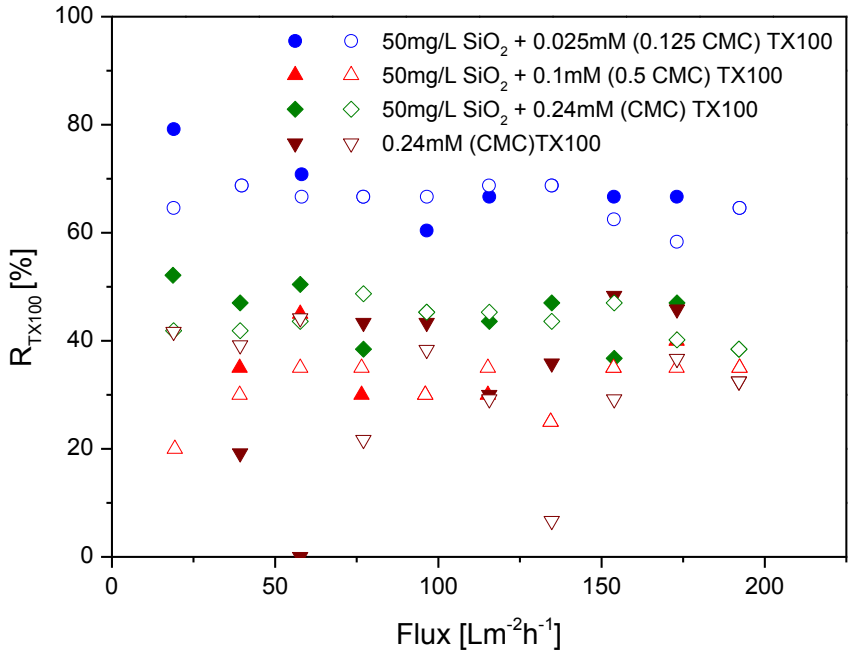

Figure B-3: Effect of concentration on TX100 rejection in filtration of TX100-silica systems. Open symbols and closed symbols denote fouling rates in ascending phase and descending phase, respectively.